

PLACE IN RETURN BOX to remove this checkout from your record.
TO AVOID FINES return on or before date due.
MAY BE RECALLED with earlier due date if requested.

DATE DUE	DATE DUE	DATE DUE

**COMPUTATIONAL DESIGN OF MECHANICAL
STRUCTURES IN ELASTICITY USING
MULTI-RESOLUTION ANALYSIS**

By

Sudarsanam Chellappa

A DISSERTATION

**Submitted to
Michigan State University
in partial fulfillment of the requirements
for the degree of**

DOCTOR OF PHILOSOPHY

Department of Mechanical Engineering

2003

COMPUTATI

A form

elastic system

various resol

homogenizati

resolution and

elasticity ope

information.

matrices tha

models of la

involving co

intensive cor

is applied to

heterogeneiti

examples in v

presented.

ABSTRACT

COMPUTATIONAL DESIGN OF MECHANICAL STRUCTURES IN ELASTICITY USING MULTI-RESOLUTION ANALYSIS

By

Sudarsanam Chellappa

A formal methodology for reducing the size of models used in the analysis of elastic systems is presented. This involves an explicit representation of the model at various resolutions and is accomplished using a projection generated numerical homogenization procedure. The framework for this analysis is derived from the multi-resolution analysis associated with the construction of wavelet bases. This is applied to elasticity operators to average fine scale properties and behavior while limiting loss of information. In discretized form, the method produces equivalent smaller stiffness matrices that can be used as building blocks (*super-elements*) to construct reduced models of larger systems. The principal application envisioned is in design problems involving complex structural systems, such as in crash-worthiness design, where very intensive computations demand computational efficiency. This model reduction scheme is applied to the problem of layout optimization of structures involving multi-scale heterogeneities of sizes that may be comparable to the size of the structure. Numerical examples in which the heterogeneities are in the form of perforations of various sizes are presented.

To my parents

I would

Your guidance

Dr. Andre E

time spent i

like to thank

Lastly

motivation

ACKNOWLEDGEMENTS

I would like to express my sincere gratitude to my advisor Dr. Alejandro Díaz. Your guidance and support has been invaluable. I thank the members of my committee: Dr. Andre Benard, Dr. Michael Frazier and Dr. Farhang Pourboghraat. Thank you for the time spent in reviewing this document and providing valuable suggestions. I would also like to thank Dr. Martin Bendsøe. Thank you for your insight and suggestions.

Lastly, I would like to thank my family. Thank you for all your support and motivation without which this endeavor would not have been possible.

LIST C

LIST C

1 Intro

2 Wave

2.1 I

2.2 M

2.3 E

2.4 G

2.5 T

2.6 C

2.7 F

2.8 W

3 Model R

3.1 Sca

3.2 The

3.3 A M

3.4 A M

3.4.1

3.4.2

3.4.3

3.5 Comp

TABLE OF CONTENTS

LIST OF TABLES	viii
LIST OF FIGURES	ix
1 Introduction	1
2 Wavelets And Multi-Scale Representation Of Functions	7
2.1 Introduction	7
2.2 Multi-Resolution Analysis	8
2.3 Example Using the Haar Basis	10
2.4 Generalized Orthogonal Scaling Functions and Wavelets	10
2.5 The Discrete Wavelet Transform	15
2.6 Constructing The Basic Scaling Function and Wavelet	19
2.7 Function Approximation Using Orthogonal Projection	23
2.8 Wavelets In Multiple Dimensions	25
3 Model Reduction In Elastostatics	28
3.1 Scales And Material Properties In Elasticity	29
3.2 The Fine-Scale Elasticity Problem	32
3.3 A Multi-Resolution Analysis Of Material Distribution	34
3.4 A Multi-Resolution Analysis Of Displacement	37
3.4.1 A Periodic Multi-Resolution Reduction Scheme	37
3.4.2 Transformation To Finite Element Form	44
3.4.2.1 Method I	45
3.4.2.2 Method II	46
3.4.2.3 Method III	48
3.4.3 Computational Aspects	50
3.5 Comparison Of Model Reduction Schemes	53

3

3

3.6 C

St

3.7 C

3.

3.7

3.7

3.8 Nu

3.8

3.8

3.8

4 Multi-Sc

4.1 Bac

4.2 Opti

4.2.

4.2.2

4.2.3

4.3 Comp

4.4 Optim

4.5 Optim

4.5.1

4.5.2

4.5.3

4.6 Exam

4.6.1

4.6.2

4.6.3

3.5.1 Comparison Between MRA Of Material Distribution And MRA Of Displacements	53
3.5.2 Comparison Between MRA Techniques And Classical Homogenization	56
3.6 Computing The Non-Periodic Reduced Stiffness Matrix Of A Substructure	62
3.7 Computing Fine-Scale Stresses By Augmentation	66
3.7.1 Computing The Periodic Large-Scale Nodal Displacements	68
3.7.2 Conversion To A Wavelet Basis	71
3.7.3 Periodic Multi-Resolution Refinement	72
3.8 Numerical Examples	74
3.8.1 Example 1	74
3.8.2 Example 2	81
3.8.3 Example 3	87
4 Multi-Scale Layout Optimization Of Structures	93
4.1 Background: Topology Optimization Of Structures	94
4.2 Optimal Design Using Macro-Scale Heterogeneities	97
4.2.1 Building A Model Using Reduced Substructures	99
4.2.2 Constructing Libraries Of Perforated Substructures	101
4.2.3 Sensitivity Analysis	103
4.3 Compliance Minimization Problems	105
4.4 Optimization Using Fixed Layouts Of Reduced Substructures	108
4.5 Optimization Using Variable Layouts Of Reduced Substructures	110
4.5.1 Perforated Substructures And Layout Dependency	110
4.5.2 A Dividing Approach To Optimization With Variable Layouts	113
4.5.3 A Merging Approach To Optimization With Variable Layouts	115
4.6 Examples	119
4.6.1 Example 1	119
4.6.2 Example 2	121
4.6.3 Example 3	122

5 Conclusions

5.1

5.2

5.3

BIBLIOGRAPHY

4.6.4 Example 4	125
4.6.5 Example 5	132
5 Concluding Remarks	139
5.1 Summary	139
5.2 Conclusions	140
5.3 Areas Of Future Work	141
BIBLIOGRAPHY	142

3.1 Ma

3.2 Ma

3.3 Ma

List Of Tables

3.1	Main Results For Example 1	79
3.2	Main Results For Example 2	86
3.3	Main Results For Example 3	92

- 2.1 Ha
- 2.2(a) Ori
- 2.2(b) Ap
- 2.2(c) Ap
- 2.2(d) Det
- 2.3 Sing
- 2.4 The
- 2.5 The
- 2.6 Sing
- 2.7 The
- 2.8 Som
- 2.9 Orth
- 2.10 A m
- 3.1 A st
- 3.2 Stru
- 3.3 Basi
- 3.4 Con
- 3.5 Con
- 3.6 Con
- 3.7 Choi
- 3.8 Boun
- using
- 3.9(a) Strain
- 3.9(b) Strain
- 3.9(c) Strain
- 3.9(d) Strain
- 3.10 Substr
- 3.11 Consta

List Of Figures

2.1	Haar scaling function and wavelet	11
2.2(a)	Original function	12
2.2(b)	Approximation at scale 6	12
2.2(c)	Approximation at scale 5	12
2.2(d)	Detail at scale 5	12
2.3	Single stage discrete wavelet decomposition	17
2.4	The convolution operation	17
2.5	The dyadic down sampling operation	18
2.6	Single stage discrete wavelet reconstruction	18
2.7	The dyadic up sampling operation	19
2.8	Some commonly used orthogonal scaling functions and wavelets	22
2.9	Orthogonal projections from wavelet to finite-element spaces	23
2.10	A multi-scale representation of two-dimensional functions	27
3.1	A structure built from substructures of different scales	31
3.2	Structure of L_J and H_{J-k}	43
3.3	Basis functions in wavelet and finite-element spaces	44
3.4	Conversion from wavelet to finite-element spaces using method I	46
3.5	Conversion from wavelet to finite-element spaces using method II	47
3.6	Conversion from wavelet to finite-element spaces using method III	49
3.7	Choices of the material distributions for the comparison	55
3.8	Bounds on the maximum relative error between the strain energy computed using material MRA and displacement MRA	55
3.9(a)	Strain energy comparisons for material distribution (a)	60
3.9(b)	Strain energy comparisons for material distribution (b)	60
3.9(c)	Strain energy comparisons for material distribution (c)	61
3.9(d)	Strain energy comparisons for material distribution (d)	61
3.10	Substructure surrounded by a weak fictitious domain	63
3.11	Constant pre-strains applied to a patch of substructures	66

3.12	Decomposition of a general non-periodic function into a coarse, non-periodic function and a periodic function	69
3.13	Geometry and boundary conditions for example 1	74
3.14	Von Mises stress distribution using the fine-scale model of the structure in example 1	75
3.15	Assembly of substructures for example 1	76
3.16	Von Mises stress distribution in reduced model using material MRA	77
3.17	Von Mises stress distribution in reduced model using displacement MRA	77
3.18	Von Mises stress in substructure (A) from the reduced model using displacement MRA	78
3.19	Von Mises stress in substructure (A) after augmentation	78
3.20	Detail of Von Mises stress near substructure (A) obtained from the fine-scale model	79
3.21	Geometry and boundary conditions for example 2	81
3.22	Von Mises stress distribution from the fine-scale model of the structure	82
3.23	Arrangement of substructures for example 2	83
3.24	Von Mises stress distribution from reduced model using material MRA	84
3.25	Von Mises stress distribution from reduced model using displacement MRA ..	84
3.26	Von Mises stress in substructure (A) from reduced model using displacement MRA	85
3.27	Von Mises stress in substructure (A) after augmentation	85
3.28	Detail of the Von Mises stress in a region around substructure (A) from the fine-scale model	86
3.29	Geometry and boundary conditions for example 3	87
3.30	Von Mises stress distribution from fine-scale model	88
3.31	Arrangement of substructures for example 3	88
3.32	Von Mises stress distribution from reduced model using material MRA	89
3.33	Von Mises stress distribution from reduced model using displacement MRA ..	89
3.34	Von Mises stress in substructure (A) from reduced model using displacement MRA	90
3.35	Von Mises stress in substructure (A) after augmentation	90

3.36 D
f
4.1 A
4.2 A
4.3 A
4.4 A
P
4.5 A
4.6 A
4.7 S
4.8 S
4.9 C
4.10 C
4.11 A
4.12 B
4.13 C
P
4.14 C
P
4.15 III
4.16 III
4.17 Pr
4.18 Op
4.19 Pr
4.20 Op
4.21 Op
4.22 Pr
4.23 Pr
4.24 Op
4.25 La
4.26 Pro

3.36	Detail of the Von Mises stress in substructure (A) obtained from the fine-scale model	91
4.1	A structure with a composite microstructure	96
4.2	A typical topology optimization problem and solution	97
4.3	A typical structure with macro-scale heterogeneities (perforations)	98
4.4	A structure built from an assembly of substructures with circular perforations	99
4.5	Assembly of substructures	100
4.6	A non-conforming assembly of discretized substructures	101
4.7	Substructures with circular perforations for various finest levels	103
4.8	Substructures with rectangular and circular perforations	105
4.9	Optimization using fixed layout of substructures	107
4.10	Optimization using variable layouts of substructures	107
4.11	A design domain and a possible layout of reduced substructures	109
4.12	Boundary traction test	110
4.13	Comparison of strain energies in substructures with different number of perforations for various boundary tractions	111
4.14	Comparison of strain energies in substructures with different number of perforations for various constant pre-strains	112
4.15	Illustration of possible evolution of layouts using the dividing approach	113
4.16	Illustration of possible evolution of layouts using the merging approach	116
4.17	Problem description for example 1	120
4.18	Optimal layout for example 1	120
4.19	Problem description for example 2	121
4.20	Optimal layout using multiple load cases for example 2	121
4.21	Optimal layout using single load case for example 2	122
4.22	Problem description with uniform layout for example 3	122
4.23	Problem description with multi-size layout for example 3	123
4.24	Optimal layout using single-size substructures for example 3	123
4.25	Layout using multi-size substructure for example 3	124
4.26	Problem description for example 4	125

4.27
a
4.28 S
4.29 C
e
4.30 S
e
4.31 S
4.32 O
co
4.33 Pr
4.34 Ini
lay
4.35 Sec
4.36 Op
stru
4.37 Star
corr
4.38 Sequ
4.39 Opti
struc
subst
4.40 Layo
using

4.27	Starting arrangement of substructures for optimization using the dividing approach for example 4 and the corresponding optimal layout	126
4.28	Sequence of steps in the dividing approach for example 4	127
4.29	Optimal arrangement of substructures using the dividing approach for example 4 and the corresponding optimal layout	128
4.30	Starting arrangement of substructures using the merging approach for example 4 and the corresponding optimal layout	129
4.31	Sequence of steps in the merging approach for example 4	130
4.32	Optimal arrangement of substructures using the merging approach and the corresponding optimal layout for example 4	131
4.33	Problem description for example 5	132
4.34	Initial layout using the merging approach and optimal structure using this layout for example 5	133
4.35	Sequence of layouts obtained using the merging approach for example 5	134
4.36	Optimal arrangement of substructures and the corresponding optimal structure obtained using the merging approach for example 5	135
4.37	Starting layout of substructures for the dividing approach and the corresponding optimal structure for example 5	135
4.38	Sequence of layouts obtained using the dividing approach for example 5	136
4.39	Optimal arrangement of substructures and the corresponding optimal structure obtained using the dividing approach with prescribed number of substructures of size $2L$ for example 5	137
4.40	Layout of substructures and corresponding optimal structure obtained using the dividing approach with a perimeter constraint for example 5	138

CR

Inf

In the

optimiz

prevent

an auto

comput

for exte

complex

possible

minimum

In

surfaces).

is invoked

Chapter 1

Introduction

In the design of complex structural systems or structures with complex behavior to optimize certain properties such as crashworthiness, the complexity of the problem often prevents a detailed computational analysis of the structure. A typical computer model of an automotive structure involves around 10^6 degrees of freedom requiring days of computer time to run a single analysis. Under these conditions the current practice calls for extensive simplifications. The strategies for simplification of the optimal design of complex structures (or structures with complex behavior) can be divided into two possible approaches: one that uses a full-scale model but limits the evaluations to a minimum and the other that uses a reduced model.

In the first approach, the optimization is applied on *surrogate models* (or response surfaces), constructed using a strategic (statistical) sampling of a full-scale model, which is invoked only sparingly to save effort. The full-scale model is still used as the principal

source of
evaluation
very effective
[40]). As
to build
attractive

Th
full-scale
noted that
information
replaces. I
of accuracy
same physi
the results of

It is
one that co
models) eff
savings that
presents a
representatio
preliminary,
it ignores fea
Nevertheless,

source of information about the system and therefore the computational cost per evaluation is not changed. Instead, the number of evaluations is reduced. This strategy is very effective whenever the number of design variables involved is small (see Yang [40]). As the number of variables increases, the number of function evaluations required to build a reasonable response surface also increases, rendering the approach less attractive and not of much advantage compared to using the full-scale model throughout.

The main idea in the second strategy is to reduce computations by replacing the full-scale model by a *reduced model*, a model that is less expensive to evaluate. It is noted that the process of constructing the reduced model may result in the loss of critical information, causing the reduced model to be significantly less accurate than the model it replaces. In this strategy the computational cost per evaluation is reduced at the expense of accuracy. In addition, design variables in the reduced order model may not have the same physical meaning as the variables in the original problem, making interpretation of the results difficult.

It is likely that the most effective strategy for the design of complex structures is one that combines the two approaches (i.e., response surface methods and reduced models) effectively. A response surface methodology would clearly benefit from the savings that result from a carefully crafted, reduced model. With this in mind, this work presents a formal methodology for model reduction that involves an explicit representation of the model at various scales. The work presented here is still preliminary, in the sense that it addresses only the elastic behavior of a structure and thus it ignores features that are crucial to the full understanding of many complex problems. Nevertheless, this is a necessary first step and it provides an important understanding of

how a
structu

T

quite s

primari

reductio

methods

freedom

degrees

freedom

componen

the dynam

componen

each intern

problem is

properties o

coarser mo

average the

The co

from fine-sca

using asympt

techniques, th

different scales

how a formal procedure can be derived to reduce the complexity of models used in structural design without losing information that can be relevant in the design problem.

The problem of constructing reduced models of structures has been investigated for quite some time in the context of vibration and control of structural systems. These primarily comprise of methods such as pseudo static variants of the classical Guyan's reduction method or component-mode based techniques. In the Guyan's reduction type methods (see Guyan [22], Friswell et al [19], Wilson et al [39]), a set of degrees of freedom of the system are chosen to be master and another set chosen as the slave degrees of freedom. The reduction process aims to eliminate the slave degrees of freedom and express the state equation in terms of the master degrees of freedom. In component mode based techniques (see Hurty [24], Craig and Bampton [8], Seshu [35]), the dynamics of a structure are described by selected sets of normal modes of individual components of the structure, plus a set of static vectors that account for the coupling at each interface where individual components are connected. In the present work, the problem is phrased in the language of *homogenization* and the computation of effective properties of composites: starting from a structure that is modeled in fine detail, we seek coarser models of the same structure (i.e., "homogenized" or "effective" structures) that average the detail without losing the (relevant) fine scale information.

The collection of mathematical methods for extracting the coarse-scale behavior from fine-scale models is termed *homogenization*. Typically, such problems are solved using asymptotic expansion techniques or weak-limits; see Bensoussan et al [5]. In these techniques, there is no accounting for structures with features involving distinctly different scales. In a recent paper by Pecullan et al [30] the subject of scale effects on the

behavior

tensors

volume

numerical

appear in

homogeni

resolution

linear hom

system of e

original sys

these effect

could deter

complete de

[20] applied

equivalent t

method of

developed m

more robust

situations tha

technique to

homogenizati

that it could

Dorabantu us

behavior of two-dimensional composites is discussed by comparing the apparent stiffness tensors of two-dimensional elastic composites for various sizes of the representative volume element. Also, there has been substantial effort to develop methods for numerical homogenization that facilitate the analysis of problems involving systems that appear in multiple scales. Brewster and Beylkin [7] outlined a procedure for numerical homogenization of a system of linear ordinary differential equations using the multi-resolution analysis (MRA) associated with the construction of a wavelet basis. Their linear homogenization procedure consists of an algorithm to produce an effective linear system of equations whose solutions are the coarse-scale projections of the solution of the original system of equations, called multi-resolution reduction, and one for augmenting these effective equations to produce the homogenized solution, called augmentation. One could determine the projection of the solution at any intermediate scale and obtain a complete description of the transition from fine to coarse scale representation. Gilbert [20] applied the same approach to a system of two ordinary differential equations that is equivalent to a one dimensional second order elliptic problem and compared the classical method of homogenization, i.e., the asymptotic expansion method, with this recently developed multi-resolution technique. It was noted that the MRA scheme is physically more robust than the classical theory, i.e. it could be applied to many more physical situations than the classical theory. Dorabantu and Engquist [15] applied the same MRA technique to a discrete elliptic second-order differential equation. They observed that this homogenization procedure produced an operator that preserved its divergence form and that it could be well approximated by a band diagonal matrix. The work by Gilbert and Dorabantu use the *Haar* basis (piecewise constants) for the discretization of the

differen

differen

In

of elastic

using fixe

Glowinski

work, the

elasticity m

could be th

large stiffne

generalized

material in a

this problem

to the size of

is specifically

scale heterog

The principal

1. To deve

systems

fine-scal

differential equations. Beylkin and Coult [6] applied this MRA method to elliptic partial differential equations and studied the spectral characteristics of the reduced operators.

In linear structural analysis, the associated differential equations are the equations of elasticity. Techniques for solving the elasticity problem defined on arbitrary domains using fixed-scale wavelet-Galerkin methods have been investigated for some time (see Glowinski et al [21], Wells et al [37], Diaz [14], DeRose and Diaz [11]). In the present work, the MRA based numerical homogenization scheme is applied to the equations of elasticity modeled using a wavelet-Galerkin technique. In this case, the model reduction could be thought of as a method to produce equivalent smaller stiffness matrices from large stiffness matrices. An application of this method is then presented in the context of generalized topology or layout optimization of structures, i.e., the optimal distribution of material in a given design space subject to prescribed loads. The existing methods for this problem do not account for the presence of finite scales that may even be comparable to the size of the design domain. Here, a method that uses a model reduction scheme that is specifically tailored to the problem of layout optimization of structures such that finite scale heterogeneities can be accounted is presented.

The principal goals of this dissertation are:

1. To develop a consistent scheme to compute equivalent reduced models of structural systems in linear elasticity at various coarse-scales that retain relevant features of fine-scale models.

2. To c
acco
size

The rema
introduc
Chapter 3
framework
Chapter 4
problem o
heterogene
possible dir

2. To develop a method for the layout optimization of structures in elasticity that accounts for multi-scale heterogeneities of sizes that may even be comparable to the size of the structure.

The remainder of this dissertation is organized as follows. Chapter 2 gives a brief introduction to wavelets and the concepts of multi-resolution analysis of functions. Chapter 3 presents a model reduction scheme using the multi-resolution analysis framework. Numerical examples that illustrate the proposed scheme are provided. Chapter 4 discusses the application of the proposed model reduction technique to the problem of layout optimization of two-dimensional structures in elasticity, in which heterogeneities of finite scale can be accounted. Finally, some concluding remarks and possible directions for future work are presented in Chapter 5.

V

F

2.

"W

freq

scal

wav

hier

anal

comp

—

⁴ Daub

Chapter 2

Wavelets and Multi-Scale Representation of Functions

2.1 Introduction

“Wavelets are mathematical functions that are used to cut up data into different frequency components and then study each component with a resolution matched to its scale”[§]. The concept of multi-resolution analysis is fundamental to the theory of wavelets. The main idea is the separation of the information to be analyzed hierarchically into *principal* and *residual* parts. In signal processing applications this is analogous to decomposing a signal into its low frequency and high frequency components with the knowledge of when they occur. This has definite advantages over

[§] Daubechies [10]

the standa
information
making wa
Fourier tran
been applie
solving ord
emphasis o
chapter. F
refer to the
references th

2.2 Mult

Definition:

functions - i

(i) $\{0\}$

(ii) \cap_j

(iii) $g(\dots)$

(iv) $g(x)$

(v) The

$\{x\}$

Thus, using th

the standard Fourier analysis, which identifies frequency information but no time information. A variety of efficient algorithms using wavelets have been developed making wavelet transforms on par with computationally efficient methods such as fast Fourier transforms. Wavelets have become a very popular tool in engineering and have been applied to a wide range of problems in signal processing, image processing and in solving ordinary and partial differential equations. A brief introduction to wavelets with emphasis on applications in computational engineering analysis is presented in this chapter. For detailed information about the construction and applications of wavelets refer to the books by Daubechies [10], Frazier [18], Resnikoff and Wells [31] and the references therein.

2.2 Multi-Resolution Analysis

Definition: A multi-resolution analysis (MRA) of $L^2(\mathbb{R})$ - the space of square integrable functions – is a nested sequence of subspaces V_j such that

- (i) $\{0\} \subset \dots \subset V_{-1} \subset V_0 \subset V_1 \subset \dots \subset L^2(\mathbb{R})$
- (ii) $\bigcap_j V_j = \{0\}$ and $\overline{\bigcup_j V_j} = L^2(\mathbb{R})$
- (iii) $g(x) \in V_j \Leftrightarrow g(2x) \in V_{j+1}$
- (iv) $g(x) \in V_0 \Leftrightarrow g(x-k) \in V_0, k \in \mathbb{Z}$
- (v) There exists a scaling function $\varphi(x) \in V_0$ such that $\{\varphi(x-k), k \in \mathbb{Z}\}$ is an orthonormal basis for V_0

Thus, using the above definition it be can shown that if

$$V_0 = \text{span} \{ \varphi(x-k), k \in \mathbb{Z} \}$$

then

Since $V_0 \subset$

Thus,

where $a_k \in$

the dilation

$V_J = \text{span} \{$

A function f

and more gen

$P_J f$ approac

the approxima

Define a new

i.e.,

then

$$V_1 = \text{span}\{\varphi(2x - k), k \in \mathbb{Z}\}$$

Since $V_0 \subset V_1$, any function in V_0 can be expressed in terms of the basis function of V_1 .

Thus,

$$\varphi(x) = \sum_{k=-\infty}^{\infty} a_k \varphi(2x - k) \quad (2.1)$$

where $a_k \in l^2(\mathbb{R})$ (the space of square summable sequences). This equation is known as

the dilation equation or the scaling relation. Denote: $\varphi_{J,k}(x) = 2^{J/2} \varphi(2^J x - k)$ and

$V_J = \text{span}\{\varphi_{J,k}(x), k \in \mathbb{Z}\}$. The dilation parameter J is known as the *scale*.

A function $f \in L^2(\mathbb{R})$ may be approximated by its projection onto the space V_0 as

$$P_0 f = \sum_{k=-\infty}^{\infty} c_{0,k} \varphi(x - k) \quad (2.2)$$

and more generally by its projection onto the space V_J as

$$P_J f = \sum_{k=-\infty}^{\infty} c_{J,k} \varphi_{J,k}(x) \quad (2.3)$$

$P_J f$ approaches f as $J \rightarrow \infty$, i.e., higher (finer) the scale of the representation, better

the approximation. Consider now the difference between the subspaces V_{J-1} and V_J .

Define a new subspace W_{J-1} such that it is the orthogonal complement of V_{J-1} in V_J ,

i.e.,

$$\begin{aligned} V_J &= V_{J-1} \oplus W_{J-1} \\ V_{J-1} &\perp W_{J-1} \end{aligned} \quad (2.4)$$

It follows t

function ψ

subspace W

for W_j . I

orthonormal

Then, from e

This equation

a level $J - 1$

since the spa

terms of the s

2.3 Exam

The simplest

function and

constant func

It follows that the spaces W_j are orthogonal and that $\bigoplus_{j \in \mathbb{Z}} W_j = L^2(\mathbb{R})$. Define a wavelet

function $\psi(x) \in W_0$ such that $\{\psi(x-k), k \in \mathbb{Z}\}$ forms an orthonormal basis for the

subspace W_0 . Then, $\{\psi_{J,k}(x) = 2^{J/2} \psi(2^J x - k), k \in \mathbb{Z}\}$ forms an orthonormal basis

for W_J . In addition, it follows that $\{\psi_{j,k}(x) = 2^{j/2} \psi(2^j x - k); j, k \in \mathbb{Z}\}$ forms an

orthonormal basis for $L^2(\mathbb{R})$. Denote the projection of a function f on W_J as $Q_J f$.

Then, from equation (2.4) we have

$$P_J f = P_{J-1} f + Q_{J-1} f \quad (2.5)$$

This equation means that $Q_{J-1} f$ represents the detail that needs to be added to get from

a level $J-1$ representation of the function to a level J representation. Furthermore,

since the space W_0 is contained in the space V_1 , the wavelet function can be expressed in

terms of the scaling function at the next higher scale,

$$\psi(x) = \sum_{k=-\infty}^{\infty} b_k \varphi(2x - k) \quad (2.6)$$

2.3 Example Using the Haar Basis

The simplest possible orthogonal wavelet system is generated from the Haar scaling

function and wavelet shown in figure 2.1. The Haar scaling function is a piece-wise

constant function defined as

$$\varphi(x) = \begin{cases} 1 & 0 \leq x < 1 \\ 0 & \text{otherwise} \end{cases} \quad (2.7)$$

This function

Similarly th

It can be se

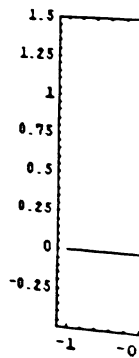


Figure 2.2(a)

function is a

figure 2.2(b)

V_5 and W_5

removed from

This function satisfies the scaling relation (equation (2.1)) with coefficients $a_0 = a_1 = 1$,

$$\varphi(x) = \varphi(2x) + \varphi(2x-1) \quad (2.8)$$

Similarly the Haar wavelet is defined as

$$\psi(x) = \begin{cases} 1 & 0 \leq x < 0.5 \\ -1 & 0.5 \leq x < 1 \\ 0 & \text{otherwise} \end{cases} \quad (2.9)$$

It can be seen that the Haar wavelet satisfies equation (2.6) with $b_0 = 1$ and $b_1 = -1$,

$$\psi(x) = \varphi(2x) - \varphi(2x-1) \quad (2.10)$$

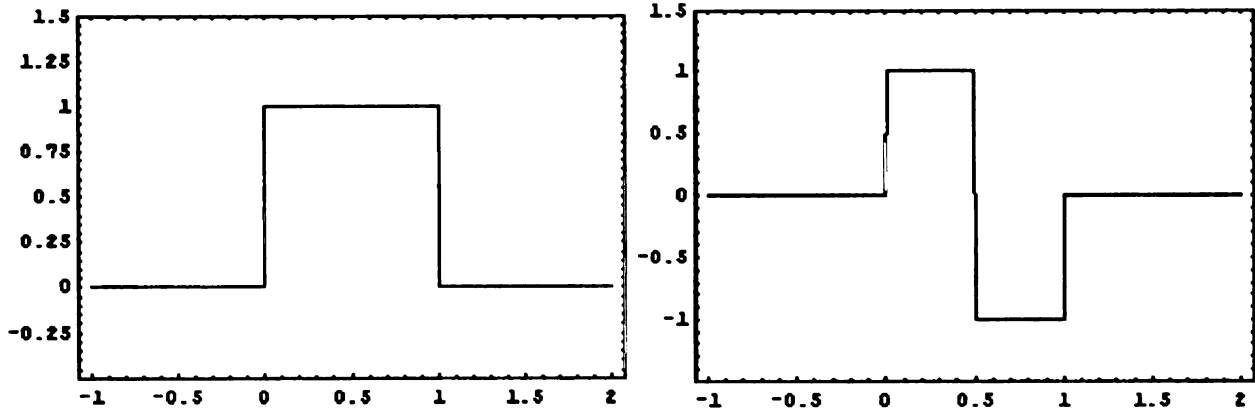
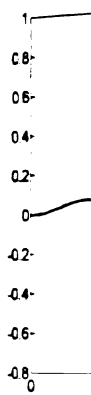


Figure 2.1: Haar scaling function and wavelet

Figure 2.2(a) shows an arbitrary function in its original form and using equation (2.3) this function is approximated by its projection in the space V_6 (2^6 coefficients) as shown in figure 2.2(b). Figures 2.2(c) and 2.2(d) show the projection of this function in the spaces V_5 and W_5 respectively, i.e., the next coarser representation and the detail that has been removed from the representation at scale-6 to create the coarser representation.



Figure

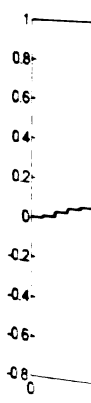


Figure
scale

2.4 Ge

Wave

In applica

properties

comprom

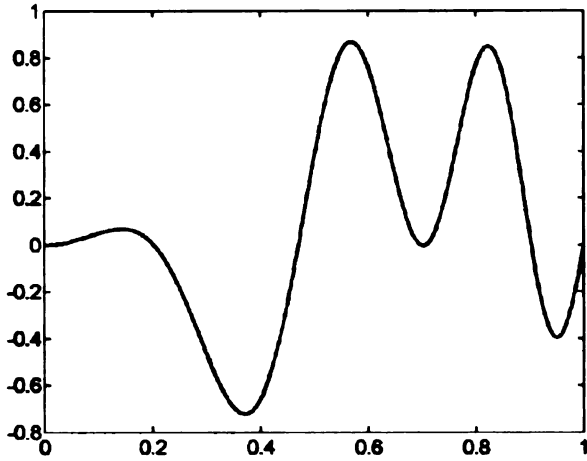


Figure 2.2(a): Original function

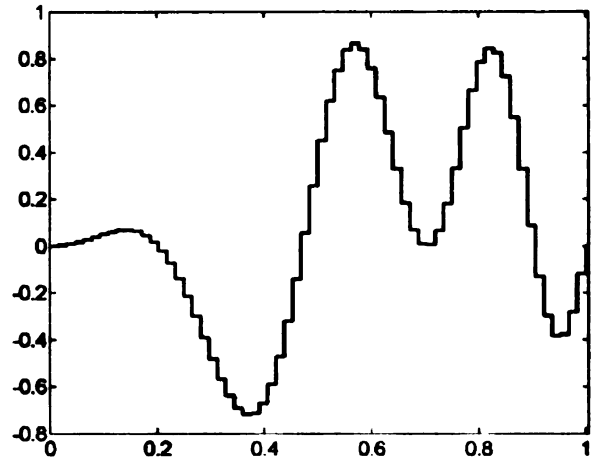


Figure 2.2(b): Approximation at scale 6 (64 data points)

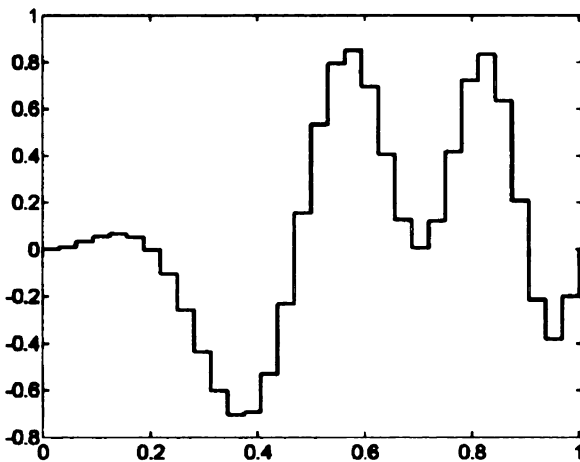


Figure 2.2(c): Approximation at scale 5 (32 data points)

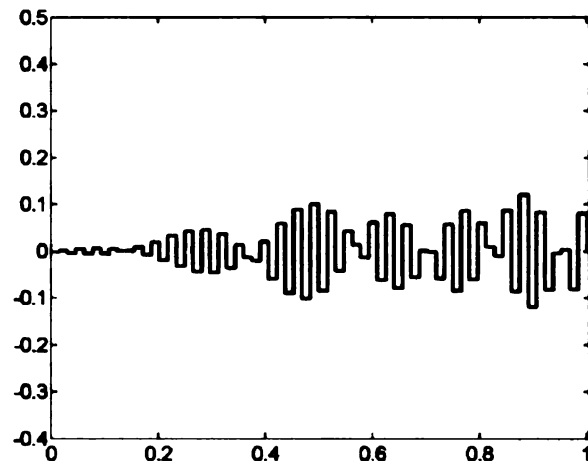


Figure 2.2(d): Detail at scale-5

2.4 Generalized Orthogonal Scaling Functions and Wavelets

In applications involving functional analysis there is a need for basis functions with other properties besides orthogonality such as continuity and differentiability without compromising the compactness of the scaling functions and wavelets involved. Some

important pr

scaling funct

constant coe

on the scaling

where

In order to u

function is us

which leads t

Equation (2.1

Using the ort

important properties of such scaling functions are discussed in this section. A general scaling function $\varphi(x)$ (of dilation factor 2) is a solution to a dilation equation (2.1). The constant coefficients a_k (filter coefficients) are derived by imposing certain conditions on the scaling function such as orthogonality with respect to integer translations,

$$\int \varphi(x)\varphi(x+l)dx = \delta_{0,l} \quad \forall l \in \mathbb{Z} \quad (2.11)$$

where

$$\delta_{0,l} = \begin{cases} 1 & l = 0 \\ 0 & \text{otherwise} \end{cases} \quad (2.12)$$

In order to uniquely define scaling functions of a given shape, the area under the scaling function is usually normalized to unity, i.e.,

$$\int \varphi(x)dx = 1 \quad (2.13)$$

which leads to the following condition on the filter coefficients

$$\sum_{k=-\infty}^{\infty} a_k = 2 \quad (2.14)$$

Equation (2.11) results in the following condition on the filter coefficients

$$\sum_{k=-\infty}^{\infty} a_k a_{k+2l} = 2\delta_{0,l} \quad \forall l \in \mathbb{Z} \quad (2.15)$$

Using the orthogonality of the wavelet function, $\psi(x)$ is defined as

$$\psi(x) = \sum_{k=-\infty}^{\infty} (-1)^k a_{N-1-k} \varphi(2x-k) \quad (2.16)$$

where N is

the interval

and $\{(-1)^k$

The above

coefficient s

wavelets, the

be able to ex

the wavelet a

i.e., the first

moments pro

differentiabili

then

Thus, equatio

coefficient sy

vanishing m

approximation

where N is an even integer and the scaling function and the wavelet are non-zero over the interval $[0, N-1]$ called the *support* of the functions. The sets of coefficients $\{a_k\}$ and $\{(-1)^k a_{N-1-k}\}$ are said to form a pair of *quadrature mirror filters*.

The above equations still do not yield a unique set of filter coefficients. In an N coefficient system, they yield a total of $\frac{N}{2}+1$ equations. For the Daubechies family of wavelets, the other $\frac{N}{2}-1$ equations are determined by requiring the scaling function to be able to exactly represent polynomials of order up to $\frac{N}{2}$. Using the orthogonality of the wavelet and the scaling function this leads to the following condition on the wavelet,

$$\int x^l \psi(x) = 0 \quad l = 0, 1, \dots, \frac{N}{2} - 1 \quad (2.17)$$

i.e., the first $\frac{N}{2}$ moments of the wavelet must be zero. This is known as the *vanishing moments* property of the wavelet and is closely related to the smoothness and differentiability of $\varphi(x)$ and $\psi(x)$. The associated constraint on the filter coefficients is then

$$\sum_{k=-\infty}^{\infty} (-1)^k a_k k^l = 0 \quad l = 0, 1, \dots, \frac{N}{2} - 1 \quad (2.18)$$

Thus, equations (2.14), (2.15) and (2.18) uniquely define the filter coefficients for an N coefficient system. In addition, it is possible to construct wavelet systems by enforcing vanishing moments properties on the scaling functions. This results in better approximation of the expansion coefficients by samples (rather than by orthogonal

projections)

of wavelets

2.5 The

The single s

means of tra

of resolution

for transform

resolution re

Consider a f

and $Q_J f$ de

where $\langle \cdot, \cdot \rangle$

complement c

From equatio

Substituting (

projections) and it causes the scaling function to be more symmetric. The Coiflet-family of wavelets is an example of such systems.

2.5 The Discrete Wavelet Transform

The single stage discrete wavelet transform algorithm of Mallat [28] provides a simple means of transforming functions from one level of resolution, J , to the next coarser level of resolution, $J-1$, called *multi-resolution decomposition or the analysis phase* and one for transforming functions from the coarser level back to the finer level, called *multi-resolution reconstruction or the synthesis phase*.

Consider a function f and let $P_J f$ denote the projection of f onto the subspace V_J and $Q_J f$ denote the projection of f onto the subspace W_J . Thus,

$$P_J f = \sum_{k=-\infty}^{\infty} c_{J,k} \varphi_{J,k}(x), \quad c_{J,k} = \langle f, \varphi_{J,k} \rangle \quad (2.19)$$

$$Q_J f = \sum_{k=-\infty}^{\infty} d_{J,k} \psi_{J,k}(x), \quad d_{J,k} = \langle f, \psi_{J,k} \rangle \quad (2.20)$$

where $\langle \cdot, \cdot \rangle$ denotes the Euclidean inner product. Since W_{J-1} is the orthogonal complement of V_{J-1} in V_J ,

$$P_{J-1} f = P_J f - Q_{J-1} f \quad (2.21)$$

From equation (2.19), it can be seen that

$$c_{J-1,k} = \langle P_{J-1} f, \varphi_{J-1,k} \rangle \quad (2.22)$$

Substituting (2.21) in (2.22),

Also, it ca

Similarly,

in the equa

leads to th

These equ

algorithm i

Consider a

by a vecto

equation (2

vector of co

$$c_{J-1,k} = \frac{1}{\sqrt{2}} \sum_{j=-\infty}^{\infty} c_{J,j} a_{j-2k} \quad (2.23)$$

Also, it can be shown that

$$d_{J-1,k} = \frac{1}{\sqrt{2}} \sum_{j=-\infty}^{\infty} c_{J,j} (-1)^j a_{N-1-j+2k} \quad (2.24)$$

Similarly, substituting the relation

$$P_J f = P_{J-1} f + Q_{J-1} f \quad (2.25)$$

in the equation

$$c_{J,k} = \langle P_J f, \varphi_{J,k} \rangle \quad (2.26)$$

leads to the relation

$$c_{J,k} = \frac{1}{\sqrt{2}} \sum_{j=-\infty}^{\infty} c_{J-1,j} a_{k-2j} + \frac{1}{\sqrt{2}} \sum_{j=-\infty}^{\infty} d_{J-1,j} (-1)^k a_{N-1-k+2j} \quad (2.27)$$

These equations (2.23), (2.24) and (2.27) form the basis of the Mallat transform algorithm implemented using the signal-processing concept of filter-banks as follows.

Consider a periodic, finite dimensional function $f \in V_J$, $\left(= \sum_{k=0}^{n-1} c_{J,k} \varphi_{J,k} \right)$ represented

by a vector of coefficients c_J , where $n = 2^J$ is the period of the function. Then, equation (2.23) in the discrete periodic form represents a circular convolution of the vector of coefficients with a discrete filter of the form

$$\tilde{h} = \frac{1}{\sqrt{2}} [a_0 \ 0 \ 0 \ \cdots \ 0 \ a_{N-1} \ \cdots \ a_2 \ a_1]^T \quad (2.28)$$

followed

vector).

discrete fi

followed

discrete v

single-stag

of such fil

In the fig

illustrated

figure 2.5;

followed by a *dyadic down sampling* (keeping only every other entry of the resulting vector). Similarly, equation (2.24) is represented by the circular convolution of another discrete filter

$$\tilde{g} = \frac{1}{\sqrt{2}} [a_{N-1} \ 0 \ 0 \ \dots \ 0 \ -a_0 \ \dots \ a_{N-3} \ -a_{N-2}]^T \quad (2.29)$$

followed by dyadic down sampling. Thus, the *analysis phase* (decomposition) of the discrete wavelet transform can be illustrated graphically as shown in figure 2.3 for a single-stage transform. Further decompositions are implemented by applying a cascade of such filter-banks recursively to the coarse-scale approximation coefficients, c_j .

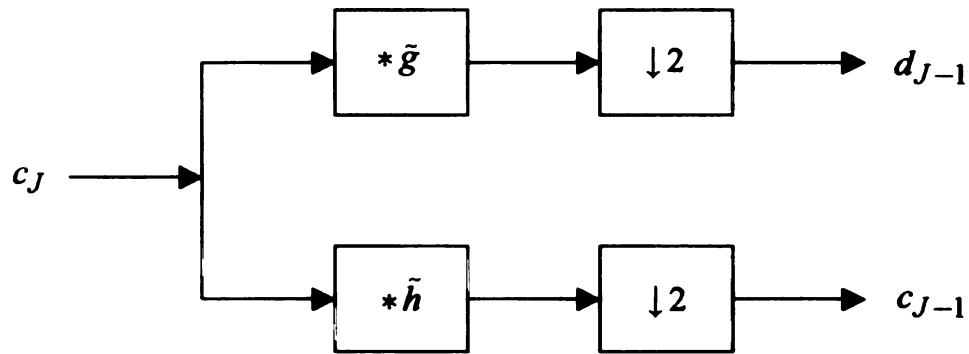


Figure 2.3: Single-stage discrete wavelet decomposition

In the figure, following the standard notation, $*$ represents the convolution operator illustrated in figure 2.4 and \downarrow represents the down sampling operator defined as shown in figure 2.5; all the indices and arguments are evaluated modulo n .

$$x(i) \longrightarrow \boxed{*h} \longrightarrow y(i) = \sum_{k=0}^{n-1} h(k)x(i-k)$$

Figure 2.4: The convolution operation

Similarly,

wavelet t

as illustra

and

Here \uparrow d

\otimes denote

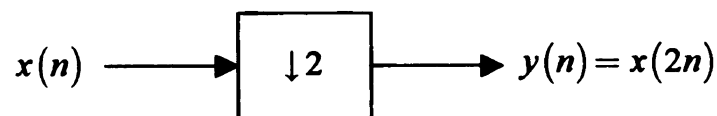


Figure 2.5: The dyadic down sampling operation

Similarly, the discrete periodic form of equation (2.27) leads to the inverse discrete wavelet transform and is implemented by a sequence of convolutions and *up samplings* as illustrated in figure 2.6. The filters in this case are

$$h = \frac{1}{\sqrt{2}} [a_0 \ a_1 \ a_2 \ \dots \ a_{N-2} \ a_{N-1} \ 0 \ \dots \ 0]^T \quad (2.30)$$

and

$$g = \frac{1}{\sqrt{2}} [a_{N-1} \ -a_{N-2} \ a_{N-3} \ \dots \ a_1 \ -a_0 \ 0 \ \dots \ 0]^T \quad (2.31)$$

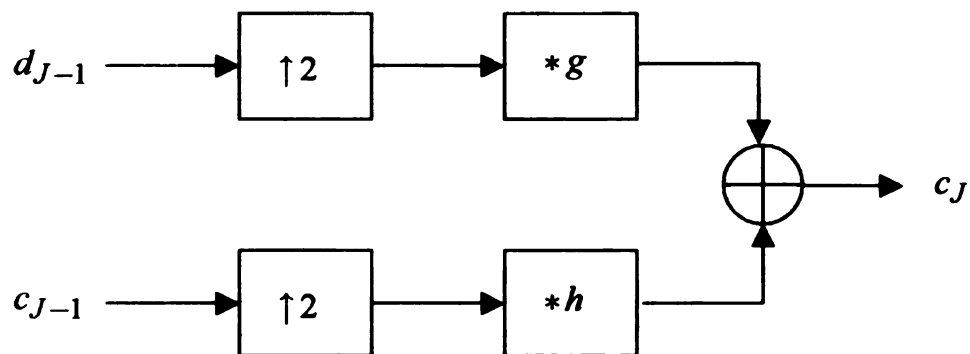


Figure 2.6: Single-stage discrete wavelet reconstruction

Here \uparrow denotes the up sampling operator and can be defined as shown in figure 2.7 and \oplus denotes the addition operator.

In the p
hence all
strictly
convolut
particula
input ve
inverse t
However
influence
transform
using var
etc.

2.6 Co

Wavel

The explic
only the s
accurate f
wavelets c

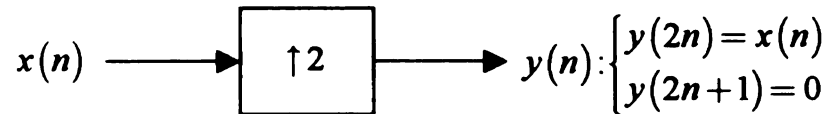


Figure 2.7: The dyadic up sampling operation

In the preceding discussion it is assumed that the associated functions are periodic and hence all the indices and arguments are evaluated modulo n . It is noted that this is not strictly necessary and one could define the same transformations using linear convolutions rather than cyclic convolutions. In the periodic case, the formulation is particularly clean because the total number of terms in the transformed vectors and the input vector are always the same, the transformation matrix is square with a simple inverse that has an interesting structure and can be efficiently calculated using an FFT. However, there is the additional problem due to *aliasing* in the periodic case, this is the influence of the terms in one end of the function affecting the other end due to cyclic transformations. These problems are sometimes overcome by extrapolating the functions using various techniques such as zero padding, symmetric padding, reflective padding, etc.

2.6 Constructing the Basic Scaling Function and Wavelet

The explicit use of the scaling function or wavelet is rare in most applications (one uses only the scaling and wavelet filter coefficients); however, they might be required for accurate function evaluations and visualization. In general, scaling functions and wavelets do not have a closed-form solution. Instead, they have to be computed

recursiv

written c

Evaluati

$$r(j) = c$$

In matrix

or

The vecto

of the mat

In order to

arising from

recursively from the dilation equation (equation 2.1). The dilation equation can be written explicitly as

$$\varphi(x) = a_0\varphi(2x) + a_1\varphi(2x-1) + \dots + a_{N-1}\varphi(2x-N+1) \quad (2.32)$$

Evaluating the above expression for all integer values $x = j \in \mathbb{Z}$, it can be shown that $\varphi(j) = 0$ for $j < 0$ and $j > N-1$. Thus, the only remaining equations are

$$\begin{aligned} \varphi(0) &= a_0\varphi(0) \\ \varphi(1) &= a_0\varphi(2) + a_1\varphi(1) + a_2\varphi(0) \\ \varphi(2) &= a_0\varphi(4) + a_1\varphi(3) + a_2\varphi(2) + a_3\varphi(1) + a_4\varphi(0) \\ &\vdots \\ \varphi(N-2) &= a_{N-3}\varphi(N-1) + a_{N-2}\varphi(N-2) + a_{N-1}\varphi(N-3) \\ \varphi(N-1) &= a_{N-1}\varphi(N-1) \end{aligned} \quad (2.33)$$

In matrix form, this can be written as

$$\begin{bmatrix} a_0 & 0 & 0 & \dots & 0 & 0 & 0 \\ a_2 & a_1 & a_0 & \dots & 0 & 0 & 0 \\ a_4 & a_3 & a_2 & \dots & 0 & 0 & 0 \\ \vdots & \vdots & \vdots & \dots & \vdots & \vdots & \vdots \\ 0 & 0 & 0 & \dots & a_{N-3} & a_{N-4} & a_{N-5} \\ 0 & 0 & 0 & \dots & a_{N-1} & a_{N-2} & a_{N-3} \\ 0 & 0 & 0 & \dots & 0 & 0 & a_{N-1} \end{bmatrix} \begin{bmatrix} \varphi(0) \\ \varphi(1) \\ \varphi(2) \\ \vdots \\ \varphi(N-3) \\ \varphi(N-2) \\ \varphi(N-1) \end{bmatrix} = \begin{bmatrix} \varphi(0) \\ \varphi(1) \\ \varphi(2) \\ \vdots \\ \varphi(N-3) \\ \varphi(N-2) \\ \varphi(N-1) \end{bmatrix} \quad (2.34)$$

or

$$\mathbf{M}\Phi = \Phi \quad (2.35)$$

The vector of integer values of the scaling function (Φ) is then given by the eigenvector of the matrix \mathbf{M} corresponding to the eigenvalue 1, i.e. the solution to the system

$$(\mathbf{M} - \mathbf{I})\Phi = \mathbf{0} \quad (2.36)$$

In order to uniquely determine a solution to the above system a normalizing condition arising from equation (2.13) yields the condition

Thus, the va

(2.36) norm

half-integer

This process

points $\left\{ \frac{j}{2^n} \right\}$

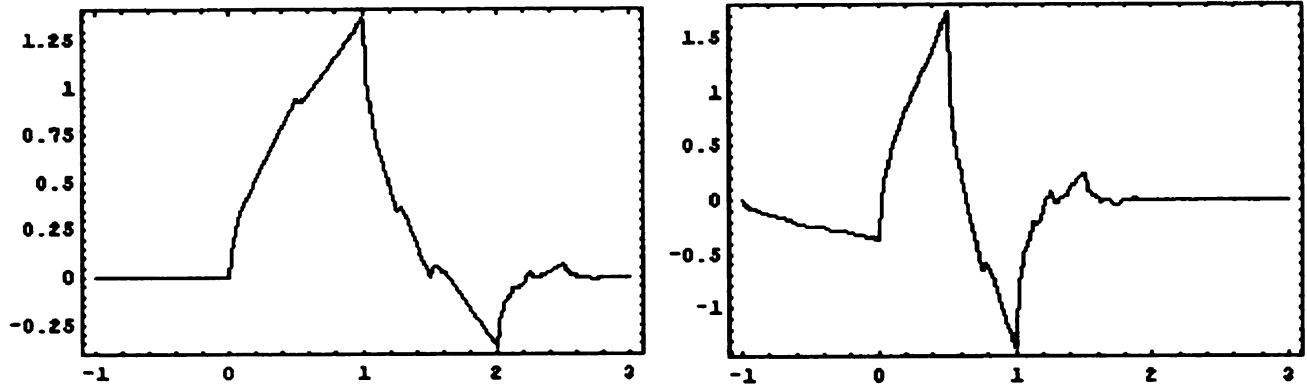
wavelets.

$$\sum_{k=-\infty}^{\infty} \varphi(j) = 1 \quad \forall j \in \mathbb{Z} \quad (2.37)$$

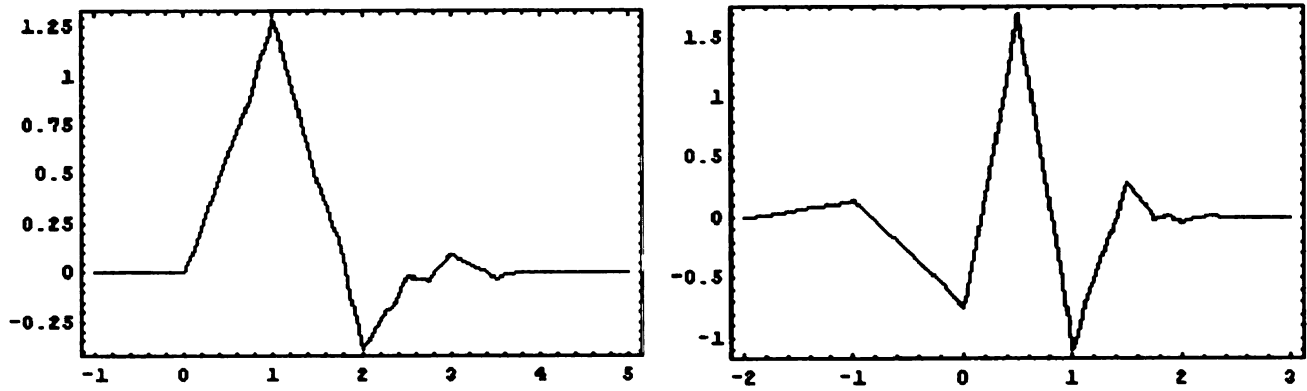
Thus, the values of the scaling function at integers are given by the solution to equation (2.36) normalized by equation (2.37). Once these are computed, the values of $\varphi(x)$ at half-integer points can be determined using the dilation equation as

$$\varphi\left(\frac{x}{2}\right) = \sum_{k=-\infty}^{\infty} a_k \varphi(x-k) \quad (2.38)$$

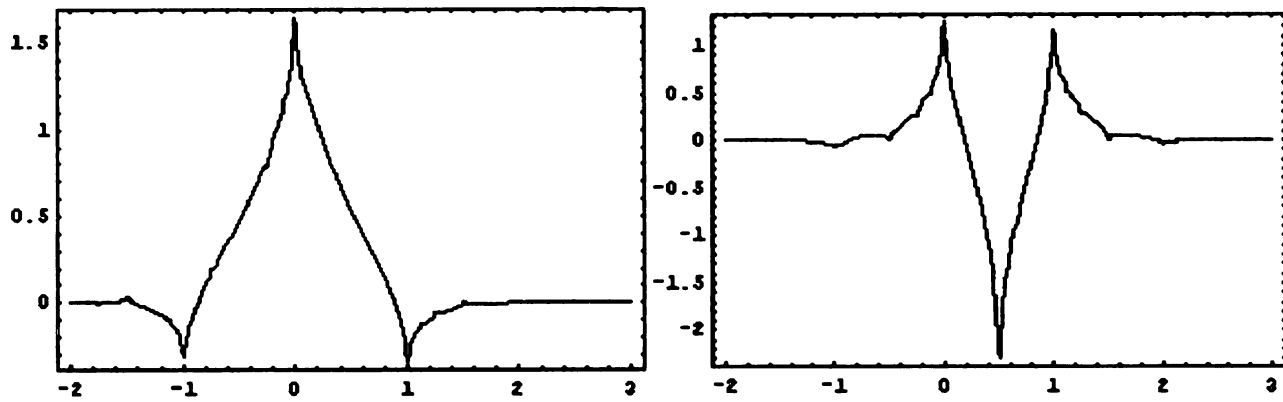
This process is repeated as many times as necessary to find the values $\varphi(x)$ at all dyadic points $\left\{ \frac{j}{2^n}; j, n \in \mathbb{Z} \right\}$. Figure 2.8 shows some commonly used scaling functions and wavelets.



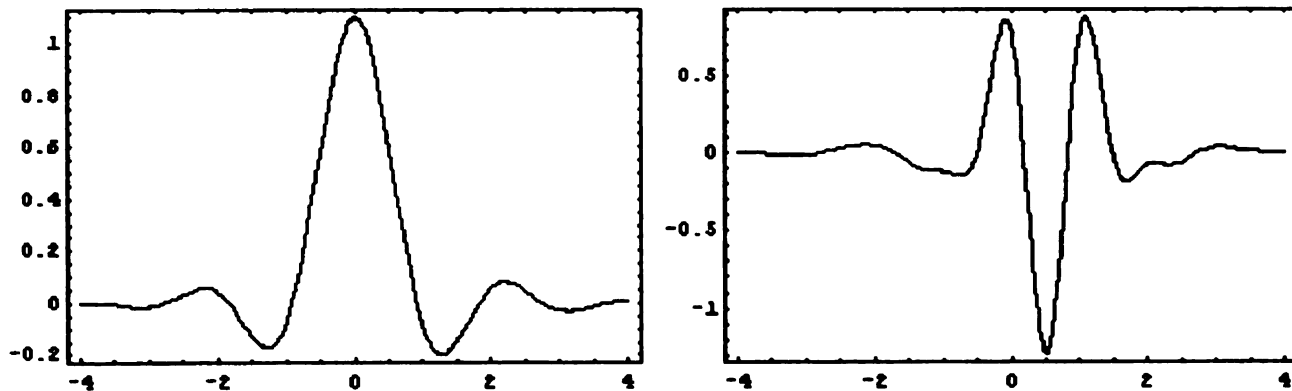
Daubechies-4 scaling function and wavelet



Daubechies-6 scaling function and wavelet



Coiflet-2 scaling function and wavelet



Coiflet-8 scaling function and wavelet

Figure 2.8: Some commonly used orthogonal scaling functions and wavelets

2.7. Fu

Projec

In certain

polynomial

multi-reso

approxima

illustrated

analysis an

Let \mathcal{P}^* a

respectivel

\mathcal{P}^h . For

element fun

original fun

2.7. Function Approximation Using Orthogonal Projections

Projections

In certain applications, functions expressed in some commonly used basis (such as polynomials) need to be approximated in a suitable scaling function basis so that the multi-resolution analysis described earlier could be applied to them. Here, the approximation of functions in a scaling function basis using orthogonal projections is illustrated using a basis of bi-linear (hat) functions used commonly in finite element analysis and the Daubechies D6 scaling functions.

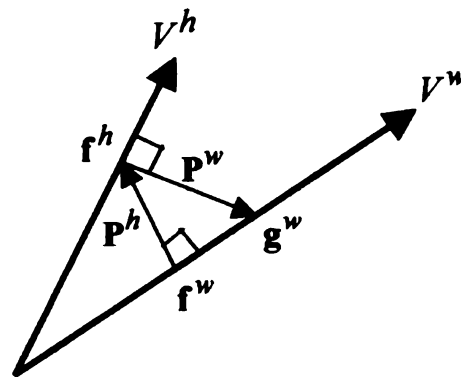


Figure 2.9: Orthogonal projections from wavelet to finite-element spaces

Let V^w and V^h be finite-dimensional spaces of periodic functions in $L^2(\mathbb{R})$, spanned respectively by D6 scaling functions φ^w and bi-linear (finite-element) shape functions φ^h . For any $f^w \in V^w$, let $P^h(f^w) \in V^h$ be the projection onto the space of finite element functions such that the L^2 -norm of the error e , ($e = f^w - P^h(f^w)$) between the original function and the projected function is minimized, i.e.,

$$\forall f^w = \sum_{k=0}^{n-1} f_k^w \varphi_k^w, \quad P^h(f^w) = \sum_{k=0}^{n-1} f_k^h \varphi_k^h \quad (2.39)$$

The stati

In the vec

Here C

wavelet a

integrals a

the compu

problem; f

et al [27]

transforms

as

Consider n

the wavelet

Find $f_k^h \in \mathbb{R}$ that

$$\min \int \left(\sum_{k=0}^{n-1} f_k^w \varphi_k^w(y) - \sum_{k=0}^{n-1} f_k^h \varphi_k^h(y) \right)^2 dy \quad (2.40)$$

The stationary point of equation (2.40) is the solution to

$$\int \left(\sum_{k=0}^{n-1} f_k^w \varphi_k^w \right) \varphi_j^h dy = \int \left(\sum_{k=0}^{n-1} f_k^h \varphi_k^h \right) \varphi_j^h dy \quad (2.41)$$

In the vector form this can be written as

$$\mathbf{C}\mathbf{f}^w = \mathbf{N}\mathbf{f}^h \quad (2.42)$$

$$\Leftrightarrow \mathbf{f}^h = \mathbf{N}^{-1}\mathbf{C}\mathbf{f}^w \quad (2.43)$$

Here \mathbf{C} and \mathbf{N} are block-circulant matrices comprising of the inner products of the wavelet and hat functions, $\int \varphi_k^w \varphi_j^h dy$ and $\int \varphi_k^h \varphi_j^h dy$, respectively. Values of these integrals are commonly referred to as *connection coefficients*. Using the scaling relation, the computation of these quantities is usually reduced to the solution of an eigenvector problem; for details regarding the computation of these connection coefficients, see Latto et al [27], Dahmen and Michelli [9], Kunoth [26]. Thus a projection matrix that transforms vectors in the wavelet space to that in the finite element space can be written as

$$\mathbf{P}^h = \mathbf{N}^{-1}\mathbf{C} \quad (2.44)$$

Consider now, the projection, $P^w(f^h)$ of a given finite-element function $f^h \in V^h$ onto the wavelet space. As before, the statement of the projection problem can be written as

$$\forall f^h = \sum_{k=0}^{n-1} f_k^h \varphi_k^h \in V^h, \quad P^w(f^h) = \sum_{k=0}^{n-1} g_k^w \varphi_k^w \quad (2.45)$$

The station

(Note: $\{ \}$)

(Compare

that transfo

written as

where, the

2.8 Wav

In the prec

dimensional

tensor prod

functions at

where F_j is

scaling functi

Find $g_k^w \in \mathbb{R}$ that

$$\min \int \left(\sum_{k=0}^{n-1} f_k^h \varphi_k^h(y) - \sum_{k=0}^{n-1} g_k^w \varphi_k^w(y) \right)^2 dy \quad (2.46)$$

The stationary point of equation (2.46) is the solution to

$$\int \left(\sum_{k=0}^{n-1} f_k^h \varphi_k^h \right) \varphi_j^w dy = \int \left(\sum_{k=0}^{n-1} g_k^w \varphi_k^w \right) \varphi_j^w dy = g_j^w \quad (2.47)$$

(Note: $\{\varphi_k^w, k \in [0, n-1]\}$ forms an orthonormal basis for V^w). In vector form this is,

$$\mathbf{C}^T \mathbf{f}^h = \mathbf{f}^w \quad (2.48)$$

(Compare the left hand sides of equations (2.41) and (2.47)). Thus a projection matrix that transforms vectors in the finite-element space to that in the wavelet space can be written as

$$\mathbf{P}^w = \mathbf{C}^T \quad (2.49)$$

where, the matrix \mathbf{C} is the same as the one defined earlier.

2.8 Wavelets In Multiple Dimensions

In the preceding discussions it is assumed that the associated functions are one-dimensional. In higher dimensions, the wavelet and scaling functions are defined as tensor products of the respective functions in 1-D. The space of two-dimensional functions at a scale J is given as

$$\mathbf{V}_J = V_J \otimes V_J \quad (2.50)$$

where V_J is the corresponding space of 1-D functions. For example, a two-dimensional scaling function is defined as follows:

All the
functions
fixed (fin

It follows
 $J-1$ can

Thus, a mu
notation as

where the co
and the deta

$$\varphi_{J,kl}(x, y) = \varphi_{J,k}(x)\varphi_{J,l}(y) \quad (2.51)$$

All the concepts discussed can then be extended to this tensor product of scaling functions. Thus a two-dimensional periodic function, $u(x, y)$, can then be expressed at a fixed (fine) scale J as

$$u_J(x, y) = P_J u(x, y) = \sum_{k,l=0}^{N-1} u_{kl}^J \varphi_{J,kl}(x, y) = \sum_{k,l=0}^{N-1} u_{kl}^J \varphi_{J,k}(x)\varphi_{J,l}(y) \quad (2.52)$$

It follows from using (2.4) in (2.50) that the coarse-space and the detail space at scale $J-1$ can be expressed as

$$\begin{aligned} \mathbf{V}_{J-1} &= V_{J-1} \otimes V_{J-1} \\ \mathbf{W}_{J-1} &= (W_{J-1} \otimes W_{J-1}) \oplus (V_{J-1} \otimes W_{J-1}) \oplus (W_{J-1} \otimes V_{J-1}) \end{aligned} \quad (2.53)$$

Thus, a multi-resolution representation of this function can be expressed using a compact notation as,

$$u_J(x, y) = \sum_{k,l=0}^{n-1} \bar{u}_{kl} \varphi_{j,kl}(x, y) + \sum_{m=j}^{J-1} \sum_{k,l=0}^{2^m-1} \sum_{r=1}^3 \tilde{u}_{m,kl}^r \psi_{m,kl}^r(x, y) \quad (2.54)$$

where the coarse-scale basis function,

$$\varphi_{j,kl}(x, y) = \varphi_{j,k}(x)\varphi_{j,l}(y) \quad (2.55)$$

and the detail basis functions are denoted as

$$\begin{aligned} \psi_{m,kl}^1(x, y) &= \psi_{m,k}(x)\varphi_{m,l}(y) \\ \psi_{m,kl}^2(x, y) &= \varphi_{m,k}(x)\psi_{m,l}(y) \\ \psi_{m,kl}^3(x, y) &= \psi_{m,k}(x)\psi_{m,l}(y) \end{aligned} \quad (2.56)$$

It should

reduces t

decompo



Origin

Figur

It should be noted that each reduction of a discrete, periodic two-dimensional function reduces the size of the coarse-scale vector of coefficients by a factor of 4. A two-stage decomposition of a two-dimensional function can be illustrated as shown in Figure 2.10.

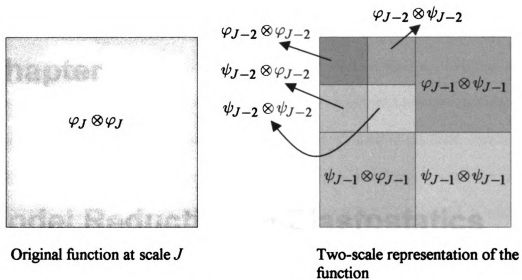


Figure 2.10: A multi-scale representation of two-dimensional functions

Cha

Mod

This chap
the analy
resolution
and behav
method ca
blocks to
design for
efficiency.
are strongl
bodies; this
analysis of s

Chapter 3

Model Reduction in Elastostatics

This chapter deals with methods to consistently reduce the size of some models used in the analysis of large structural systems. The reduction is accomplished using a multi-resolution analysis applied to differential operators to average the fine-scale properties and behavior while retaining the coarse-scale information. In the discrete form this method can be used to construct small stiffness matrices that can be used as building blocks to construct larger systems. An application of this scheme is proposed to be in design for crash-worthiness, where intensive computations demand computational efficiency. It is noted that the models of structural systems for crashworthiness analysis are strongly nonlinear and involve other phenomena such as contact between rigid bodies; this work is only a starting step towards such a comprehensive scheme for the analysis of such models by considering the analysis of structures in linear elastostatics.

This c
introdu
problem
multi-re
section 2
the displ
proposed
in section
suitable fo
parameters
Finally, nu
presented in

3.1. Sca

Let S repre
be modeled

Let S^J be

Here the ind
discretized a

Upon discre

This chapter is arranged as follows: The notion of scales in structural systems is introduced in section 3.1. This is followed by a discussion of the discretized elasticity problem at a fixed (fine) scale in section 3.2. A model reduction technique based on a multi-resolution analysis of the material distribution is presented in section 3.3. In section 3.4, a model reduction strategy based on a periodic multi-resolution analysis of the displacements is presented. This is followed by comparisons between the two proposed reduction schemes as well as that with the classical homogenization technique in section 3.5. Section 3.6 deals with computing a reduced stiffness matrix that is suitable for assembly with other stiffness matrices. A technique to compute fine-scale parameters using the reduced solution, called *augmentation*, is presented in section 3.7. Finally, numerical examples that illustrate and compare the methods discussed are presented in section 3.8.

3.1. Scales And Material Properties In Elasticity

Let S represent a structure of interest. The relevant behavior of S in linear elasticity can be modeled by a linear system of the form

$$L(u) = f + \text{boundary conditions} \quad (3.1)$$

Let S^J be a model of the structure that incorporates all of its details up to a scale J . Here the index J is used to denote the level of refinement at which the structure has been discretized and it is chosen such that all the relevant features of the structure are resolved. Upon discretization, the elasticity equation (3.1) becomes

$$\mathbf{L}_J \mathbf{u}_J = \mathbf{f}_J \quad (3.2)$$

where \mathbf{E}
displacement
open for
of the st
More exp
to the eq

accounts
in finite el
of certain
is usually c
decide whi
cases, ther
freedom. F
periodic ho
varying mat
scales prese
by assuming

where $E_{ijkl}^{(0)}$
dimension c
context, ρ

where \mathbf{L}_J is a stiffness matrix, \mathbf{f}_J is the force vector and \mathbf{u}_J is a vector of unknown displacements. The specific choice of the basis functions used in the discretization is left open for the time being. We are interested in whether we can reduce the size (dimension) of the stiffness matrix in (3.2) and still retain all the *relevant* information present in \mathbf{u}_J . More explicitly, the question is: Is there an operator \mathbf{H}_{J-k} such that the solution $\bar{\mathbf{u}}_{J-k}$ to the equation

$$\mathbf{H}_{J-k} \bar{\mathbf{u}}_{J-k} = \mathbf{f}_{J-k} \quad (3.3)$$

accounts for all the relevant information present in \mathbf{u}^J ? This question is a familiar one in finite element analysis, where this is usually accomplished using a *static condensation* of certain unwanted degrees of freedom, e.g., see Wilson [38]. However, this procedure is usually done as an ad hoc scheme, i.e., there is no general set of rules that help one to decide which degrees of freedom to condense out and which to retain. Also, in some cases, there is no physical meaning or basis associated with the condensed degrees of freedom. Here we consider an approach that is more closely related to the methods of periodic homogenization used in the computation of effective properties of rapidly varying materials. We associate the different scales of detail in the structure S with the scales present in the geometric layout of the material in the structure. This is facilitated by assuming that the material distribution in the structure can be expressed as

$$E_{ijkl}(\underline{x}) = \rho(\underline{x}) E_{ijkl}^0 \quad (3.4)$$

where E_{ijkl}^0 is a known, reference material tensor and $\rho: \mathbb{R}^n \rightarrow (0, 1]$ (n is the spatial dimension of the model) characterizes the spatial distribution of the material. In this context, ρ is commonly known as the effective density function. This material model is

frequently

Thus, we

density fun

We

an assembl

3.1.

Here $\Omega =$

$x = \bar{x}_c + y$

y is a coord

as

Also, it may

structure as

problem of

reduced stif

a structure

standard fin

frequently used in solving structural topology optimization problems, e.g.. see [33]. Thus, we associate the scales present in the model to the scales present in the relative density function.

We are interested in structures whose material distributions can be expressed as an assembly of several sub-domains (called here *substructures*) as illustrated in figure 3.1.

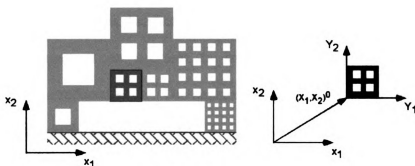


Figure 3.1: A structure built from substructures of different scales.

Here $\Omega = \bigcup \Omega_c$, where Ω_c is a substructure. Any point x in Ω_c can be expressed as $x = \bar{x}_c + y$, where \bar{x}_c is the global coordinate of a reference point in the substructure and y is a coordinate local to the substructure. Then we can express the material distribution as

$$\rho(x) = \rho(\bar{x}_c, y) \quad (3.5)$$

Also, it may be possible (and desirable) to express the stiffness matrix associated with the structure as an assembly of matrices corresponding to each substructure. Thus the problem of finding a reduced model of the structure becomes a problem of finding reduced stiffness matrices corresponding to each individual substructure. The concept of a structure being divided into substructures is similar to the notion of super-elements in standard finite-element analysis.

The
homogeniz
a mixture o
with a fre
infinitesim
(weak limit
scales in w
the averag
displacemen
described in

3.2. The

The plane-s
such that

where $\varepsilon(u)$
traction on
 E is the el
elastic tensor

The above formulation of the problem has obvious similarities to that in periodic homogenization, where the goal is to find the effective material tensor that corresponds to a mixture of materials. The mixture is characterized by a cell that is repeated periodically with a frequency $1/\varepsilon$, ($\varepsilon \rightarrow 0$), i.e., material variation is assumed to take place at infinitesimal scales. Such problems are solved using asymptotic expansion techniques (weak limits) and the result is a homogenized material tensor. In the present problem the scales in which the material is distributed in Ω are of finite dimensions and the result of the averaging process is an operator (a stiffness matrix) that relates loads and displacements in the reduced scale. The construction and reduction of the operators are described in the following sections.

3.2. The Fine-Scale Elasticity Problem

The plane-stress elasticity problem on a prescribed domain $\Omega = \cup \Omega_c$ seeks $u \in V(\Omega)$

such that

$$\int_{\Omega} E \varepsilon(u) \varepsilon(v) d\Omega = \int_{\Gamma^t} t \cdot v d\Gamma \quad \forall v \in V^0(\Omega) \quad (3.6)$$

where $\varepsilon(u)$ is the strain tensor associated with the displacement u ; t is an applied traction on the boundary Γ^t ; V is a space of kinematically admissible displacements and E is the elastic tensor defined on Ω . Using the material model described earlier the elastic tensor within each substructure is expressed in the form

$$E(y) = \rho^c E^0 \quad (3.7)$$

where E^0

a substruct

problem de

where the s

we assume

with jump

called the s

discretizati

Ω_c is resol

is the value

that resolve

from substr

We

discretized

discretizatio

e.g., using f

scale stiffne

stiffness ma

reduction.

where E^0 is a reference material tensor, ρ^c characterizes the material distribution within a substructure and $y \in \Omega_c$ is a coordinate system local to the substructure. The elasticity problem defined on Ω is now:

$$\sum_c \int_{\Omega_c} E(y) \varepsilon(u) \varepsilon(v) dy = \int_{\Gamma^t} t \cdot v d\Gamma \quad \forall v \in V^0(\Omega) \quad (3.8)$$

where the sum is interpreted in the sense of assembly. In order to facilitate computations we assume that ρ^c is resolved with sufficient accuracy by a piecewise constant function with jump discontinuities at Cartesian grid lines spaced $S_c = 2^{-J} L_c$ units apart (S_c is called the *scale* of the discretization), for some positive integer J called the level of the discretization. L_c is the length of a side of the substructure. In practice, the geometry in Ω_c is resolved by a digital image composed of $2^J \times 2^J$ pixels of size $S_c \times S_c$, where ρ_{kl}^J is the value of ρ^c at the center of the pixel (k, l) . S_c and J are a measure of the scale that resolves ρ^c . We denote this by writing $\rho^c(y) \equiv \rho_J^c(y)$. Both S_c and J may vary from substructure to substructure.

We refer to (3.8) as the fine-scale problem when all the substructures are discretized at their finest scale. In the typical problems of interest such a fine-scale discretization results in a system with too many degrees of freedom for efficient analysis, e.g., using finite elements. The large size of the fine-scale problem requires that the fine-scale stiffness matrix associated with each substructure be replaced by an equivalent stiffness matrix of a smaller dimension obtained through some consistent process of reduction. Here we propose two such reduction strategies: one based on a multi-

resolution

multi-res

inexpens

particula

displacem

resolution

rigorous

relatively

3.3 A

Distrib

An approx

using a w

is resolved

where the

pixel (k, l)

and detail

implemente

splits functi

resolution analysis of the material distribution functions ρ^c and the other based on a multi-resolution analysis of the displacements u . The first approach is computationally inexpensive but crude. It is used where there is no necessity to go from the solution at a particular discretization level to another, i.e., there is no consistent procedure linking the displacements at different levels of discretization. The second strategy, based on a multi-resolution analysis of displacements, is a more consistent procedure and provides a rigorous link between the displacements at various levels of discretization, but it is relatively a computationally expensive approach.

3.3 A Multi-Resolution Analysis of the Material Distribution

An approximation scheme based on a representation of material distribution function ρ^c using a wavelet expansion is presented. If the material distribution in a substructure Ω_c is resolved by a $2^J \times 2^J$ digital image, we can write

$$\rho^c(y) = \rho_J^c(y) = \sum_{k,l=0}^{N-1} \rho_{kl}^J \varphi_{J,kl}(y) \quad (3.9)$$

where the functions $\varphi_{J,kl}$ are 2D Haar scaling functions, i.e., piecewise constant over the pixel (k,l) and $N = 2^J$. A wavelet expansion of this function splits ρ^c into coarse-scale and detail functions, $\bar{\rho}(y)$ and $\tilde{\rho}(y)$, respectively. The transformation is easily implemented using a 2-D discrete wavelet transform. More specifically, the transform splits functions $\rho^c \in V_J$, a space of dimension $2^{2J} = N^2$, into functions $\bar{\rho} \in V_{J-1}$ and

$\bar{\rho} \in W_{J-1}$.

dimension

coarse spa

decomposi

The coarse

and $n = 2^k$

tensor prod

of ρ^c over

function $\bar{\rho}$

tensor

is an arithme

A substruct

substructure

harmonic av

$\tilde{\rho} \in W_{J-1}$, where W_{J-1} is the orthogonal complement of V_{J-1} in V_J . Space V_{J-1} is of dimension $2^{2(J-1)} = N^2/4$, i.e., each application of the wavelet transform reduces the coarse space by a factor of four. After several applications of the wavelet transform the decomposition is of the form

$$\begin{aligned} \rho(y) &= \sum_{k,l=0}^{N-1} \rho_{kl}^J \varphi_{J,kl}(y) \\ &= \sum_{k,l=0}^{n-1} \bar{\rho}_{kl} \varphi_{j,kl}(y) + \sum_{m=j}^{J-1} \sum_{k,l=0}^{2^m-1} \sum_{r=1}^3 \tilde{\rho}_{kl}^{m,r} \psi_{m,kl}^r(y) \end{aligned} \quad (3.10)$$

The coarse-scale function is of the form

$$\bar{\rho} \doteq \sum_{k,l=0}^{n-1} \bar{\rho}_{kl} \varphi_{j,kl}(y) \quad (3.11)$$

and $n = 2^j$. Here the 2D scaling functions $\varphi_{j,kl}(y)$ and the wavelets $\psi_{j,kl}(y)$ are tensor products of their corresponding 1D functions. Coefficients $\bar{\rho}_{kl}$ are average values of ρ^c over pixels of size $\Delta = 2^{-j} L_c$ in an equally spaced grid of size $n \times n$. The function $\bar{\rho}(y)$ is nothing but an arithmetic average of ρ^J and in view of (3.7), the elastic tensor

$$E_A(y) = \bar{\rho}(y) E^0 \quad (3.12)$$

is an arithmetic average of $E(y)$ over the substructure.

A substructure made of material E_A would over-estimate the stiffness of the original substructure, as $E_A(y)$ is an upper bound for $E(y)$. To compensate, we shall look for a harmonic average of $E(y)$. For this purpose we define the function

1

when

coar

from

by 1

corre

is a 1

E_H

used

and t

This a

a fine

$$\theta_J^c(\mathbf{y}) = \sum_{k,l=0}^{N-1} \theta_{kl}^J \varphi_{J,kl}(\mathbf{y}) \quad (3.13)$$

where $\theta_{kl}^J \doteq 1/\rho_{kl}^J$. A multi-resolution analysis of this fine-scale function produces a coarse representation

$$\bar{\theta}(\mathbf{y}) = \sum_{k,l=0}^{n-1} \bar{\theta}_{kl} \varphi_{j,kl}(\mathbf{y}) \quad (3.14)$$

from which we can define

$$\underline{\rho}(\mathbf{y}) = \sum_{k,l=0}^n \underline{\rho}_{kl} \varphi_{j,kl}(\mathbf{y}) \quad (3.15)$$

by letting $\underline{\rho}_{kl} \doteq 1/\bar{\theta}_{kl}$. The function $\underline{\rho}$ is a harmonic average of ρ^J and the corresponding elastic tensor is then

$$E_H(\mathbf{y}) = \underline{\rho}(\mathbf{y}) E^0 \quad (3.16)$$

is a harmonic average of $E(\mathbf{y})$ over the substructure. A substructure made of material E_H would under estimate the stiffness of the original substructure. E_A and E_H are used to define an effective material for substructure Ω_c as the weighted average

$$\bar{E}_j^c = \alpha E_A + (1-\alpha) E_H, \quad \alpha \in [0,1] \quad (3.17)$$

and the corresponding material distribution function $\rho_j^c(\mathbf{y})$ as

$$\rho_j^c(\mathbf{y}) = \alpha \bar{\rho}(\mathbf{y}) + (1-\alpha) \underline{\rho}(\mathbf{y}), \quad \alpha \in [0,1] \quad (3.18)$$

This average approximates the material properties of the substructure when reduced from a fine level J to a coarse level $j < J$. Using these properties and a finite element

discretization of equally spaced elements of size $\Delta = 2^{-j} L_c$ an effective stiffness matrix \mathbf{K}_j^c of dimension $2(n+1)^2 \times 2(n+1)^2$ can be constructed by assembling n^2 standard finite element matrices per substructure, i.e.,

$$\mathbf{K}_j^c = \sum_{k,l=1}^n \left(\rho_j^c \right)_{k,l} \mathbf{k}^0 \quad (3.19)$$

Here, \mathbf{k}^0 is the stiffness matrix of a four-noded square finite element made of material E^0 . The reduced substructure can be interpreted as a super-element whose stiffness matrix \mathbf{K}_j^c can be used as a building block in an assembly of other substructures following the usual rules for assembly.

3.4 A Multi-Resolution Analysis of the Displacement

The matrix \mathbf{K}_j constructed in the earlier section (3.19) is based on a multi-resolution analysis of the material distribution alone and thus it is only an approximation to the effective properties of a substructure. This approximation is surprisingly accurate and is sufficient for problems with simple microstructures. However, a more consistent analysis may be required when detailed representations of the small-scale effects are of interest. One such analysis is based on numerical homogenization using a multi-resolution analysis of the displacements.

3.4.1 A Periodic Multi-Resolution Reduction Scheme

The variational form (or weak form) of the plane elasticity problem defined on a single periodic substructure discretized at its finest scale can be written as

$$\int_{\Omega_c} E(\mathbf{y}) \varepsilon(\mathbf{u}) \varepsilon(\mathbf{v}) d\mathbf{y} = \int_{\Omega_c} \mathbf{f} \mathbf{v} d\mathbf{y}, \quad \forall \mathbf{u}, \mathbf{v} \in V_P(\Omega_c) \quad (3.20)$$

where

$$V_P(\Omega_c) = \{\mathbf{u} \in H^1(\Omega_c) : \mathbf{u} \text{ is } \Omega_c \text{ - periodic}\} \quad (3.21)$$

and the body force \mathbf{f} has mean-value of zero in Ω_c . This problem is solved using a wavelet-Galerkin technique, outlined briefly here (for further details about the technique refer Diaz [14], DeRose and Diaz [11] and the references therein). The tensor of elastic properties $E(\mathbf{y})$ and the trial and weight functions \mathbf{u}, \mathbf{v} are approximated as follows:

$$\begin{aligned} E(\mathbf{y}) &= \sum_{k,l=0}^{2^J-1} E_{kl}^J \varphi_{J,kl}^{Haar}(\mathbf{y}) \\ \mathbf{u}(\mathbf{y}) &= \sum_{k,l=0}^{2^J-1} \mathbf{u}_{kl}^J \varphi_{J,kl}(\mathbf{y}) \\ \mathbf{v}(\mathbf{y}) &= \sum_{k,l=0}^{2^J-1} \mathbf{v}_{kl}^J \varphi_{J,kl}(\mathbf{y}) \end{aligned} \quad (3.22)$$

where the coefficients E_{kl}^J , \mathbf{u}_{kl}^J and \mathbf{v}_{kl}^J are wavelet coefficients associated with pixel (k, l) in a J -level discretization of substructure Ω_c . The material tensor is approximated using the piece-wise constant Haar scaling functions $\varphi^{Haar}(\mathbf{y})$ as the function $E(\mathbf{y})$ has to satisfy only minimal continuity requirements whereas the displacement functions need to satisfy sufficient smoothness conditions. Daubechies (D6) functions $\varphi(\mathbf{y})$ are used to approximate displacements. Using the approximations (3.22) into (3.20) yields a $2N^2 \times 2N^2$ linear system of equations

$$\mathbf{L}_J \mathbf{u}_J = \mathbf{f}_J \quad (3.23)$$

where the mesh size that resolves ρ^c is $N \times N$, $N = 2^J$ and \mathbf{L} is of the form

$$\mathbf{L} = \begin{bmatrix} \mathbf{L}_J^{xx} & \mathbf{L}_J^{xy} \\ \mathbf{L}_J^{yx} & \mathbf{L}_J^{yy} \end{bmatrix} \quad (3.24)$$

In equation (3.24)

$$\begin{aligned} L_{J,klmn}^{xx} &= \sum_{p,q} E_{pq}^{J,11} C_{pqklmn}^{1,0,1,0} + E_{pq}^{J,33} C_{pqklmn}^{0,1,0,1} \\ L_{J,klmn}^{xy} &= \sum_{p,q} E_{pq}^{J,33} C_{pqklmn}^{0,1,1,0} + E_{pq}^{J,12} C_{pqklmn}^{1,0,0,1} \\ L_{J,klmn}^{yx} &= \sum_{p,q} E_{pq}^{J,33} C_{pqklmn}^{1,0,0,1} + E_{pq}^{J,12} C_{pqklmn}^{0,1,1,0} \\ L_{J,klmn}^{yy} &= \sum_{p,q} E_{pq}^{J,22} C_{pqklmn}^{0,1,0,1} + E_{pq}^{J,33} C_{pqklmn}^{1,0,1,0} \end{aligned} \quad (3.25)$$

where

$$E_{pq}^J = \begin{bmatrix} E_{pq}^{J,11} & E_{pq}^{J,12} & 0 \\ E_{pq}^{J,12} & E_{pq}^{J,22} & 0 \\ 0 & 0 & E_{pq}^{J,33} \end{bmatrix}$$

The terms

$$C_{pqklmn}^{\alpha,\beta,\xi,\zeta} = \left[\int_{\Omega} \varphi_{J,p}^E(x) D^\alpha \varphi_{J,k}^u(x) D^\xi \varphi_{J,m}^u(x) dx \right] \times \left[\int_{\Omega} \varphi_{J,q}^E(y) D^\beta \varphi_{J,l}^u(y) D^\zeta \varphi_{J,n}^u(y) dy \right]$$

are called *connection coefficients* and depend only on the choice of basis functions. D^i denotes a derivative operator (several algorithms are available to compute these coefficients, see Kunoth [26]). \mathbf{L}_J is the stiffness matrix associated with a material distribution ρ^c discretized at the finest scale S_c . It is the most detailed representation of

the substructure but it is too large to be useful in computations involving many substructures. We reduce \mathbf{L}_J using a multi-resolution analysis that splits \mathbf{u}_J into coarse-scale and fine detail components $\bar{\mathbf{u}}$ and $\tilde{\mathbf{u}}$ respectively.

Consider the system represented in equation (3.23) and let the associated space of functions be V^J , i.e., $\mathbf{L}_J: V^J \rightarrow V^J$ and $\mathbf{u}_J, \mathbf{f}_J \in V^J$. Define \mathcal{W} to be the transformation

$$\mathcal{W}: V^J \rightarrow V^{J-1} \oplus W^{J-1} \quad (3.26)$$

that maps a function in the space V^J into functions in the space V^{J-1} and its orthogonal complement W^{J-1} . The orthogonal transformation

$$\mathcal{W}\mathbf{u}_J = \begin{bmatrix} \mathbf{P}_{J-1}\mathbf{u}_J \\ \mathbf{Q}_{J-1}\mathbf{u}_J \end{bmatrix} = \begin{bmatrix} \bar{\mathbf{u}}_{J-1} \\ \tilde{\mathbf{u}}_{J-1} \end{bmatrix} \quad (3.27)$$

represents the splitting of a vector \mathbf{u}_J into its coarse scale component $\bar{\mathbf{u}}_{J-1}$ and the details $\tilde{\mathbf{u}}_{J-1}$, where the operators $\mathbf{P}_{J-1}: V^J \rightarrow V^{J-1}$ and $\mathbf{Q}_{J-1}: V^J \rightarrow W^{J-1}$ are the coarse and detail projection operators respectively. The equation (3.23) can now be expanded as follows:

$$\mathcal{W}\mathbf{L}_J\mathcal{W}^T(\mathcal{W}\mathbf{u}_J) = \begin{bmatrix} \mathbf{L}_{J-1} & \mathbf{C}_{J-1} \\ \mathbf{C}_{J-1}^T & \mathbf{A}_{J-1} \end{bmatrix} \begin{bmatrix} \bar{\mathbf{u}}_{J-1} \\ \tilde{\mathbf{u}}_{J-1} \end{bmatrix} = \begin{bmatrix} \bar{\mathbf{f}}_{J-1} \\ \tilde{\mathbf{f}}_{J-1} \end{bmatrix} \quad (3.28)$$

where,

$$\begin{aligned} \mathbf{A}_{J-1} &= \mathbf{Q}_{J-1}\mathbf{L}_J\mathbf{Q}_{J-1}: W^{J-1} \rightarrow W^{J-1} \\ \mathbf{C}_{J-1} &= \mathbf{P}_{J-1}\mathbf{L}_J\mathbf{Q}_{J-1}: W^{J-1} \rightarrow V^{J-1} \\ \mathbf{L}_{J-1} &= \mathbf{P}_{J-1}\mathbf{L}_J\mathbf{P}_{J-1}: V^{J-1} \rightarrow V^{J-1} \end{aligned} \quad (3.29)$$

Here $\bar{\mathbf{f}}_{J-1}$ and $\tilde{\mathbf{f}}_{J-1}$ are the coarse-scale and detail components of the external force.

The coarse scale component of the displacements $\bar{\mathbf{u}}_{J-1}$ is found by block Gauss elimination, which yields the equation

$$\left(\mathbf{L}_{J-1} - \mathbf{C}_{J-1} \mathbf{A}_{J-1}^{-1} \mathbf{C}_{J-1}^T\right) \bar{\mathbf{u}}_{J-1} = \bar{\mathbf{f}}_{J-1} - \mathbf{C}_{J-1} \mathbf{A}_{J-1}^{-1} \tilde{\mathbf{f}}_{J-1} \quad (3.30)$$

For the class of operators of interest here it can be shown that the operator \mathbf{A}_{J-1} is indeed invertible. This can be proved for our prototype problem in 2D elasticity as follows (The result can be extended to other cases easily). A 2D elastic stiffness matrix \mathbf{L}_J is positive semi-definite with two zero-eigenvalues that correspond to the two rigid body modes (translation in the x-direction and the translation in the y-direction). These two modes are constant functions and can be represented exactly at any scale, i.e., the detail components associated with these modes are always zero. This means that the operator \mathbf{Q}_{J-1} is orthogonal to these rigid body modes. Let Θ denote the subspace spanned by the rigid body modes. From the positive-semi-definiteness of \mathbf{L}_J we know, that for all non-zero vectors \mathbf{x} in the space V^J that are orthogonal to the rigid body modes

$$\mathbf{x}^T \mathbf{L}_J \mathbf{x} > 0, \quad \mathbf{x} : \{\mathbf{x} \neq \mathbf{0}, \mathbf{x} \in V^J \setminus \Theta\} \quad (3.31)$$

Using the orthogonality of the wavelet transform operator, (3.31) can be written as

$$(\mathbf{W}\mathbf{x})^T (\mathbf{W}\mathbf{L}\mathbf{W}^T) (\mathbf{W}\mathbf{x}) > 0, \quad \mathbf{x} : \{\mathbf{x} \neq \mathbf{0}, \mathbf{x} \in V^J \setminus \Theta\} \quad (3.32)$$

Using equation (3.28) this can be expressed as

$$\begin{bmatrix} \mathbf{W}\mathbf{x} \end{bmatrix}^T \begin{bmatrix} \mathbf{L}_{J-1} & \mathbf{C}_{J-1} \\ \mathbf{C}_{J-1}^T & \mathbf{A}_{J-1} \end{bmatrix} \begin{bmatrix} \mathbf{W}\mathbf{x} \end{bmatrix} > 0, \quad \mathbf{x} : \{\mathbf{x} \neq \mathbf{0}, \mathbf{x} \in V^J \setminus \Theta\} \quad (3.33)$$

Also, any vector in Θ has no detail components, i.e.,

$$\forall \mathbf{x} \in \Theta, \mathcal{W}\mathbf{x} = \begin{bmatrix} \mathbf{x} \\ \mathbf{0} \end{bmatrix} \quad (3.34)$$

Consider $\mathbf{y} \in V^J$ such that $\mathcal{W}\mathbf{y} = \begin{bmatrix} \mathbf{0} \\ \mathbf{v} \end{bmatrix}$, where $\mathbf{v} \in W^{J-1}$. It can be seen from equation

(3.34) (and using the linearity of the concerned operators) that \mathbf{y} is orthogonal to any vector in the subspace Θ . Now, for all such vectors \mathbf{y} ,

$$\mathbf{y}^T \mathbf{L}_J \mathbf{y} > 0 \quad (3.35)$$

Using the same approach as in equation (3.33), we have

$$\begin{bmatrix} \mathbf{0} \\ \mathbf{v} \end{bmatrix}^T \begin{bmatrix} \mathbf{L}_{J-1} & \mathbf{C}_{J-1} \\ \mathbf{C}_{J-1}^T & \mathbf{A}_{J-1} \end{bmatrix} \begin{bmatrix} \mathbf{0} \\ \mathbf{v} \end{bmatrix} > 0, \forall \mathbf{v} \in W^{J-1} \quad (3.36)$$

After carrying out the multiplication we have

$$\mathbf{v}^T \mathbf{A}_{J-1} \mathbf{v} > 0, \forall \mathbf{v} \in W^{J-1} \quad (3.37)$$

Thus, from equation (3.37) we can see that the matrix \mathbf{A}_{J-1} is positive-definite and thus invertible. More generally, Engquist and Runborg [17] show that the operator \mathbf{A}_{J-1} is bijective for a class of elliptic operators \mathbf{L}_J obtained from bilinear forms.

The matrix

$$\mathbf{H}_{J-1} \doteq \mathbf{L}_{J-1} - \mathbf{C}_{J-1} \mathbf{A}_{J-1}^{-1} \mathbf{C}_{J-1}^T \quad (3.38)$$

is the effective stiffness matrix at level $J-1$ associated with a periodic patch of identical substructures Ω_c discretized at level J . Further reductions are possible by applying the reduction procedure recursively to obtain a sequence of effective stiffness matrices \mathbf{H}_{J-2} , \mathbf{H}_{J-3} , etc. It should be noted that the each reduction of the stiffness matrix

results in a matrix that is relatively much denser than the original matrix. This is illustrated in figure 3.2 where the dark regions denote non-zero entries.

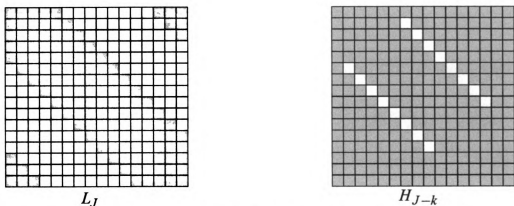


Figure 3.2: Structure of L_J and H_{J-k}

If the structure considered involves forces that are slow-varying in nature, i.e., $\tilde{\mathbf{f}} = \mathbf{0}$, then the above set of matrices $(L_J, \{H_{J-k}\})$ form a complete description of the substructure at various scales.

The obtained effective stiffness matrices operate on vectors that result from a wavelet discretization of the associated functions. This creates some difficulties not only in the application of boundary conditions but also in the assembly of stiffness matrices from several substructures. Moreover, the strain energy of an assembly of substructures is not the sum of strain energies of individual substructures since the associated basis functions in each substructure extend beyond the boundaries of the substructure. This is due to the fact that the support (=5) of the considered scaling functions (D6) is greater than 1. It might be advantageous to convert these wavelet effective stiffness matrices into equivalent nodal stiffness matrices that operate on the nodal values of the associated forces and displacements defined on the substructure (similar to a bi-linear finite-element

stiffness matrix). Also, these nodal-matrices would be more portable and can be incorporated into general-purpose widely available finite element codes. This conversion is described next.

3.4.2 Transformation to Finite-Element Form

This section deals with finding an approximation to \mathbf{H}_j that acts on finite-element instead of wavelet spaces. Introduce V^w and V^h as finite-dimensional spaces of periodic functions on Ω_c spanned respectively by D6 scaling functions (φ) and bi-linear finite element shape functions (φ^h) shown in figure 3.3.

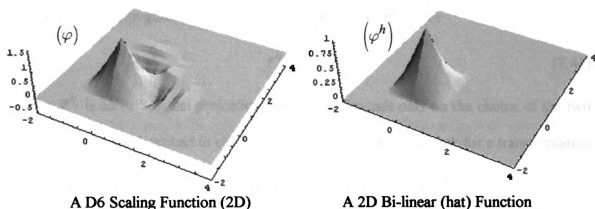


Figure 3.3: Basis functions in the wavelet and finite-element spaces respectively

Representative functions in these spaces are of the form

$$u_w = \sum_{k,l=0}^{n-1} u_{kl}^w \varphi_{kl} \quad \text{and} \quad u_h = \sum_{k,l=0}^{n-1} u_{kl}^h \varphi_{kl}^h \quad (3.39)$$

where $n = 2^j$. Here $\mathbf{u}^w = \{u_{kl}^w\}$ are wavelet coefficients and $\mathbf{u}^h = \{u_{kl}^h\}$ are displacements at nodes on an $n \times n$ uniformly spaced grid with spacing $\Delta = 2^{-j} L_c$.

Three approaches to convert a periodic stiffness matrix, \mathbf{H}_j , into an equivalent nodal stiffness matrix in the (bi-linear) finite-element space are presented.

3.4.2.1 Method I

For a given periodic stiffness matrix \mathbf{H} (corresponding to a periodically tiled domain) and a force f^w in V^w with mean value zero (i.e., orthogonal to the two rigid body modes) there exists a unique displacement $u^w \in V^w$ (and associated coefficients \mathbf{u}^w) such that

$$\mathbf{H}\mathbf{u}^w = \mathbf{f}^w \quad (3.40)$$

Let f^h be the orthogonal projection of f^w onto V^h computed as

$$\mathbf{f}^h = \mathbf{P}^h \mathbf{f}^w \quad (3.41)$$

where \mathbf{P}^h is an orthogonal projection matrix that depends only on the choice of the two basis functions (as described in chapter 2, section 2.7). We now look for a transformation matrix \mathbf{Q} that transforms the vector of wavelet displacement coefficients \mathbf{u}^w , into a vector of nodal displacements \mathbf{u}^h , in such a way that the work of the loads \mathbf{f}^w and \mathbf{f}^h is the same, i.e.,

$$\mathbf{u}^h = \mathbf{Q}\mathbf{u}^w \quad (3.42)$$

and

$$\mathbf{f}^{wT} \mathbf{u}^w = \mathbf{f}^{hT} \mathbf{u}^h \quad (3.43)$$

This is illustrated in figure 3.4.

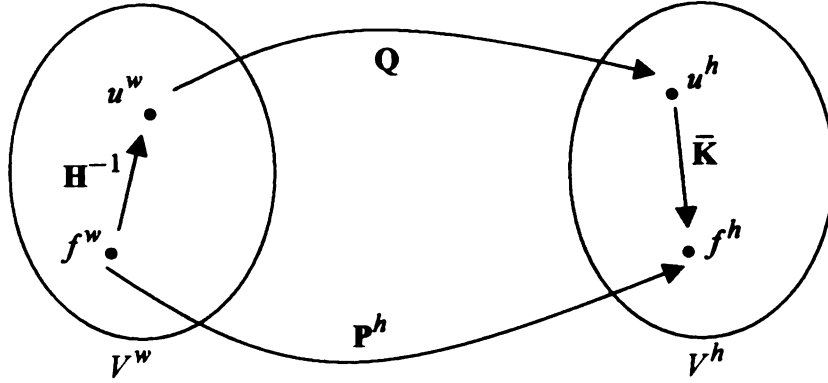


Figure 3.4: Conversion from wavelet to finite element spaces using method I

The work due to the force and displacement in V^h can be written as

$$\mathbf{f}^{hT} \mathbf{u}^h = \mathbf{f}^{wT} \mathbf{P}^{hT} \mathbf{Q} \mathbf{u}^w \quad (3.44)$$

Combining equations (3.43) and (3.44) we see that

$$\mathbf{Q} = [\mathbf{P}^{hT}]^{-1} \quad (3.45)$$

Now, we look for a matrix $\bar{\mathbf{K}}$ that relates the forces and displacements in V^h as

$$\bar{\mathbf{K}} \mathbf{u}^h = \mathbf{f}^h \quad (3.46)$$

Using equations (3.42) and (3.45) in (3.40), we have

$$\mathbf{H} \mathbf{u}^w = \mathbf{f}^w \Rightarrow \mathbf{H} \mathbf{P}^{hT} \mathbf{u}^h = [\mathbf{P}^h]^{-1} \mathbf{f}^h \Rightarrow \mathbf{P}^h \mathbf{H} \mathbf{P}^{hT} \mathbf{u}^h = \mathbf{f}^h \quad (3.47)$$

Thus the equivalent finite element matrix is

$$\bar{\mathbf{K}} = \mathbf{P}^h \mathbf{H} \mathbf{P}^{hT} \quad (3.48)$$

3.4.2.2 Method II

Here we start with a finite-element function (force) $f^h \in V^h$ and denote f^w to be its orthogonal projection onto V^w whose coefficients are computed as

$$\mathbf{f}^w = \mathbf{P}^w \mathbf{f}^h \quad (3.49)$$

where \mathbf{P}^w is an orthogonal projection matrix. The objective here is to find a transformation matrix $\mathbf{R} : V^h \rightarrow V^w$ that transforms a finite-element displacement into an equivalent wavelet displacement and in turn the associated nodal stiffness matrix such that the work of the loads \mathbf{f}^w and \mathbf{f}^h is the same, i.e.,

$$\mathbf{u}^w = \mathbf{R} \mathbf{u}^h \quad (3.50)$$

and

$$\mathbf{f}^{hT} \mathbf{u}^h = \mathbf{f}^{wT} \mathbf{u}^w \quad (3.51)$$

This process is illustrated in figure 3.5.

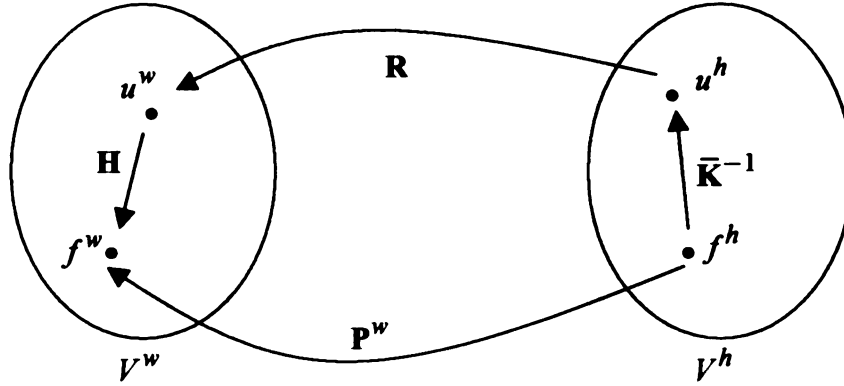


Figure 3.5: Conversion from wavelet to finite element spaces using method II

The work associated with $u^w, f^w \in V^w$ can be expressed as

$$\mathbf{f}^{wT} \mathbf{u}^w = \mathbf{f}^{hT} \mathbf{P}^{wT} \mathbf{R} \mathbf{u}^h \quad (3.52)$$

Combining equations (3.51) and (3.52) we see that the works are the same only if

$$\mathbf{R} = \left[\mathbf{P}^{wT} \right]^{-1} \quad (3.53)$$

As before, we look for a finite element stiffness matrix that relates \mathbf{u}^h and \mathbf{f}^h as

$$\bar{\mathbf{K}}\mathbf{u}^h = \mathbf{f}^h \quad (3.54)$$

Using equations (3.50) and (3.53) in (3.40), we have

$$\begin{aligned} \mathbf{H}\mathbf{u}^w = \mathbf{f}^w &\Rightarrow \mathbf{H}\left[\mathbf{P}^{wT}\right]^{-1}\mathbf{u}^h = \mathbf{P}^w\mathbf{f}^h \\ &\Rightarrow \left[\mathbf{P}^w\right]^{-1}\mathbf{H}\left[\mathbf{P}^{wT}\right]^{-1}\mathbf{u}^h = \mathbf{f}^h \end{aligned} \quad (3.55)$$

The equivalent nodal stiffness matrix is then

$$\bar{\mathbf{K}} = \left[\mathbf{P}^w\right]^{-1}\mathbf{H}\left[\mathbf{P}^{wT}\right]^{-1} \quad (3.56)$$

3.4.2.3 Method III

Here we introduce a matrix \mathbf{B} , defined such that

$$\mathbf{u}^{wT}\mathbf{B}\mathbf{u}^h = \int_{\Omega_c} \bar{E}(y) \varepsilon(\mathbf{u}^w) \varepsilon(\mathbf{u}^h) dy \quad (3.57)$$

The right hand side of equation (3.57) is the elasticity bilinear form with finite-element (hat) trial functions and wavelet weight functions (compare to 3.22). The elastic tensor \bar{E} is an average of the material in the substructure and is assumed to be of the form

$$\bar{E} = \rho_B(y)E^0 \quad (3.58)$$

where E^0 is a reference elasticity tensor and ρ_B is a distribution of relative densities that is obtained by averaging the fine-scale distribution of relative densities to the coarse-scale using (3.18) (It should be noted that this is the only place where an average of the material is used in this method that is based on a multi-resolution analysis of displacements). The matrix \mathbf{B} is one that transforms a finite-element displacement $\mathbf{u}^h \in V^h$ into a wavelet body force $\mathbf{f}^w \in V^w$, i.e., $\mathbf{f}^w = \mathbf{B}\mathbf{u}^h$ is the wavelet body force

th

tr

(v

tra

su

wc

and

Thi

The w

that corresponds to a finite-element pre-strain $\varepsilon(\mathbf{u}^h)$. If the basis functions used as the trial and weight functions are interchanged, matrix \mathbf{B}^T is the one that transforms a given (wavelet) displacement $\mathbf{u}^w \in V^w$ into a finite-element body force $\mathbf{f}^h \in V^h$.

Having defined this operator \mathbf{B} , we look for an operator $\mathbf{Q}: V^w \rightarrow V^h$ that transforms a given wavelet displacement $\mathbf{u}^w \in V^w$ into a nodal displacement $\mathbf{u}^h \in V^h$ such that the work due to the transformed forces and displacements is the same as the work of the corresponding functions in V^w , i.e.,

$$\mathbf{u}^h = \mathbf{Q}\mathbf{u}^w \quad (3.59)$$

and

$$\mathbf{f}^{hT} \mathbf{u}^h = \mathbf{f}^{wT} \mathbf{u}^w \quad (3.60)$$

This process is illustrated in figure 3.6.

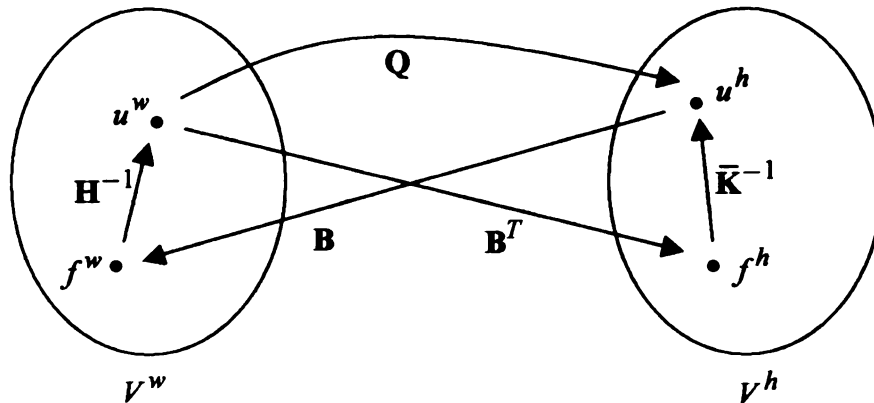


Figure 3.6: Conversion from wavelet to finite-element spaces using method III

The work corresponding to the displacements and forces in V^h can be written as

$$\mathbf{f}^{hT} \mathbf{u}^h = \mathbf{u}^{wT} \mathbf{BQ}\mathbf{u}^w = \mathbf{f}^{wT} \mathbf{H}^{-1} \mathbf{BQ}\mathbf{u}^w \quad (3.61)$$

From eq

Using eq

Thus, the

TH
equivalen
substructu

3.4.3 Co

In this se
matrix of

1. As

L

wh

su

(di

ρ_e

From equations (3.60) and (3.61) we see that

$$\mathbf{Q} = \mathbf{B}^{-1}\mathbf{H}_j \quad (3.62)$$

Using equation (3.62) in the equation $\bar{\mathbf{K}}\mathbf{u}^h = \mathbf{f}^h$ we have,

$$\bar{\mathbf{K}}\mathbf{u}^h = \mathbf{f}^h \Leftrightarrow \bar{\mathbf{K}}\mathbf{Q}\mathbf{u}^w = \mathbf{B}^T\mathbf{u}^w \Leftrightarrow \bar{\mathbf{K}}\mathbf{B}^{-1}\mathbf{H}\mathbf{u}^w = \mathbf{B}^T\mathbf{u}^w \quad (3.63)$$

Thus, the equivalent nodal stiffness matrix is then given as

$$\bar{\mathbf{K}} = \mathbf{B}^T\mathbf{H}^{-1}\mathbf{B} \quad (3.64)$$

The matrix $\bar{\mathbf{K}}$ obtained using either of these approaches is the “finite element equivalent” to \mathbf{H}_j . It relates nodal degrees of freedom to nodal forces in a periodic substructure reduced from level J to level j .

3.4.3 Computational Aspects

In this section, the computational procedure involved in obtaining a reduced stiffness matrix of a substructure using the multi-resolution analysis of displacements is outlined.

1. Assemble a fine-scale wavelet stiffness matrix of a substructure, \mathbf{L}_J , as

$$\mathbf{L}_J = \sum_{e=1}^{N_J} \rho_e^J \mathbf{I}^0 \quad (\text{sum interpreted in the sense of assembly})$$

where $N_J = 2^J \times 2^J$ is the number of pixels in the fine-scale discretization of the substructure, \mathbf{I}^0 is a pre-computed wavelet “element” stiffness matrix of a pixel (dimension 50×50 for D6 scaling function) with a reference material tensor and ρ_e^J is the value of the relative density function at a pixel e .

S

For j =

2. C

3. C

at

Th

ha

ma

end loop

4. AS

de

an

usi

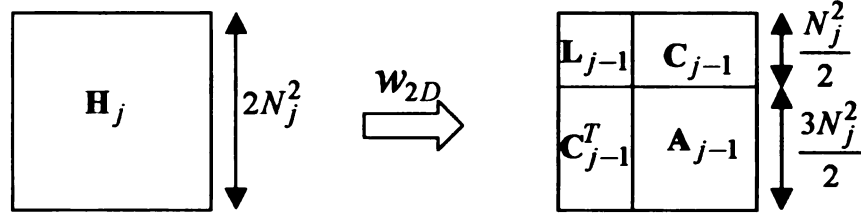
va

5. Co

Set $\mathbf{H}_J = \mathbf{L}_J$.

For $j = J$ to $J - k + 1$ (k is the number of reduction levels), do

2. Compute the wavelet decomposition of the stiffness matrix at level j



3. Compute the Schur's complement to obtain the effective reduced stiffness matrix at level $j - 1$

$$\mathbf{H}_{j-1} = \mathbf{L}_{j-1} - \mathbf{C}_{j-1} \mathbf{A}_{j-1}^{-1} \mathbf{C}_{j-1}^T$$

This involves the solution of a $\frac{3N_j^2}{2} \times \frac{3N_j^2}{2}$ system of equations with $\frac{N_j^2}{2}$ right

hand sides and the multiplication of a $\frac{N_j^2}{2} \times \frac{3N_j^2}{2}$ matrix with a $\frac{3N_j^2}{2} \times \frac{N_j^2}{2}$

matrix.

end loop

4. Assemble $\mathbf{B} = \sum_{e=1}^n \rho_B^e \mathbf{b}^0$, where $n = 2^{J-k} \times 2^{J-k}$, ρ_B is an *averaged* relative

density distribution at the reduced scale (obtained as shown in equation (3.18))

and \mathbf{b}^0 is a pre-computed “element” matrix of size 50×8 that is constructed using D6 and Hat functions as the weight and trial functions respectively in the variational form of the elasticity equation.

5. Compute $\bar{\mathbf{K}} = \mathbf{B}^T \mathbf{H}_{J-k}^{-1} \mathbf{B}$

End.

The mo

This inv

as matrix

stiffness

computat

finest-sca

reference

steps 4 ar

are much

fine-scale

relatively

The matrix \mathbf{H}_{J-k} is positive semi-definite (it has two rigid body modes). It is inverted by adding a matrix $\epsilon\mathbf{Q}$ to remove the rigid body modes. Here, ϵ is a suitable scalar penalty and $\mathbf{Q} = \mathbf{p}^T \mathbf{p}$, where $\mathbf{p} = \begin{bmatrix} 1 & \cdots & 1 & 0 & \cdots & 0 \\ 0 & \cdots & 0 & 1 & \cdots & 1 \end{bmatrix}$ is a matrix of rigid body modes.

End.

The most computationally intensive step is computing the Schur's complement (step 3). This involves the solution of a system of equations for multiple right hand sides as well as matrix multiplication. At the end of each reduction stage (steps 2 and 3) the size of the stiffness matrix (and hence the number of equations) reduces by a factor of 4 and thus the computations progressively reduce after each reduction step. The first step, involving the finest-scale stiffness matrix, can be implemented efficiently with a pre-computed reference "element" stiffness matrix and using sparse assembly. The computations in steps 4 and 5 are performed on matrices in the reduced-scale; the sizes of these matrices are much smaller (factor of 2^{2k} , where k is the number of reductions) compared to the fine-scale stiffness matrix. It should be noted that the reduced stiffness matrices are relatively much denser than the fine-scale matrices, as illustrated in Figure 3.2.

3.5 C

In this
respect

3.5.1

displa

Conside

to an N

the spa

$n \times n$, v

matrix

$\mathbf{KE} = s$

diagona

bases f

eigenv

The tw

translat

\mathbf{K} othe

3.5 Comparison of the Model Reduction Schemes

In this section, comparisons of the proposed model reduction schemes are presented with respect to each other and with the classical homogenization scheme.

3.5.1 Comparison between MRA of material distribution and MRA of displacements

Consider $\mathbf{K}:V \rightarrow V$ and $\hat{\mathbf{K}}:V \rightarrow V$ to be the reduced stiffness matrices that correspond to an MRA of material distribution and an MRA of displacements, respectively, and V is the space of kinematically admissible functions. Let the dimensions of the matrices be $n \times n$, where n is the number of degrees of freedom in the models. Define \mathbf{E} to be a matrix of eigenvectors and $\mathbf{\Omega}$ to be a diagonal matrix of eigenvalues of \mathbf{K} , i.e., $\mathbf{K}\mathbf{E} = \mathbf{\Omega}\mathbf{E}$. Similarly, define $\hat{\mathbf{E}}$ to be the matrix of eigenvectors and $\hat{\mathbf{\Omega}}$ to be the diagonal matrix of eigenvalues of $\hat{\mathbf{K}}$, i.e., $\hat{\mathbf{K}}\hat{\mathbf{E}} = \hat{\mathbf{\Omega}}\hat{\mathbf{E}}$. Since \mathbf{E} and $\hat{\mathbf{E}}$ are orthonormal bases for V , any eigenvector \mathbf{e}_i of \mathbf{K} can be expressed as a linear combination of eigenvectors ($\hat{\mathbf{e}}_j$) of $\hat{\mathbf{K}}$, i.e.,

$$\mathbf{e}_i = \sum_j \beta_{ij} \hat{\mathbf{e}}_j, \quad \beta_{ij} = \langle \mathbf{e}_i, \hat{\mathbf{e}}_j \rangle \quad (3.65)$$

The two stiffness matrices have two zero-energy (rigid body) modes that correspond to a translation in the x and y directions respectively. Let $\bar{\mathbf{E}}$ be the matrix of eigenvectors of \mathbf{K} other than the rigid body modes, $\dim(\bar{\mathbf{E}}) = n \times n - 2$. This can be expressed as

$$\bar{\mathbf{E}} = \hat{\mathbf{E}}\mathbf{B} \quad (3.66)$$

w

a

A

f

a

w

c

w

c

T

as

It

nu

where the entries in matrix \mathbf{B} are of the form

$$B_{ij} = \langle \bar{e}_i, \hat{e}_j \rangle \quad (3.67)$$

and \bar{e}_i and \hat{e}_i are column vectors of $\bar{\mathbf{E}}$ and $\hat{\mathbf{E}}$ respectively.

Any (displacement) vector \mathbf{u} that is orthogonal to the rigid body modes can be written as,

$$\mathbf{u} = \bar{\mathbf{E}}\boldsymbol{\alpha} \quad (3.68)$$

for some $\alpha_i \in \mathbb{R}$. Using the orthogonality of $\bar{\mathbf{E}}$, we can write the strain energy associated with this displacement \mathbf{u} using the material MRA model as

$$\mathbf{u}^T \mathbf{K} \mathbf{u} = \boldsymbol{\alpha}^T \bar{\mathbf{E}}^T \mathbf{K} \bar{\mathbf{E}} \boldsymbol{\alpha} = \boldsymbol{\alpha}^T \bar{\boldsymbol{\Omega}} \boldsymbol{\alpha} \quad (3.69)$$

where $\bar{\boldsymbol{\Omega}}$ is a diagonal matrix of the non-zero eigenvalues of \mathbf{K} . The displacement \mathbf{u} can be expressed in terms of the eigenvectors of $\hat{\mathbf{K}}$ as

$$\mathbf{u} = \hat{\mathbf{E}} \mathbf{B} \boldsymbol{\alpha} \quad (3.70)$$

where the entries of \mathbf{B} are as defined in (3.67). Now, the strain energy associated with \mathbf{u} computed using the MRA of displacements can be expressed as

$$\mathbf{u}^T \hat{\mathbf{K}} \mathbf{u} = \boldsymbol{\alpha}^T \mathbf{B}^T \hat{\mathbf{E}}^T \hat{\mathbf{K}} \hat{\mathbf{E}} \mathbf{B} \boldsymbol{\alpha} = \boldsymbol{\alpha}^T \mathbf{B}^T \hat{\boldsymbol{\Omega}} \mathbf{B} \boldsymbol{\alpha} \quad (3.71)$$

The relative error in strain energy obtained using the two models can then be expressed as

$$\frac{|\mathbf{u}^T \mathbf{K} \mathbf{u} - \mathbf{u}^T \hat{\mathbf{K}} \mathbf{u}|}{|\mathbf{u}^T \mathbf{K} \mathbf{u}|} = \frac{|\boldsymbol{\alpha}^T [\bar{\boldsymbol{\Omega}} - \mathbf{B}^T \hat{\boldsymbol{\Omega}} \mathbf{B}] \boldsymbol{\alpha}|}{|\boldsymbol{\alpha}^T \bar{\boldsymbol{\Omega}} \boldsymbol{\alpha}|} \quad (3.72)$$

It can be shown using Rayleigh's principle that the eigenvalues of the matrix in the numerator of the right hand side of equation (3.72) form an upper bound on the relative

error of
rigid bo

Here, th
five diffe

Figure 3
obtained

$$|\Lambda_i| = e^{i\alpha}(\Delta)$$

Fi
en

error of the strain energies, i.e., for a normalized displacement \mathbf{u} that is orthogonal to rigid body modes,

$$\max_{\substack{|\mathbf{u}| \leq 1 \\ \mathbf{u} \neq \mathbf{0}}} \frac{|\mathbf{u}^T \mathbf{K} \mathbf{u} - \mathbf{u}^T \hat{\mathbf{K}} \mathbf{u}|}{|\mathbf{u}^T \mathbf{K} \mathbf{u}|} \leq \max \text{eig}(\mathbf{I} - \bar{\mathbf{\Omega}}^{-1} \mathbf{B}^T \hat{\mathbf{\Omega}} \mathbf{B}) \quad (3.73)$$

Here, the reduced stiffness matrices of a periodic tiling of a substructure for a choice of five different material distributions (Figure 3.7) are computed and compared.

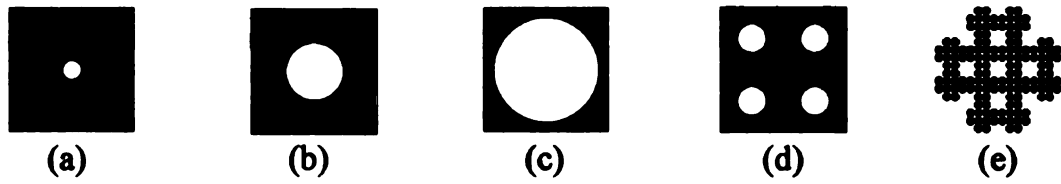


Figure 3.7: Choices of material distributions for the comparison

Figure 3.8 shows the plots of the eigenvalues of the matrix $(\Delta = \mathbf{I} - \bar{\mathbf{\Omega}}^{-1} \mathbf{B}^T \hat{\mathbf{\Omega}} \mathbf{B})$ obtained for the various choices of the material distributions chosen.

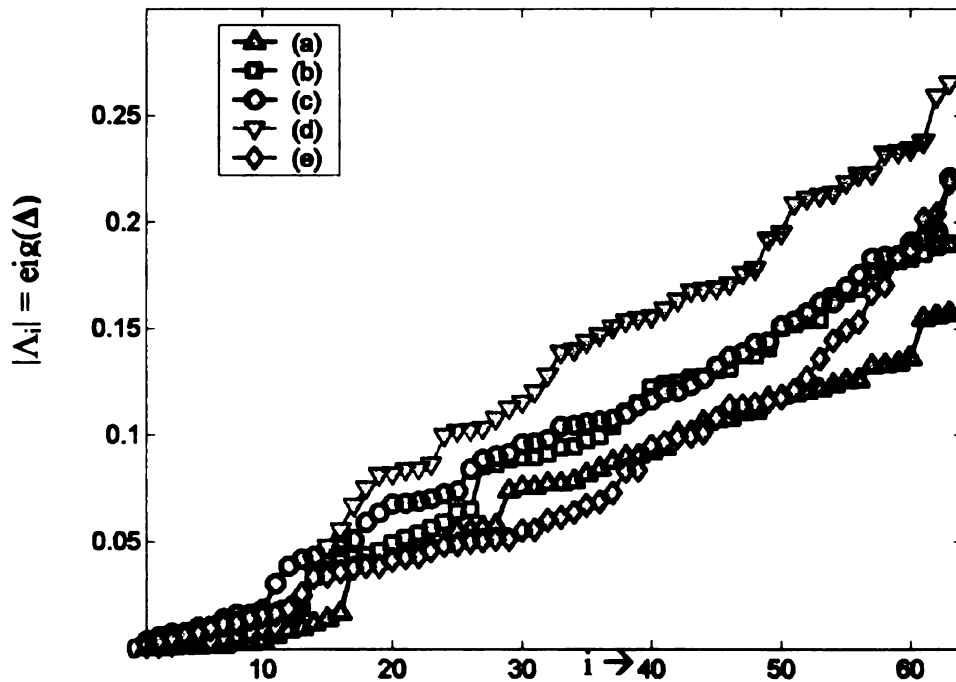


Figure 3.8: Bounds on the maximum relative error between the strain energy computed using material MRA and displacement MRA

The re
spacing
are 12
usually
spatial
error in
combin
on the

3.5.2

Homom

Here,
displace

infinites
is assum
base cell

where

represent
coordinat
given as

The reduced stiffness matrices are at a discretization that corresponds to a uniform spacing of degrees of freedom in a 8×8 grid. The dimensions of these stiffness matrices are 128×128 . The figure 3.8 shows the first 64 eigenvalues of the matrix Δ , as we are usually not concerned with the higher energy modes that correspond to rapidly varying spatial displacements. The value of the plots at each 'i' corresponds to a bound on the error in the strain energy associated with a displacement that can be expressed as a linear combination of the first 'i' modes. It can be seen that for the first few modes, the bound on the error is small but it increases as more number of modes are included.

3.5.2 Comparison between MRA techniques and Classical Homogenization

Here, the averaging schemes based on the MRA of material distributions and displacements are compared to the classical homogenization method.

In classical homogenization, the material distribution is assumed to vary at infinitesimal scales and an asymptotic analysis is used to compute effective properties. It is assumed that the material distribution is characterized by the periodic repetition of a base cell (Y). The displacement field u is expanded in an asymptotic series

$$u = u_0(x, y) + \varepsilon u_1(x, y) + \varepsilon^2 u_2(x, y) + \dots \quad (3.74)$$

where

$$y = x / \varepsilon \quad (3.75)$$

represents the local (microscopic) coordinates and x is the global (macroscopic) coordinate. It can be shown (see Bensoussan et al [5]) that the effective material tensor is given as

where χ

periodic

The strain

where E

ε^0 . Thus

correspon

Si

a periodic

Equation

$$E_{ijkl}^H = \frac{1}{Y} \int_Y \left(E_{ijkl} - E_{ijpq} \frac{\partial \chi_p^{kl}}{\partial y_q} \right) dY \quad (3.76)$$

where χ_p^{kl} is the solution to the so-called *cell-problem* defined on the infinitesimal periodic characteristic cell, given as follows

$$\int_Y E_{ijpq} \frac{\partial \chi_p^{kl}}{\partial y_q} \frac{\partial v_i}{\partial y_j} dY = \int_Y E_{ijkl} \frac{\partial v_i}{\partial y_j} dY, \quad \forall v \in V \quad (3.77)$$

$$V = \{v : v \text{ is } Y\text{-periodic}\}$$

The strain energy form of (3.76) can be written as

$$E_{ijpq}^H \varepsilon_{ij}^0 \varepsilon_{pq}^0 = \frac{1}{Y} \int_Y \left(E_{ijpq} \left(\varepsilon_{ij}^0 - \varepsilon_{ij}^* \right) \left(\varepsilon_{pq}^0 - \varepsilon_{pq}^* \right) \right) dY \quad (3.78)$$

where E is the material tensor and ε^* is the resultant strain due to the applied pre-strain, ε^0 . Thus, we can define the strain energy associated with a (finite size) substructure Ω_c , corresponding to a periodic repetition of infinitesimal cells Y , as

$$\Phi^H \triangleq \left[\frac{1}{Y} \int_Y \left(E_{ijpq} \left(\varepsilon_{ij}^0 - \varepsilon_{ij}^* \right) \left(\varepsilon_{pq}^0 - \varepsilon_{pq}^* \right) \right) dY \right] \times \text{meas}(\Omega_c) \quad (3.79)$$

Similarly, the strain energy associated with applying a constant pre-strain (ε^0) on a periodic tiling of a (finite-size) substructure Ω_c can be defined as

$$\Phi \triangleq \int_{\Omega_c} \left(E_{ijpq} \left(\varepsilon_{ij}^0 - \varepsilon_{ij}^* \right) \left(\varepsilon_{pq}^0 - \varepsilon_{pq}^* \right) \right) d\Omega \quad (3.80)$$

Equation (3.80) can then be written as

$$\Phi = \int_{\Omega_c} E_{ijpq} \varepsilon_{ij}^0 \varepsilon_{pq}^0 + \int_{\Omega_c} E_{ijpq} \varepsilon_{ij}^* \varepsilon_{pq}^* - 2 \int_{\Omega_c} E_{ijpq} \varepsilon_{ij}^0 \varepsilon_{pq}^* \quad (3.81)$$

The elas

substruc

Using (3

The first

strain and

prescribed

second

displacem

The strain

where \mathbf{K}

being that

The strain

where $\bar{\mathbf{K}}$

scale solu

The elasticity problem associated with the application of a constant pre-strain on a substructure Ω_c , is defined as: Find \mathbf{u}^* , such that

$$\int_{\Omega_c} E_{ijpq} \varepsilon_{ij}(\mathbf{u}^*) \varepsilon_{pq}(\mathbf{u}^*) = \int_{\Omega_c} E_{ijpq} \varepsilon_{ij}^0 \varepsilon_{pq}(\mathbf{u}^*) \quad (3.82)$$

Using (3.82) in (3.81), the strain energy becomes

$$\Phi = \int_{\Omega_c} E_{ijpq} \varepsilon_{ij}^0 \varepsilon_{pq}^0 - \int_{\Omega_c} E_{ijpq} \varepsilon_{ij}^* \varepsilon_{pq}^* \quad (3.83)$$

The first term on the right hand side of equation (3.83) does not involve the resultant strain and can be computed exactly without solving any elasticity problem (as ε^0 is a prescribed constant strain). The model reduction schemes are used to compute the second term using an approximation of either the material distribution or the displacements at a coarse scale, i.e., MRA of material or MRA of displacements.

The strain energy using a multi-resolution analysis of material is then

$$\Phi^M = \int_{\Omega_c} E_{ijpq} \varepsilon_{ij}^0 \varepsilon_{pq}^0 - \mathbf{u}^{*T} \mathbf{K}^c \mathbf{u}^* \quad (3.84)$$

where \mathbf{K}^c is a reduced stiffness matrix obtained as shown in (3.19), the only difference being that the substructure involved is assumed to be periodic.

The strain energy using a multi-resolution analysis of displacements is

$$\Phi^D = \int_{\Omega_c} E_{ijpq} \varepsilon_{ij}^0 \varepsilon_{pq}^0 - \mathbf{u}^{*T} \bar{\mathbf{K}} \mathbf{u}^* \quad (3.85)$$

where $\bar{\mathbf{K}}$ is a reduced stiffness matrix obtained as shown in (3.64) and \mathbf{u}^* is the coarse-scale solution to a constant pre-strain elasticity problem (It should be noted that the body

force (n)

material

T

homogen

various r

these mo

to a pres

a particu

would be

material

material

directions

strains ϵ^0

Here, sub

and the

$$\epsilon^0 = \begin{Bmatrix} 1 \\ 0 \end{Bmatrix}$$

Fi

computed

force (right hand side of 3.82) in this case is computed using an equivalent, reduced material tensor).

The comparison between the multi-resolution reduction schemes and classical homogenization is carried out by applying constant pre-strains to substructures with various material distributions and comparing the resulting strain energies when either of these models is used to compute the strain energy. The stiffer material, when subjected to a prescribed constant pre-strain will result in higher strain energy. In order to say that a particular material is stiffer, this result has to hold for all possible strains. However, it would be meaningful only to consider strains whose principal directions coincide with the material axes, as only then would the strain energy be maximum, i.e., the best use of the material is only when it is oriented in such a way that it coincides with the principal directions of the applied strain (see Pedersen [31]). Thus, among all such (normalized)

strains $\varepsilon^0 = \begin{bmatrix} 1 & \beta \\ \beta & \eta \end{bmatrix}$, the strain energy produced by the strain with $\beta = 0$ is the highest.

Here, substructures of unit sizes are considered with five choices of material distributions and the strain energies as a result of applying constant pre-strains of the form

$\varepsilon^0 = \begin{bmatrix} 1 & 0 \\ 0 & \eta \end{bmatrix}$, where $\eta \in [-1, 1]$, are computed.

Figures 3.9 (a) to (e) show the plots of strain energy (Φ) versus the parameter η , computed using the various methods discussed here.

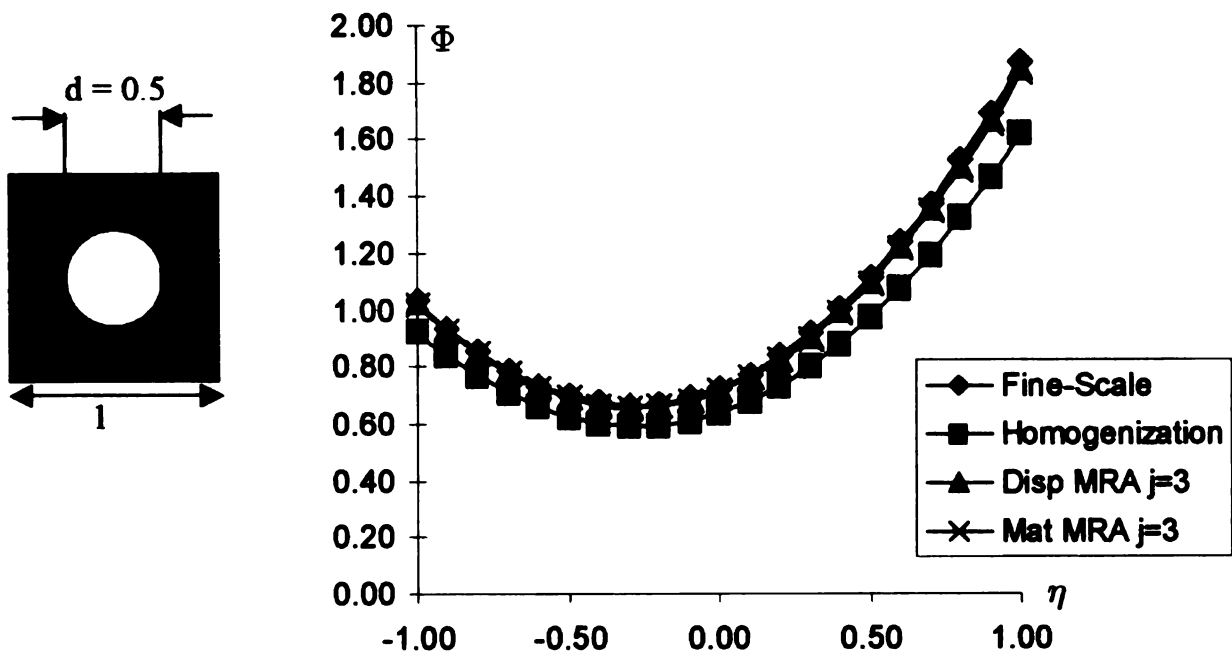


Figure 3.9(a): Strain energy comparisons for material distribution (a)

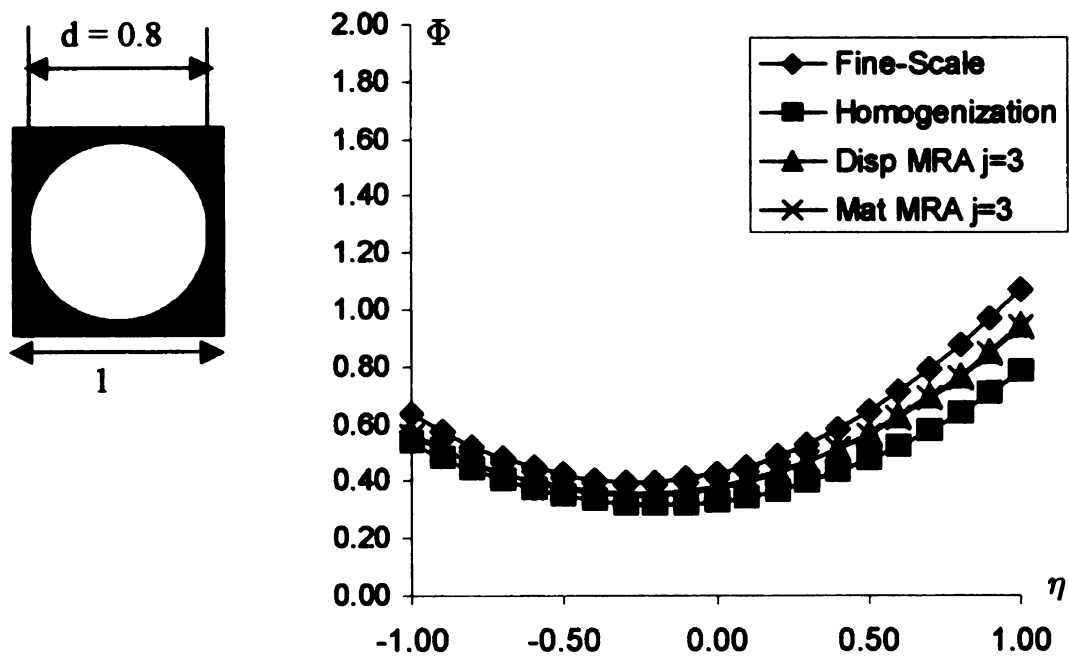


Figure 3.9(b): Strain energy comparisons for material distribution (b)

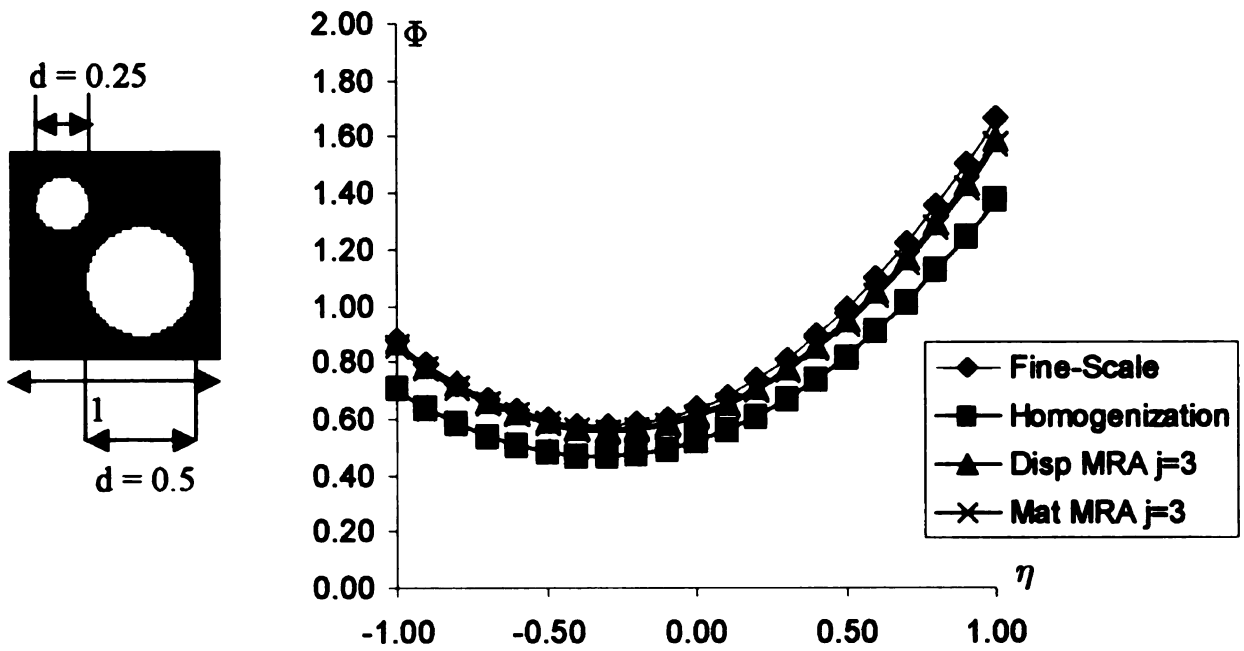


Figure 3.9(c): Strain energy comparisons for material distribution (c)

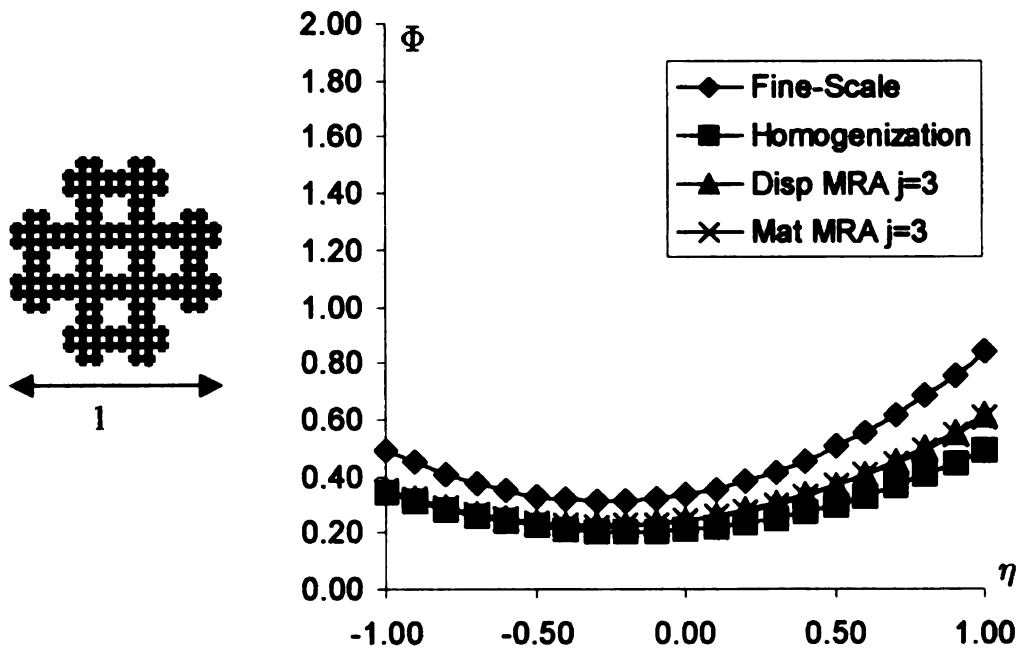


Figure 3.9(d): Strain energy comparisons for material distribution (d)

In the ab
discretiz
structure
energy i
scale mo
used. F
properti
classical
underest
complica
loss of a
essential
matrices
the effec

3.6 C

Matrix

The red
not yet
build a n
be expr
 $\Omega = U_c$

In the above plots, the reduction process involved starting from a 64×64 ($J=6$) element discretization and reducing it to a 8×8 ($j=3$) discretization. For simple material structures such as the perforated substructures in Figure 3.9 (a), (b) and (c), the strain energy in the reduced model is essentially indistinguishable from the energy in the full-scale model, regardless of whether the material based or displacement based MRA is used. For comparison, the graphs also show the energy in a substructure whose elastic properties are those of a periodic mixture at infinitesimal scales, i.e., the result from classical homogenization methods. In all cases, using such effective properties will underestimate the strain energy (and hence the stiffness) of the substructures. For more complicated structures, such as in Figure 3.9 (d), the loss of resolution results in some loss of accuracy. However, even in this case the two reduction processes result in essentially identical approximations of the strain energy and the reduced stiffness matrices still provide a more accurate of the strain energy in the full-scale structure than the effective properties obtained from classical homogenization.

3.6 Computing the Non-Periodic Reduced Stiffness Matrix of a Substructure

The reduced matrix $\bar{\mathbf{K}}$, obtained using a multi-resolution analysis of the displacements is not yet ready to be used as a super-element and assembled with other such matrices to build a model of a complex structure. This is because, while the area of the structure can be expressed a union of smaller areas that correspond to smaller substructures, $\Omega = \bigcup_c \Omega_c$, the total stiffness matrix of the structure cannot be expressed as an assembly

of *peri*

interpre

that cha

For this

different

technique

a single

surround

substruct

layout is

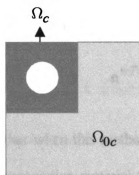
3.10.

Fig

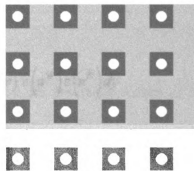
of *periodic* stiffness matrices of individual substructures, $\mathbf{K}(\Omega) \approx \sum_c \bar{\mathbf{K}}^c(\Omega_c)$ (sum

interpreted in the sense of assembly). However, $\bar{\mathbf{K}}$ can be used to construct a matrix \mathbf{K} that characterizes a substructure as a single entity in a non-periodic arrangement.

For this we turn to the well-known computational scheme used in the solution of partial differential equations on arbitrarily shaped domains called the *fictitious domain technique*, (e.g., see Bakhvalov and Knyazev [1], Glowinski et al [21]). The properties of a single substructure that is not part of a periodic arrangement can be obtained by surrounding the substructure by weak material of a sufficiently low strength so that the substructure is essentially unaffected by its surroundings. A periodic arrangement of this layout is characterized by a fictitious substructure $\Omega_{Fc} = \Omega_c \cup \Omega_{0c}$ as shown in figure 3.10.



Fictitious Substructure Ω_{Fc}



Periodic arrangement of fictitious substructures

Figure 3.10. Substructure surrounded by a weak fictitious domain

For exam

fine-scal

the fictit

Thus, th

substruct

to level

substruct

Using th

where B

Recall th

the corre

over the

substruct

$j+1$ is d

[§] See sec

For example, if the material distribution within Ω_c is resolved by $2^J \times 2^J$ pixels[§], the fine-scale problem in Ω_{Fc} involves $2^{J+1} \times 2^{J+1}$ pixels and the material distribution in the fictitious substructure is defined as follows

$$\rho(\Omega_{ij}^{Fc}) = \begin{cases} \rho(\Omega_c) & i, j \in \Omega_c \\ \varepsilon \ll 1 & i, j \in \Omega_{0c} \end{cases} \quad (3.86)$$

Thus, the fine-scale problem on a substructure is now extended to one on the fictitious substructure and the reduction procedure discussed earlier is performed from level $J+1$ to level $j+1$ to compute a reduced stiffness matrix corresponding to this fictitious substructure, denoted as \mathbf{H}_{j+1}^F .

Using the approach in section 3.5.2.3, we compute the nodal matrix as

$$\bar{\mathbf{K}}_{j+1}^F = \mathbf{B}_{j+1}^F \left[\mathbf{H}_{j+1}^F \right]^{-1} \mathbf{B}_{j+1}^F \quad (3.87)$$

where \mathbf{B}_{j+1}^F is defined as

$$\mathbf{u}^{wT} \mathbf{B}_{j+1}^F \mathbf{u}^h = \int_{\Omega_c} \bar{E}_{j+1}^F(\mathbf{y}) \varepsilon(\mathbf{u}^w) \varepsilon(\mathbf{u}^h) d\mathbf{y} \quad (3.88)$$

Recall that when this method was illustrated with periodic stiffness matrices and vectors, the corresponding material tensor used in the definition of the matrix \mathbf{B} was the average over the substructure (as given in (3.58)). In the case of a fictitious substructure (i.e., substructure surrounded by a weak fictitious material) the average material tensor at scale $j+1$ is defined as

[§] See section 3.2

This is d
original
resulting
The pres
analysis
the actual
both the
of the fu
is define
state of d

where α

domain a

$\alpha_{jB}^c(y)$

The par

in figur

$$\bar{E}_{j+1}^F(y) = \begin{cases} \rho_{jB}^c(y) E^0 & \text{if } y \in \Omega_c \\ 0 & \text{if } y \in \Omega_{0c} \end{cases} \quad (3.89)$$

This is done so that the terms corresponding to the non-periodic stiffness matrix of the original substructure (without the fictitious domain) are the only non-zero terms in the resulting matrix obtained using (3.87) and thus can be directly obtained.

The presence of the fictitious domain in the reduction process using the multi-resolution analysis of displacements causes the terms that are associated with the boundary between the actual substructure and the weak fictitious domain to have properties that are due to both these materials. These *edge effects* need to be compensated using a judicious choice of the function ρ_{jB}^c , which is the only adjustable parameter in this process. Here $\rho_{jB}^c(y)$ is defined such that a patch of 3×3 isotropic, homogeneous substructures reproduces a state of constant strain exactly. We assume that $\rho_{jB}^c(y)$ is of the form

$$\rho_{jB}^c(y) = \alpha_{jB}^c(y) \rho_j^c(y) \quad (3.90)$$

where $\alpha_{jB}^c(y)$ is a correction factor to compensate for the presence of the fictitious domain and $\rho_j^c(y) \equiv 1$ for a homogeneous substructure. The piecewise constant function

$\alpha_{jB}^c(y)$ is of the form

$$\alpha_{jB}^c(y) = \sum_{k,l=0}^n \alpha_{kl} \varphi_{j,kl}^H(y) \quad (3.91)$$

The patch is subjected to three prescribed constant strain fields $\varepsilon_0^I, \varepsilon_0^{II}, \varepsilon_0^{III}$ as illustrated in figure 3.11.

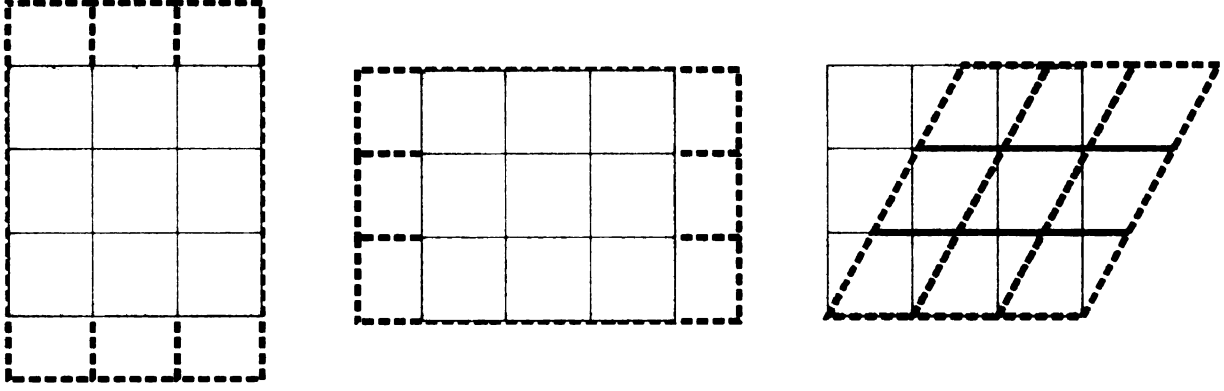


Figure 3.11. Constant pre-strains applied to a patch of substructures

The coefficients α_{kl} are chosen to minimize the function

$$\Phi = \|\epsilon^I - \epsilon_0^I\|^2 + \|\epsilon^{II} - \epsilon_0^{II}\|^2 + \|\epsilon^{III} - \epsilon_0^{III}\|^2 \quad (3.92)$$

where ϵ^I , ϵ^{II} and ϵ^{III} are the strains resulting from the imposed pre-strains.

$\bar{\mathbf{K}}_{j+1}^{Fc}$ is a matrix of size $2(4n^2 \times 4n^2)$ for $n = 2^j$, from this we extract a sub-matrix \mathbf{K}_j^c of dimensions $2((n+1)^2 \times (n+1)^2)$, in the case of approach III, these are the only non-zero terms in $\bar{\mathbf{K}}_{j+1}^{Fc}$. This matrix characterizes the behavior of a substructure Ω_c as a single entity in a non-periodic setting when reduced from level J to level $j < J$. This can now be used as a building block in an assembly of other substructures to construct a complete reduced model of a structure.

3.7 Computing Fine-Scale Stresses By Augmentation

The solution to the reduced system of equations obtained using either of the earlier described methods represents the coarse behavior of the original system. This is useful and may even be sufficient for certain design problems that involve only large-scale

behavior. However, it may be necessary to compute some small-scale effects at certain locations (substructures) of interest, such as local stresses at locations of possible stress-concentrations such as sharp corners or abrupt changes in geometry or material properties. In this section, a method to compute the small-scale stresses (where necessary) given the coarse solution is presented.

This problem can be compared to that of computing the small-scale stresses in classical periodic homogenization. In the case of classical homogenization, the large-scale (coarse) solution is used to compute a coarse-scale strain field. Since this method assumes that the small-scale is microscopic, the coarse-scale strain field at any point in the domain may be thought of as a constant strain over the (infinitesimal) region occupied by the microstructure. The small-scale displacements in the case of classical homogenization are computed as the solution to the cell problem (3.77) for a constant pre-strain, where the value of constant pre-strain is the value of the large-scale strain at a location of interest. The important difference in the present scheme is that the small-scale problem is solved on a domain of finite size rather than on an infinitesimal cell. Thus the small-scale displacements cannot be computed simply by applying a *constant* pre-strain over the substructure, as in classical homogenization. The large-scale strains in the substructure are in general not constant. In the case of the model reduction using a multi-resolution analysis of the displacements, it is possible to obtain the fine-scale displacements at any substructure using a consistent augmentation procedure. This is not possible in the case of the multi-resolution analysis of the material.

Let c be a particular substructure of interest whose small-scale stresses need to be computed and let $u_j \in V_j^h$ be the large-scale nodal displacement in this substructure

obtained from the solution of the reduced system. The multi-resolution analysis discussed earlier assumes periodicity of the associated functions in their respective domains and also deals with functions in a wavelet basis (V^w). Thus, in order to use the multi-resolution procedure to compute the fine-scale displacements, we first need to find an equivalent, *periodic* large-scale nodal displacement function and convert it into an equivalent function in V_j^w .

3.7.1 Computing the periodic large-scale nodal displacements

It is assumed that the fine-scale strain in a substructure, ϵ^{fine} , can be expressed as the sum of a periodic fine-scale strain in an equivalent periodic substructure and a large-scale non-periodic strain, i.e.,

$$\epsilon^{fine} = \epsilon_P^{fine} + \epsilon_{NP}^{coarse} \quad (3.93)$$

where the subscripts P and NP denote periodic and non-periodic, respectively. This assumption in fact means that the non-periodic component of the strain is large-scale in nature. In addition, it is assumed that the large-scale displacement in the substructure, u_j , can also be expressed as a sum of a periodic component and a non-periodic component, i.e.,

$$u_j = u_j^P + u_j^{NP} \quad (3.94)$$

This assumption is illustrated in figure 3.12, where a typical non-periodic displacement function is shown to be composed of a non-periodic component and a periodic component.

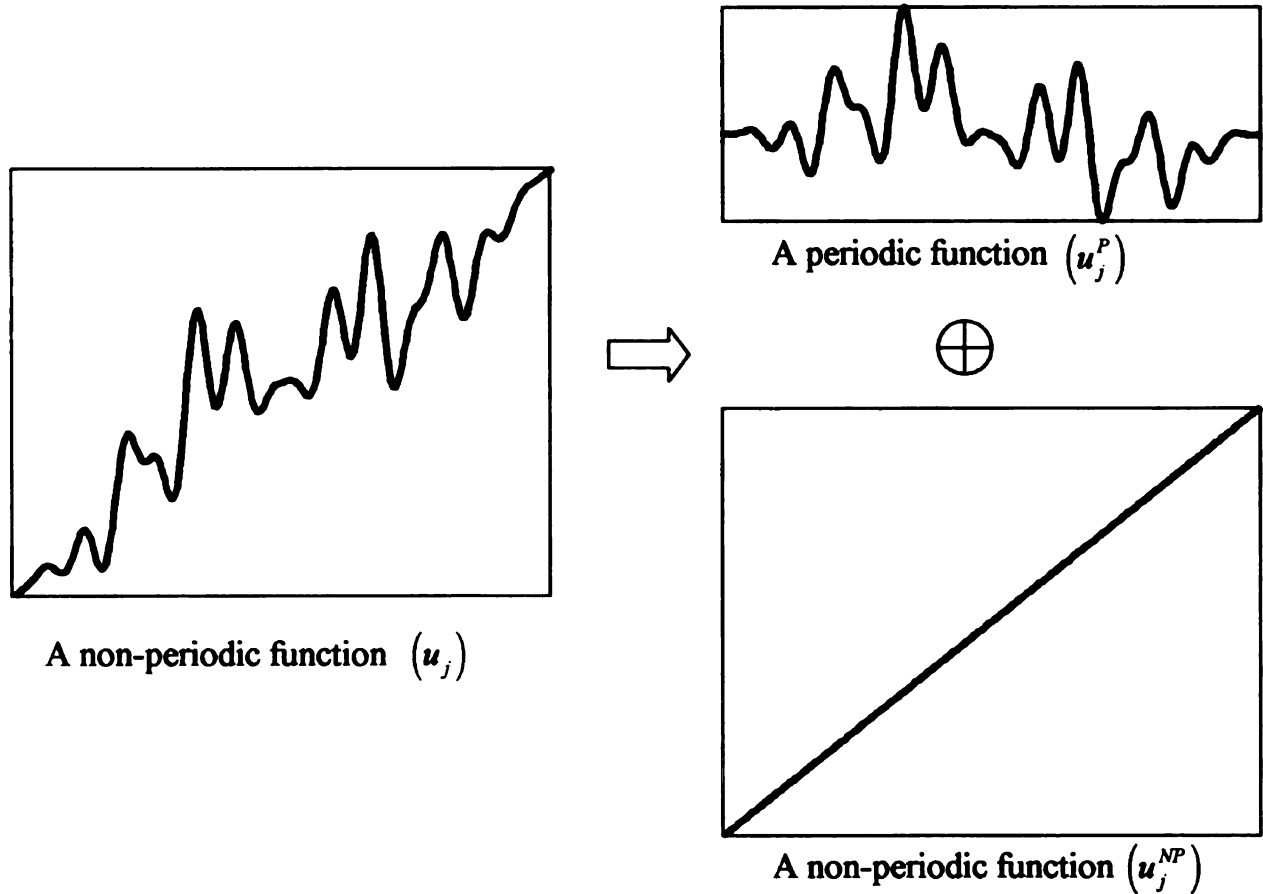


Figure 3.12. Decomposition of a general non-periodic function into a coarse,

The coarse-scale strain energy in the substructure can be expressed as

$$U^c = \frac{1}{2} \int_{\Omega_c} \bar{E}_j \varepsilon(u_j) \varepsilon(u_j) dy \quad (3.95)$$

Using (3.94) this can be expressed as

$$\begin{aligned}
 U^c &= \frac{1}{2} \int_{\Omega_c} \bar{E}_j \varepsilon(u_j^P) \varepsilon(u_j^P) dy + \frac{1}{2} \int_{\Omega_c} \bar{E}_j \varepsilon(u_j^{NP}) \varepsilon(u_j^{NP}) dy \\
 &+ \int_{\Omega_c} \bar{E}_j \varepsilon(u_j^P) \varepsilon(u_j^{NP}) dy
 \end{aligned} \quad (3.96)$$

It should be noted that the augmentation process does not add any strain energy into the system, it merely computes the fine-scale displacements associated with the same coarse-

scale strain energy. It can be shown that the strain energy associated with a periodic stiffness matrix at a level J is the same as the strain energy computed from a consistently reduced stiffness matrix at level $J-k$, i.e., the multi-resolution reduction scheme conserves strain energy. Thus, it would be useful to express the strain energy purely as the sum of one due to periodic displacements and another due to non-periodic displacements. This would require the last term in the right hand side of (3.96) to be equal to zero, i.e., the periodic component of the displacement needs to be orthogonal to the non-periodic component with respect to the energy inner product, $\langle \cdot, \cdot \rangle_E$, defined as

$$\langle \cdot, \cdot \rangle_E = \int_{\Omega_c} \bar{E}_j \varepsilon(\cdot) \varepsilon(\cdot) dy \quad (3.97)$$

such that the strain energy due to the coupled (periodic and non-periodic) terms is zero.

Thus, we look to decompose the displacement u_j according to equation (3.94) such that

$$\langle u_j^P, u_j^{NP} \rangle_E = 0 \quad (3.98)$$

Using equation (3.94), we can write this as

$$\langle u_j^P, (u_j - u_j^P) \rangle_E = 0 \quad (3.99)$$

Expanding equation (3.99) we get

$$\int_{\Omega_c} \bar{E}_j \varepsilon(u_j^P) \varepsilon(u_j - u_j^P) dy = \int_{\Omega_c} \bar{E}_j \varepsilon(u_j) \varepsilon(u_j^P) dy \quad (3.100)$$

Define a matrix \mathbf{D}_j such that,

$$\left[\mathbf{u}_j^P \right]^T \mathbf{D}_j \mathbf{u}_j = \int_{\Omega_c} \bar{E}_j \varepsilon(u_j) \varepsilon(u_j^P) dy \quad (3.101)$$

In the discretized form, equation (3.100) becomes

$$\left[\mathbf{u}_j^P \right]^T \bar{\mathbf{K}}_j \mathbf{u}_j^P = \left[\mathbf{u}_j^P \right]^T \mathbf{D}_j \mathbf{u}_j \quad (3.102)$$

where $\bar{\mathbf{K}}_j$ is the periodic nodal stiffness matrix of dimensions $2n^2 \times 2n^2$. The matrix \mathbf{D}_j (of dimensions $2n^2 \times 2(n+1)^2$) could be thought of as one that transforms a vector of non-periodic nodal displacements into a periodic nodal body force. A candidate \mathbf{u}_j^P is such that it satisfies the system of equations

$$\bar{\mathbf{K}}_j \mathbf{u}_j^P = \mathbf{D}_j \mathbf{u}_j \quad (3.103)$$

This ensures that equation (3.102) is satisfied and that the total strain energy can then be expressed as the sum of the strain energy due to periodic displacements and that due to the coarse, non-periodic displacements.

The periodic displacement vector \mathbf{u}_j^P obtained by solving equation (3.103) is one that corresponds to the nodal values of the displacement function in a periodic substructure. In order to apply the multi-resolution analysis to this function it needs to be expressed in an equivalent wavelet basis, this conversion is described next.

3.7.2 Conversion to a Wavelet Basis

The conversion of a periodic function in the finite-element (nodal) basis V^h into an equivalent function in a wavelet basis V^w is proposed using the reverse of the process described in section 3.4.2.3. According to this scheme a periodic nodal displacement \mathbf{u}_j^P can be converted into the equivalent wavelet displacement function $\bar{\mathbf{u}}_j \in V_j^w$ as

$$\bar{\mathbf{u}}_j = \mathbf{H}_j^{-1} \mathbf{B}_j \mathbf{u}_j^P \quad (3.104)$$

where \mathbf{H}_j is a reduced stiffness matrix of the substructure in a wavelet basis and \mathbf{B}_j is a matrix that transforms a given periodic nodal displacement into an equivalent body force in a wavelet basis. Once this coarse-scale displacement function in the wavelet basis has been computed, it can then be refined using the reverse of the multi-resolution analysis discussed in section 3.4.1 to obtain the fine-scale displacement function. This process is described next.

3.7.3 Periodic Multi-Resolution Refinement

Recall the multi-resolution reduction scheme discussed in section 3.4.1. As expressed in (3.28) a single stage wavelet transform applied to a system represented by the equations $\mathbf{L}_{j+1}\mathbf{u}_{j+1} = \mathbf{f}_{j+1}$ yields the partitioned system

$$\begin{aligned} \mathcal{W}\mathbf{L}_{j+1}\mathcal{W}^T(\mathcal{W}\mathbf{u}_{j+1}) &= \mathcal{W}\mathbf{f}_{j+1} \\ \Leftrightarrow \begin{bmatrix} \mathbf{L}_j & \mathbf{C}_j \\ \mathbf{C}_j^T & \mathbf{A}_j \end{bmatrix} \begin{bmatrix} \bar{\mathbf{u}}_j \\ \tilde{\mathbf{u}}_j \end{bmatrix} &= \begin{bmatrix} \bar{\mathbf{f}}_j \\ \tilde{\mathbf{f}}_j \end{bmatrix} \end{aligned}$$

Thus, given the coarse-scale displacement $\bar{\mathbf{u}}_j$, the detail components $\tilde{\mathbf{u}}_j$ of the displacement at scale j can be obtained from

$$\tilde{\mathbf{u}}_j = \mathbf{A}_j^{-1}\tilde{\mathbf{f}}_j - \mathbf{A}_j^{-1}\mathbf{C}_j^T\bar{\mathbf{u}}_j \quad (3.105)$$

where \mathbf{A}_j and \mathbf{C}_j are as defined in equation (3.29). Under the assumption that the force is slow-varying (i.e., $\tilde{\mathbf{f}} = \mathbf{0}$), the detail component is given as

$$\tilde{\mathbf{u}}_j = -\mathbf{A}_j^{-1}\mathbf{C}_j^T\bar{\mathbf{u}}_j \quad (3.106)$$

The displacement at scale $j+1$ can then be obtained using the inverse wavelet transform, \mathcal{W}^{-1} , as follows



$$\bar{\mathbf{u}}_{j+1} = \mathcal{W}^{-1} \begin{bmatrix} \bar{\mathbf{u}}_j \\ \tilde{\mathbf{u}}_j \end{bmatrix} \quad (3.107)$$

This process (equations (3.106) and (3.107)) is recursively repeated several times to obtain the displacement at finest scale J .

Once the fine-scale displacement has been computed, the total fine-scale strain in the substructure is then obtained by adding the fine-scale periodic strain, $\varepsilon(\mathbf{u}_J)$, to the non-periodic coarse strain, $\varepsilon(\mathbf{u}_j^{NP})$, i.e., using

$$\varepsilon_J = \varepsilon(\mathbf{u}_J) + \varepsilon(\mathbf{u}_j^{NP}) \quad (3.108)$$

The fine-scale stresses can be obtained using this strain and the material distribution in the given substructure

$$\sigma_J(\mathbf{y}) = E_J(\mathbf{y})\varepsilon_J(\mathbf{y}) \quad (3.109)$$

where E_J represents the elastic tensor.

3.8 Numerical Examples

This section presents numerical examples that illustrate and compare the schemes presented in this chapter. (Images in this dissertation are presented in color.)

3.8.1 Example 1

The first example considered is a square plate with circular perforations of various sizes subject to a uniform compressive load at the tip as shown in figure 3.13. Here the solid material is assumed to have a Young's modulus of 0.91 and the weak (void) material with a Young's modulus of 0.045 with a Poisson's ratio of 0.3 in both.

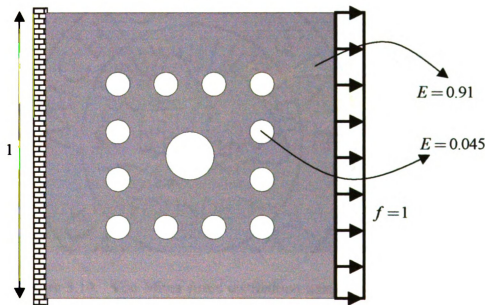


Figure 3.13. Geometry and boundary conditions for example 1

This structure is modeled at a fine-scale that resolves all the features of the material distribution using a commercial finite-element software. The total number of degrees of freedom in the model is 74,498. The compliance of the structure is 0.671. The maximum displacement is at the center of the right edge and is of magnitude 1.44. Figure 3.14

shows the distribution of Von Mises stress from this fine-scale model. The maximum Von Mises stress in the structure is 2.69 near the center perforation.

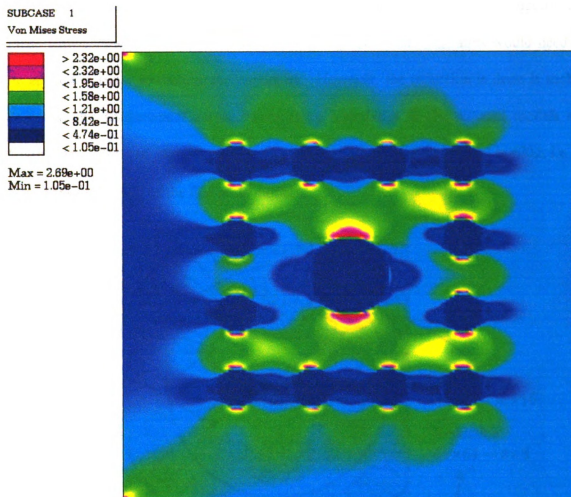


Figure 3.14. Von Mises stress distribution using the fine-scale model of the structure in example 1. (Number of degrees of freedom = 74,498)

Figure 3.15 shows the assembly of 33 substructures used in constructing the reduced model of the structure. The substructure in the center is modeled at a fine-scale corresponding to a 64×64 pixel discretization and reduced to a scale corresponding to a 16×16 discretization. All the other substructures are also modeled at a fine-scale that

1950



UNIVERSITY OF CALIFORNIA

1950

corresponds to a 64×64 discretization but are reduced to one that corresponds to an 8×8 discretization. It is noted that if all the substructures were to be modeled in the given fine scales then the displacement across the boundary between the central substructure and those surrounding it would not be continuous, i.e., additional constraints would need to be applied in order to enforce the continuity. However, the reduction is done in such a way that the displacement across substructure boundaries in the reduced models are continuous. The total number of degrees of freedom in the reduced model is 4802, i.e., it is approximately $\frac{1}{16}$ of the fine-scale model.

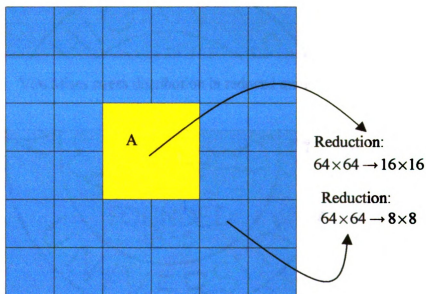


Figure 3.15. Assembly of substructures for example 1

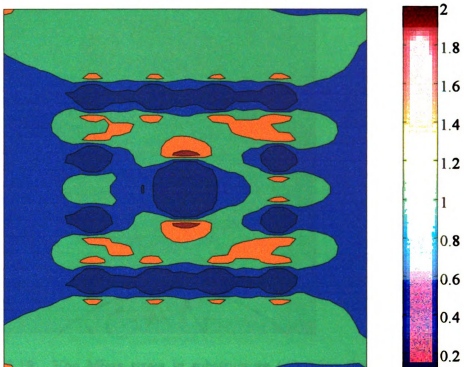


Figure 3.16. Von Mises stress distribution in reduced model using material MRA

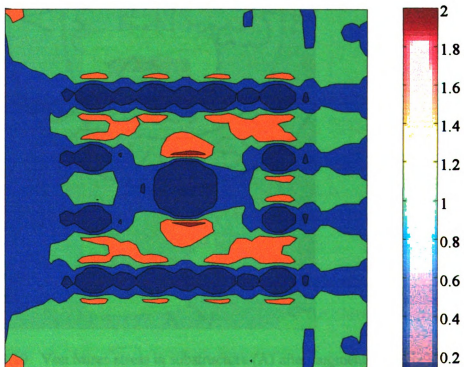


Figure 3.17. Von Mises stress distribution in reduced model using displacement MRA

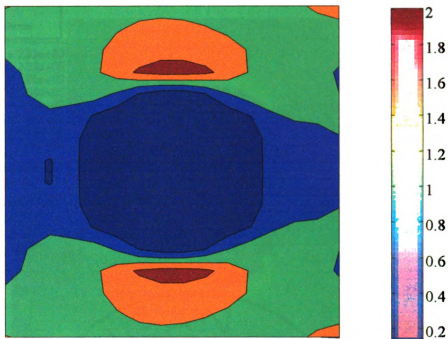


Figure 3.18. Von Mises stress in substructure (A) using the reduced model

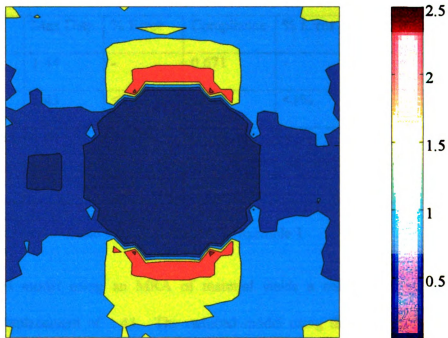


Figure 3.19. Von Mises stress in substructure (A) after augmentation

100
100

THE UNIVERSITY OF CHICAGO



UNIVERSITY OF CHICAGO

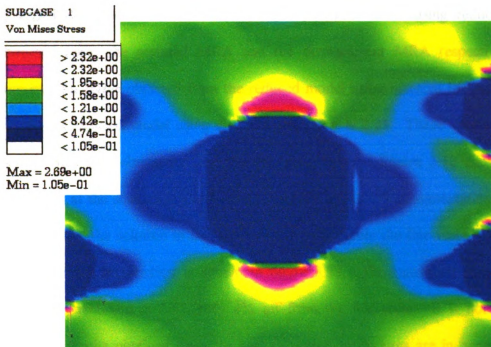


Figure 3.20: Detail of the Von Mises stress near substructure (A) obtained using the fine-scale model

	Max Disp	% Error	Compliance	% Error	Max. σ_{von}	% Error
Fine-Scale	1.44	-	0.671	-	2.69	-
Material MRA	1.43	<1%	0.667	<1%	2.21	17%
Displacement MRA	1.44	<1%	0.675	<1%	2.25	16%
Augmented	-	-	-	-	2.57	4%

Table 3.1: Main results for example 1

The reduced model using an MRA of material yields a compliance of 0.667 and a maximum displacement of 1.43. The reduced model using the MRA of displacements yields a compliance of 0.675 and a maximum displacement of 1.44. These values are very close (less than 1% difference) to that obtained using the fine-scale model. Figures

3.16 and 3.17 show the distribution of the Von Mises stress using reduced models constructed using the material MRA and the displacement MRA respectively. The maximum Von Mises obtained from the reduced model using material MRA is 2.21 and that from the reduced model using displacement MRA is 2.25. These values are almost 17% less than that obtained using the fine-scale model. Figure 3.18 shows a more detailed look at the stresses in the central substructure (A). The augmentation procedure is performed on the solution in this substructure to compute the fine-scale stresses. The augmented stress distribution is shown in figure 3.19. The maximum stress obtained after the augmentation is 2.57, only 4% off from the fine-scale. It is noted that the coarse-scale results obtained from the two reduction procedures are in general not too different. However, in the case of displacement MRA, it was possible to carry out an augmentation procedure and compute the stresses with a greater accuracy at the desired location.

3.8.2 Example 2

The next example considered is the structure shown in figure 3.21. As before, the solid material has Young's modulus of 0.91 and the weak material (void) has Young's modulus of 0.045. Poisson's ratio is 0.3 in both cases.

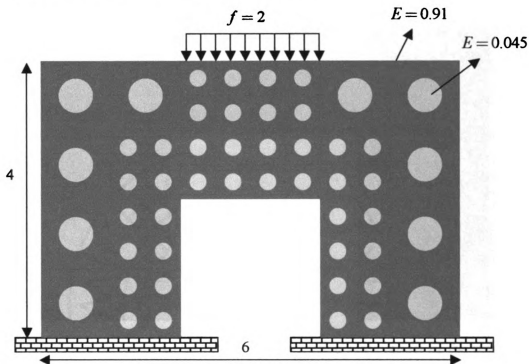


Figure 3.21. Geometry and boundary conditions for example 2

The fine-scale model of the structure consists of 163,840 degrees of freedom and is computed using a commercial finite element software. The compliance of the structure is 6.96 and the maximum displacement is 7.66 and is observed at the center of the top edge. Figure 3.22 shows the distribution of Von Mises stress in the structure. The maximum stress (as expected) is observed near the sharp corners and the magnitude of the maximum stress obtained is 4.72.

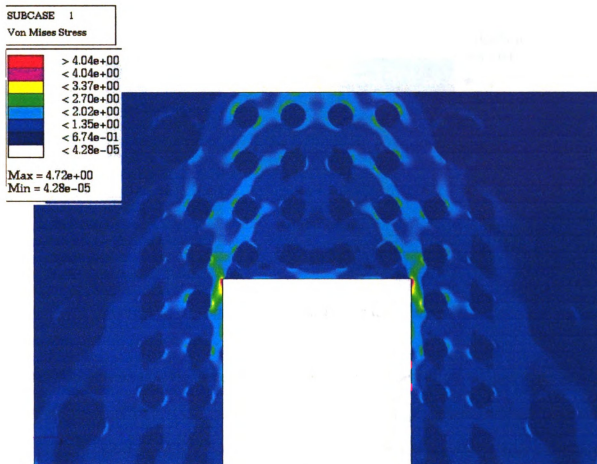
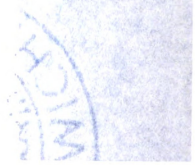


Figure 3.22: Von Mises stress distribution from fine-scale model of the structure with 163,840 degrees of freedom

Figure 3.23 shows the arrangement of 50 substructures used in constructing the reduced model of the given structure. The substructures in the outer periphery of the structure with large perforations are modeled at a fine-scale that corresponds to a 64×64 uniform discretization and reduced to an equivalent of a 16×16 discretization. The other smaller substructures are also modeled using the same fine-scale discretization but are reduced to an equivalent of an 8×8 discretization. The total number of degrees of freedom in the reduced model is 10,240.

10-4215
10-4216
10-4217
10-4218
10-4219
10-4220
10-4221
10-4222
10-4223
10-4224
10-4225
10-4226
10-4227
10-4228
10-4229
10-4230
10-4231
10-4232
10-4233
10-4234
10-4235
10-4236
10-4237
10-4238
10-4239
10-4240
10-4241
10-4242
10-4243
10-4244
10-4245
10-4246
10-4247
10-4248
10-4249
10-4250
10-4251
10-4252
10-4253
10-4254
10-4255
10-4256
10-4257
10-4258
10-4259
10-4260
10-4261
10-4262
10-4263
10-4264
10-4265
10-4266
10-4267
10-4268
10-4269
10-4270
10-4271
10-4272
10-4273
10-4274
10-4275
10-4276
10-4277
10-4278
10-4279
10-4280
10-4281
10-4282
10-4283
10-4284
10-4285
10-4286
10-4287
10-4288
10-4289
10-4290
10-4291
10-4292
10-4293
10-4294
10-4295
10-4296
10-4297
10-4298
10-4299
10-4300



10-4215
10-4216
10-4217
10-4218
10-4219
10-4220
10-4221
10-4222
10-4223
10-4224
10-4225
10-4226
10-4227
10-4228
10-4229
10-4230
10-4231
10-4232
10-4233
10-4234
10-4235
10-4236
10-4237
10-4238
10-4239
10-4240
10-4241
10-4242
10-4243
10-4244
10-4245
10-4246
10-4247
10-4248
10-4249
10-4250
10-4251
10-4252
10-4253
10-4254
10-4255
10-4256
10-4257
10-4258
10-4259
10-4260
10-4261
10-4262
10-4263
10-4264
10-4265
10-4266
10-4267
10-4268
10-4269
10-4270
10-4271
10-4272
10-4273
10-4274
10-4275
10-4276
10-4277
10-4278
10-4279
10-4280
10-4281
10-4282
10-4283
10-4284
10-4285
10-4286
10-4287
10-4288
10-4289
10-4290
10-4291
10-4292
10-4293
10-4294
10-4295
10-4296
10-4297
10-4298
10-4299
10-4300

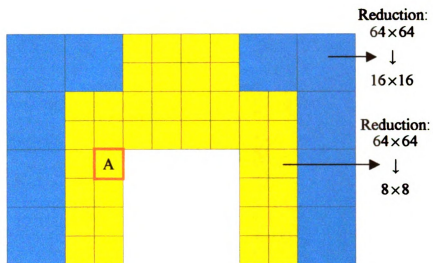


Figure 3.23. Arrangement of substructures for example 2

The reduced model using material MRA predicts a compliance of 6.7 and a maximum displacement of 7.35. The compliance and maximum displacement obtained from the reduced model using displacement MRA are 6.7 and 7.4 respectively. These values are very close to those obtained from the fine-scale model. Figures 3.24 and 3.25 show the Von Mises distribution obtained from reduced models build using the material MRA and displacement MRA respectively. The maximum Von Mises stress from the material MRA reduced model is 3.19 and that from the displacement MRA reduced model is 3.22. These are approximately 30% less than the maximum stress obtained from the fine-scale model. Figure 3.26 shows the coarse-scale stress in substructure (A). The fine-scale stresses in (A) are computed by the augmentation procedure and are shown in figure 3.27. The maximum stress after augmentation is 4.2. This is still off from the fine-scale result by about 11%.

THE UNIVERSITY OF CHICAGO

THE UNIVERSITY OF CHICAGO
DIVISION OF THE PHYSICAL SCIENCES
DEPARTMENT OF CHEMISTRY
5780 SOUTH CAMPUS DRIVE
CHICAGO, ILLINOIS 60637
TEL: 773-936-3700
FAX: 773-936-3700

THE UNIVERSITY OF CHICAGO
DIVISION OF THE PHYSICAL SCIENCES
DEPARTMENT OF CHEMISTRY
5780 SOUTH CAMPUS DRIVE
CHICAGO, ILLINOIS 60637
TEL: 773-936-3700
FAX: 773-936-3700

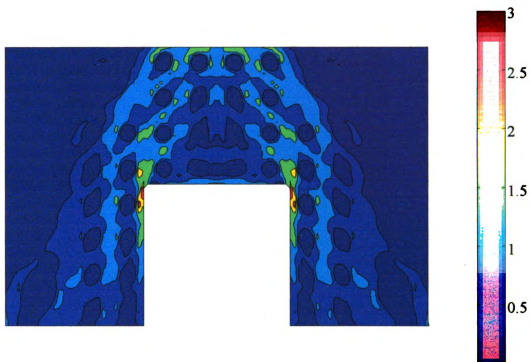


Figure 3.24. Von Mises stress distribution from a reduced model using material MRA

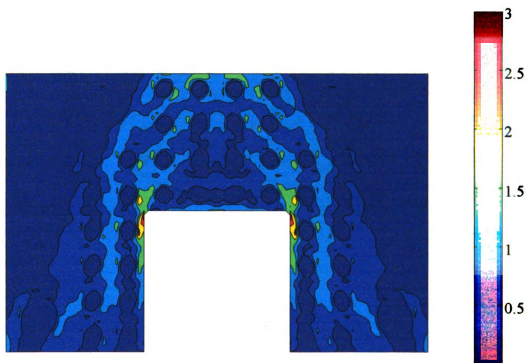


Figure 3.25. Von Mises stress distribution from a reduced model using displacement MRA



FIG. 10. Difference in the time-averaged monthly mean precipitation rate (mm day^{-1}) between the control and the 1000-K experiment. Contour interval is 0.5 mm day^{-1} . Shaded region indicates where the difference is statistically significant at the 95% confidence level.

6. Diagnostics of the 1000-K experiment

As shown in Fig. 10, the 1000-K experiment produces a significant decrease in precipitation over the tropical Pacific and Indian Oceans, and a significant increase over the tropical Atlantic and parts of the Indian Ocean. The precipitation changes are consistent with the changes in the cloud cover and cloud droplet number concentration.

The cloud cover and cloud droplet number concentration changes are consistent with the changes in the cloud droplet growth rate and the cloud droplet activation rate.

The cloud droplet growth rate and the cloud droplet activation rate changes are consistent with the changes in the cloud droplet growth rate and the cloud droplet activation rate.

The cloud droplet growth rate and the cloud droplet activation rate changes are consistent with the changes in the cloud droplet growth rate and the cloud droplet activation rate.

The cloud droplet growth rate and the cloud droplet activation rate changes are consistent with the changes in the cloud droplet growth rate and the cloud droplet activation rate.

The cloud droplet growth rate and the cloud droplet activation rate changes are consistent with the changes in the cloud droplet growth rate and the cloud droplet activation rate.

The cloud droplet growth rate and the cloud droplet activation rate changes are consistent with the changes in the cloud droplet growth rate and the cloud droplet activation rate.

The cloud droplet growth rate and the cloud droplet activation rate changes are consistent with the changes in the cloud droplet growth rate and the cloud droplet activation rate.

The cloud droplet growth rate and the cloud droplet activation rate changes are consistent with the changes in the cloud droplet growth rate and the cloud droplet activation rate.

The cloud droplet growth rate and the cloud droplet activation rate changes are consistent with the changes in the cloud droplet growth rate and the cloud droplet activation rate.

The cloud droplet growth rate and the cloud droplet activation rate changes are consistent with the changes in the cloud droplet growth rate and the cloud droplet activation rate.

The cloud droplet growth rate and the cloud droplet activation rate changes are consistent with the changes in the cloud droplet growth rate and the cloud droplet activation rate.

The cloud droplet growth rate and the cloud droplet activation rate changes are consistent with the changes in the cloud droplet growth rate and the cloud droplet activation rate.

The cloud droplet growth rate and the cloud droplet activation rate changes are consistent with the changes in the cloud droplet growth rate and the cloud droplet activation rate.

The cloud droplet growth rate and the cloud droplet activation rate changes are consistent with the changes in the cloud droplet growth rate and the cloud droplet activation rate.

The cloud droplet growth rate and the cloud droplet activation rate changes are consistent with the changes in the cloud droplet growth rate and the cloud droplet activation rate.

The cloud droplet growth rate and the cloud droplet activation rate changes are consistent with the changes in the cloud droplet growth rate and the cloud droplet activation rate.

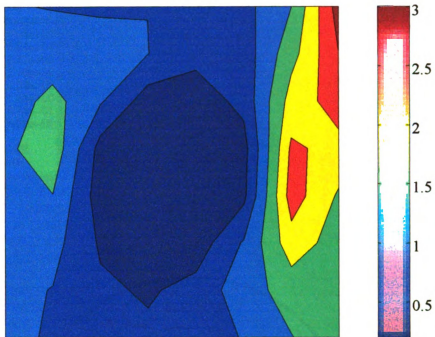


Figure 3.26: Von Mises stress in substructure (A) from the reduced model using displacement MRA

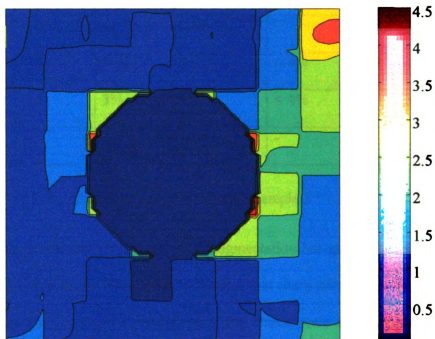


Figure 3.27: Von Mises stress in substructure (A) after augmentation



UNIVERSITY OF CALIFORNIA

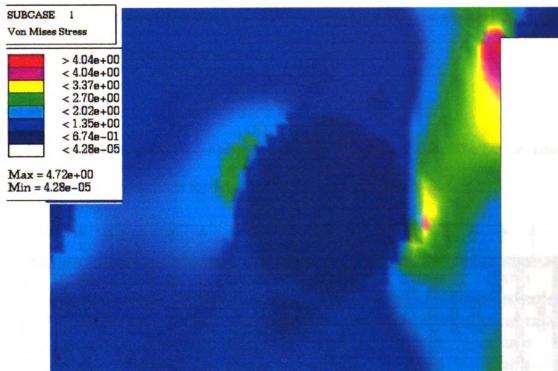


Figure 3.28: Detail of the Von Mises stress in a region around substructure (A) from the fine-scale model

	Max Disp	% Error	Compliance	% Error	Max. σ_{von}	% Error
Fine-Scale	7.66	-	6.96	-	4.72	-
Material MRA	7.35	< 4%	6.7	< 4%	3.19	32%
Displacement MRA	7.4	3%	6.7	< 4%	3.22	31%
Augmented	-	-	-	-	4.2	11%

Table 3.2: Main results for example 2

In this case, the maximum stress even after augmentation has greater than 10% error as compared to the fine-scale. This is due to the fact that sharp corners are locations of high stress gradients and the discretization level at the coarse-scale is not enough to capture

these gradients. Locations of high stress gradients usually need to be modeled at a much finer discretization than the other regions

3.8.3 Example 3

In the last example the material distribution is as shown in figure 3.29. The bottom edge of the frame is clamped and the top edge is subject to a uniform unit load.

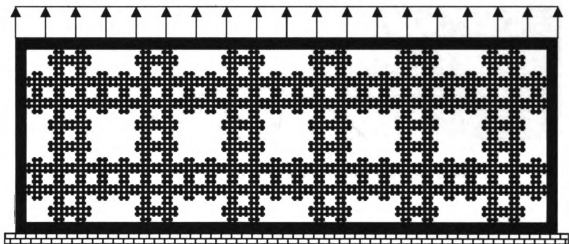


Figure 3.29. Geometry and boundary conditions for example 3

The compliance of the structure obtained from a fine-scale model using a commercial finite element software is 0.765. The maximum displacement is 1.86. Figure 3.30 shows the distribution of the Von Mises stresses obtained from a fine-scale model of the structure. The maximum Von Mises stress is 0.83. The assembly of substructures used in the construction of a reduced model of this structure is illustrated in figure 3.31. The solid rim is not reduced and is modeled in accordance with the continuity requirement across the substructure boundaries. The interior of the structure is modeled using 12 substructures modeled at a fine scale corresponding to a 64×64 mesh and reduced to a 8×8 mesh.

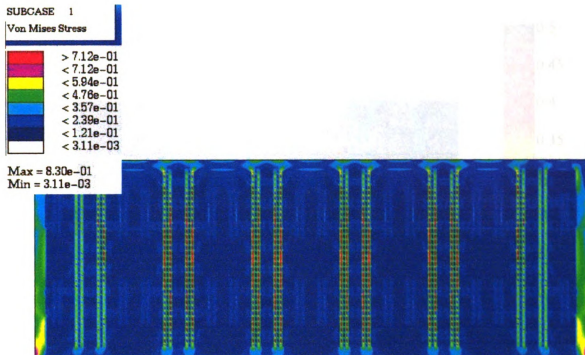


Figure 3.30. Von Mises stress distribution from a fine-scale model

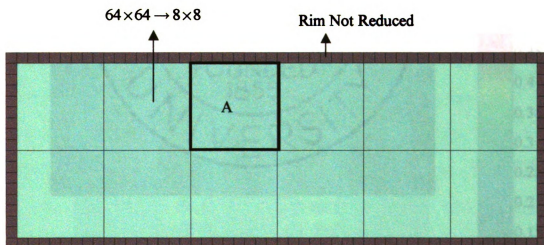


Figure 3.31. Arrangement of substructures for example 3



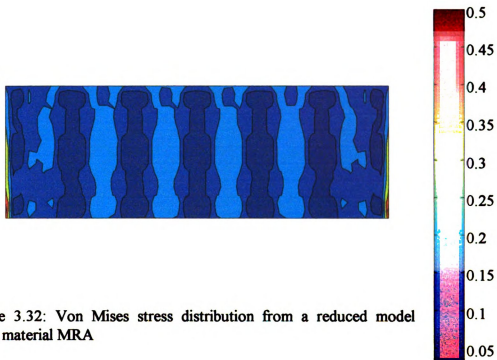


Figure 3.32: Von Mises stress distribution from a reduced model using material MRA

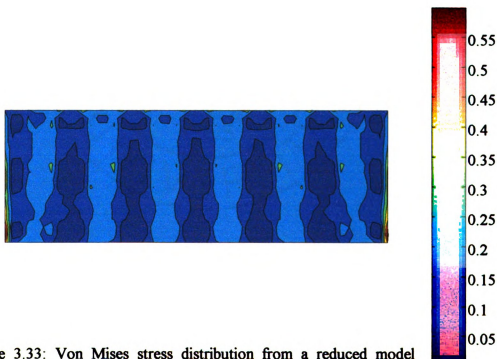


Figure 3.33: Von Mises stress distribution from a reduced model using displacement MRA

1950

1950

1950

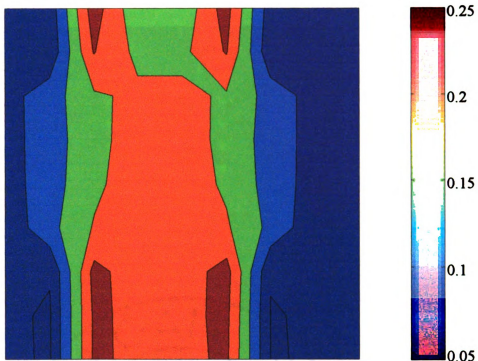


Figure 3.34: Von Mises stress in substructure (A) from the reduced model using displacement MRA

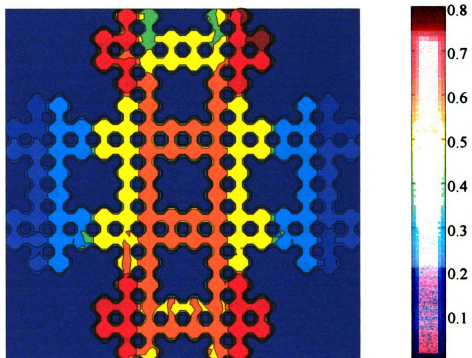


Figure 3.35: Von Mises stress in substructure (A) after augmentation

Figure 1. Schematic diagram of the experimental setup for the study of the effect of the initial concentration of the reactants on the rate of the reaction. The reaction is carried out in a closed system at constant volume and temperature. The initial concentration of the reactants is varied by changing the volume of the reactants.

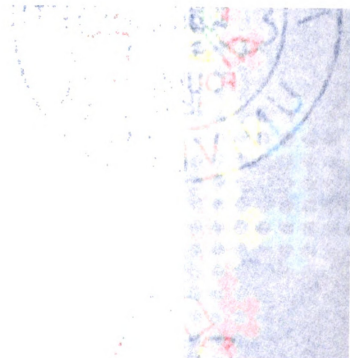


Figure 1. Schematic diagram of the experimental setup for the study of the effect of the initial concentration of the reactants on the rate of the reaction.

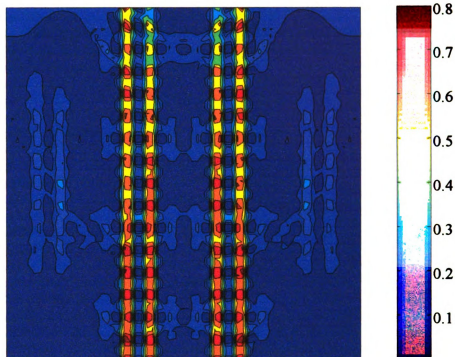


Figure 3.36: Detail of the Von Mises stress in substructure (A) obtained from the fine-scale model

The reduced model using material MRA yields a compliance of 0.724 and a maximum displacement of 1.71. The corresponding results from the reduced model using displacement MRA are: compliance of 0.756 and a maximum displacement of 1.90. Figures 3.32 and 3.33 show the distribution of Von Mises stress obtained from the material MRA model and the displacement MRA model respectively. The maximum Von Mises stress from the material MRA reduced model is 0.61 and that from the displacement MRA model is 0.69. These values of maximum stresses are observed at the bottom corners. The maximum stresses from the reduced model are approximately 20-30% less than that obtained from the fine-scale model. The augmentation procedure is then carried out on substructure (A) and the resulting maximum stress computed. Figures



Figure 1: A line graph showing the relationship between the number of trials and the number of correct responses. The x-axis is labeled 'Number of trials' and ranges from 0 to 10. The y-axis is labeled 'Number of correct responses' and ranges from 0 to 10. The data points are approximately: (1, 1), (2, 2), (3, 3), (4, 4), (5, 5), (6, 6), (7, 7), (8, 8), (9, 9), (10, 10). A dashed line connects the points, showing a linear relationship. A vertical line is drawn at trial 5, and a horizontal line is drawn at 5 correct responses, intersecting at the point (5, 5).

The graph shows a linear relationship between the number of trials and the number of correct responses. The x-axis represents the number of trials, ranging from 0 to 10. The y-axis represents the number of correct responses, ranging from 0 to 10. The data points are approximately: (1, 1), (2, 2), (3, 3), (4, 4), (5, 5), (6, 6), (7, 7), (8, 8), (9, 9), (10, 10). A dashed line connects the points, showing a linear relationship. A vertical line is drawn at trial 5, and a horizontal line is drawn at 5 correct responses, intersecting at the point (5, 5).

3.34 and 3.34 show the coarse-scale stress in substructure (A) and the augmented stress respectively. The maximum Von Mises stress after augmentation is 0.817, only 2% off from the fine-scale result.

	Max Disp	% Error	Compliance	% Error	Max. σ_{von}	% Error
Fine-Scale	1.86	-	0.77	-	0.83	-
Material MRA	1.71	8%	0.72	< 7%	0.61	27%
Displacement MRA	1.9	2%	0.75	< 3%	0.69	17%
Augmented	-	-	-	-	0.82	< 2%

Table 3.3: Main results for example 3

It is noted that the maximum stress from the reduced models are observed at the bottom corners of the outer rim. However, in the fine-scale, the bottom corner stress though considerably large, is not the maximum. The maximum stress in the fine-scale model is observed in the interior substructures (A). In the reduced models, the stresses in the substructure (A) are much less than that in the fine-scale model (compare figures (3.34) and (3.36)). After augmentation the maximum stresses are only 2% less than the fine-scale result. But, the augmentation over estimates the locations of the maximum stresses, i.e., the locations of maximum stresses after augmentation are spread out over a larger area than as computed from the fine-scale result. Nevertheless, as seen by comparing figures (3.34) and (3.35), there is a tremendous increase in the accuracy of the magnitude of maximum stress computed in substructure (A) using the reduced model after augmentation.

Chapter 4

Multi-Scale Layout Optimization Of Structures

In this chapter, some strategies for the optimal layout design of structural systems using materials with finite-scale heterogeneities are presented. The standard methods that are commonly used to solve these problems are either homogenization-based techniques that involve materials with infinitesimal heterogeneities (microstructures) (refer Bendsoe and Kikuchi [2], Diaz and Bendsoe [12]) or methods that use fictitious material models (see Bendsoe [3], Rozvany et al [33,34]). Structural systems involving many finite-scale heterogeneities yield very large systems of equations that are not suitable for the kind of iterative solution schemes that are required in the case of optimization problems. The main goal in this chapter is to propose strategies that incorporate the model reduction techniques discussed earlier into a problem of layout optimization of structural systems where finite-scale features can be accounted.

This chapter is arranged as follows: section 4.1 gives a brief introduction to the problem of layout optimization of structures and the standard techniques used to solve these problems. The next section, section 4.2, introduces the problem of optimizing the layout with finite-scale materials. There, a simplified version of this problem using perforations as a prototype for heterogeneities is presented and the associated sensitivity analysis is outlined. Section 4.3 discusses the formulation of compliance minimization problems using perforated substructures. Section 4.4 illustrates the solution of compliance minimization problems using fixed layouts of substructures. The next section, section 4.5, deals with the dependence of the optimal layout on the arrangement of various sizes of substructures. Here, the formulation and solution of compliance minimization problems with varying layouts of substructures are discussed. Finally, numerical results are presented in section 4.6.

4.1. Background: Topology Optimization of Structures

Topology optimization problems in general seek to find the optimal layout of a structure in a prescribed design space using a given amount of material, subject to constraints on the response of the structure under prescribed loading conditions. Typical objective functions involve: mean compliance, total mass, eigenvalues. Typical constraints include volume and stress (e.g. see Suzuki and Kikuchi [36], Diaz and Kikuchi [13], Duysinx and Bendsoe [16], Haber et al [23]).

A typical topology optimization problem can be expressed as a problem that seeks an optimal distribution of the elasticity tensor $E_{ijkl}(x)$ over the design domain, Ω , by writing

$$E_{ijkl}(x) = \chi(x) \bar{E}_{ijkl} \quad (4.1)$$

where \bar{E}_{ijkl} is a reference tensor and $\chi(x)$ is an indicator function for the part Ω^m of Ω that is occupied by material, i.e.,

$$\chi(x) = \begin{cases} 1 & \text{if } x \in \Omega^m \\ 0 & \text{if } x \in \Omega \setminus \Omega^m \end{cases} \quad (4.2)$$

An approach to solving such optimization problems using finite elements results in each point, x , in the domain having the discrete choice of having material or no material, i.e., this distributed parameter optimization problem is formulated using a discrete valued parameter function. The solution of this type of problems requires the use of discrete optimization algorithms. However, such an approach would be unstable with respect to the choice of elements and the discretization mesh, as the distributed problem, in general, does not have a solution unless composite materials are introduced (see Kohn and Strang [25], Murat and Tartar [29]). An alternative solution to this problem was introduced by Bendsoe and Kikuchi [2]. According to this scheme, rather than determining the mixture of two materials at the macroscopic level, the mixture is allowed to occur at an infinitesimal scale. This leads to a problem formulation using material with a microstructure, i.e., a material with microscopic perforations of different sizes controlled by the introduction of a parameter called *effective density* (volume occupied by material in a characteristic unit-cell), which may vary continuously from 0 to 1, the two limiting cases being the void and a solid material and the intermediate densities correspond to a composite material. The relation between the effective density and the material tensor, $E_{ijkl}(x)$, is determined through the use of a homogenization method,

where the material distribution at the microscopic level is used to determine the effective properties of the material at the macroscopic level. Figure 4.1 shows a structure that is composed of a periodic composite microstructure.

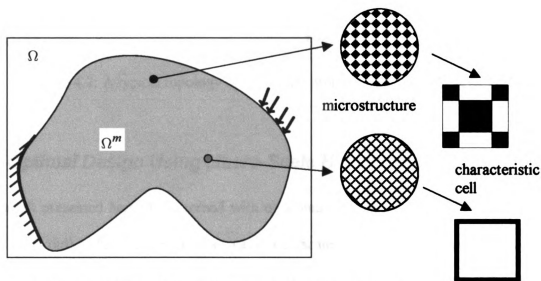


Figure 4.1: A structure with a composite microstructure

Another approach to solve the problem is by introducing an artificial density function $\mu(x)$, $x \in \Omega$, $0 < \mu(x) \leq 1$, $p > 1$ and defining the elasticity tensor as

$$E_{ijkl}(x) = [\mu(x)]^p \bar{E}_{ijkl} \quad (4.3)$$

This model is known as the Solid Isotropic Material with Penalization (SIMP) model (see Rozvany et al [33, 34]) and yields results with fictitious materials of low stiffness for intermediate densities for sufficiently large value of the penalty factor, i.e., it forces the material at each point to have an effective density that is either close to being solid or void. Figure 4.2 illustrates a typical topology optimization problem and its solution.

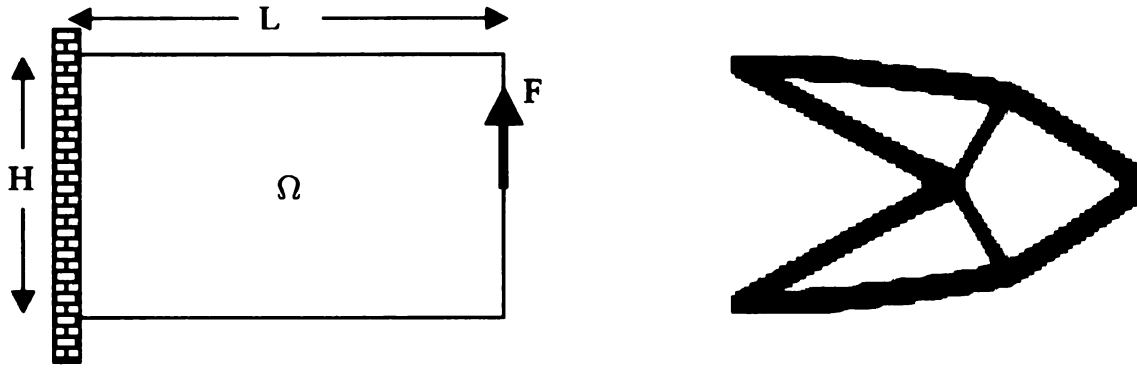


Figure 4.2: A typical topology optimization problem and solution

4.2. Optimal Design Using Macro-Scale Heterogeneities

The work presented here is concerned with obtaining optimal mixtures of two materials (solid and void) at finite scales (macro-scale), i.e., scales that may even be comparable to the dimensions of the structure. Furthermore, it is assumed that the boundary of the desired structure is known a-priori. This is different from the case of standard topology optimization problems where finding the boundaries is part of the problem. The problem is now reduced to one of finding the optimal arrangement of finite-size heterogeneities on a prescribed domain. The heterogeneities may be of any type; however, to illustrate the idea, this discussion deals with perforations as the macro-scale heterogeneities.

A typical structure with finite-scale perforations is illustrated in Figure 4.3. The optimization problem seeks to find the locations and the sizes of various perforations in the given domain. The implementation of this kind of an optimization problem using standard techniques such as finite element methods requires the domain to be suitably discretized and this usually involves adapting the geometry of the structure to a conforming mesh. Since the layout of the material keeps changing during the course of the optimization process, repeated re-meshing of the structure would be required at each

stage of the optimization problem, making this process not only computation-intensive but also difficult to automate.



Figure 4.3: A typical structure with macro-scale heterogeneities (perforations)

One possible approach to solving such problems is proposed here, using the substructuring idea described in the previous chapter. The proposed method seeks to build structures in a given design domain Ω , that can be expressed as the union of regular substructures, Ω_c , in such a way that all the perforations lie in the interior of the substructures, i.e.,

$$\Omega = \bigcup_c \Omega_c \text{ and } \delta\Omega_c \cap \Omega^P = \emptyset \quad (4.4)$$

where Ω^P represents the perforated portions of the domain. The substructures can be of different sizes and in general each substructure can include more than one perforation. One could construct *libraries* (databases) of such substructures (stiffness matrices) of various sizes and types of perforations. The optimization problem would then be approximated into one that seeks to build a structure as an assembly of an optimal

selection of substructures chosen from a library of perforated substructures of various sizes. As a result of the assumption on the design domain (4.4), the optimal structure obtained as an assembly of selected substructures cannot have overlapping perforations and the geometry of the perforations are limited to those in the pre-computed library of perforated substructures. An example of such a structure is illustrated in Figure 4.4.

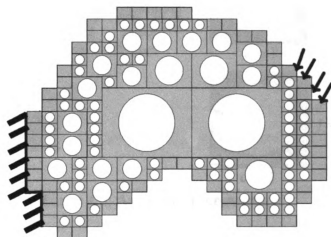


Figure 4.4: A structure built from an assembly of substructures with circular perforations

4.2.1 Building a model using reduced substructures

Here, some relevant features of the construction of a model (stiffness matrix of a structure) using reduced stiffness matrices of substructures are presented. Consider a structure assembled from square substructures of various sizes and with various sizes of circular perforations as shown in Figure 4.5. The structure is represented using five different substructures of three different sizes, L , $2L$ and $4L$. Let J_c be the level of the discretization required to resolve the material distribution in a substructure c , such that



11/11/11 11:11:11

11/11/11 11:11:11

11/11/11 11:11:11

the discretization corresponds to a uniform mesh with spacing equal to $S_c = \frac{L_c}{2^{J_c}}$, where

L_c is the dimension of the substructure.

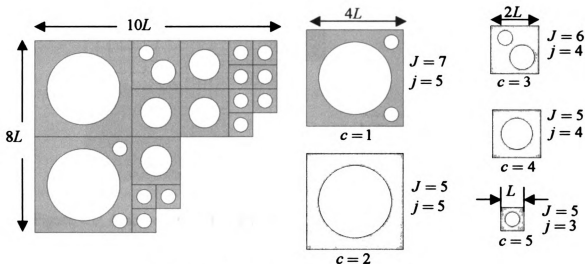


Figure 4.5: Assembly of substructures

Substructures of the same size (e.g., 1, 2 and 3, 4) may require a different resolution scale, depending upon the size of the perforations in them. In the figure, it is assumed that substructures 2, 4 and 5 are discretized at the same level $J_c = 5$. However, the

spacing of the degrees of freedom in each of these substructures is: $S_2 = \frac{4L}{2^5} = \frac{L}{8}$,

$S_4 = \frac{2L}{2^5} = \frac{L}{16}$ and $S_5 = \frac{L}{2^5} = \frac{L}{32}$. While substructures 1 and 3 are discretized at

different levels, $J_1 = 7$ and $J_3 = 6$, the spacing in these substructures is the same,

$S_1 = \frac{4L}{2^7} = \frac{L}{32}$ and $S_3 = \frac{2L}{2^6} = \frac{L}{32}$. Notice that in the fine scale problem when S_c is

different in two adjacent substructures, a one pixel – one element finite element discretization is in general not conforming and would require additional constraints in

order to enforce continuity across substructure boundaries. An example of such a non-conforming mesh is shown in Figure 4.6.

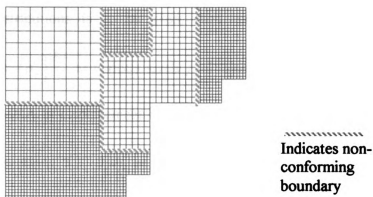


Figure 4.6: A non-conforming assembly of discretized substructures

The reduction of each substructure is performed such that the displacement across boundaries of adjacent reduced substructures is continuous, thus avoiding additional constraints to enforce inter-substructure compatibility. This requirement leads to the following condition on the reduced discretization level of a substructure,

$$\Delta_c = L_c / 2^{j_c} = \Delta \quad (4.5)$$

for $c = 1, 2, \dots, N_c$. For the substructures shown in Figure 4.5, this implies that $j_1 = j_2 = j_5 + 2$ and $j_3 = j_4 = j_5 + 1$. It is emphasized at this point that these relations do not determine the finest scale at which a substructure is to be modeled.

4.2.2 Constructing libraries of perforated substructures

Here, the construction of libraries (databases) of stiffness matrices and material distributions associated with perforated substructures is discussed. A particular type of (parameterizable) perforation is chosen and a set of material distribution functions

$\{\rho_J^c\}^{(k)}$ associated with a discrete set of design variables in a substructure of size L are constructed at a suitably chosen fine scale J . If a reduction based on the MRA of material distributions is to be used, then the library consists of reduced material distributions $\{\rho_j^c\}^{(k)}$ at various levels j , obtained using the process described in section 3.2. If an MRA of displacement is used, the library consists of reduced stiffness matrices $\{\mathbf{K}_j^c\}^{(k)}$ (sections 3.3, 3.4), at levels $j = J, J-1, \dots, 3$ ($j = 3$ is the smallest level possible when using D6 wavelets). This library is comparable to the library of effective material tensors used in some topology optimization problems (see Suzuki and Kikuchi [36]) and needs to be constructed only once and can be re-used in other problems with little difficulty. The resolution and the number of different perforation diameters in the library depend on the choice of the finest discretization level, J . An interpolation scheme is then used to approximate \mathbf{K}_j^c as a continuous function of the design variables in the specified range of allowable values the design variables can take. To illustrate, Figure 4.7 shows the largest, intermediate and smallest perforation that can be modeled at resolutions corresponding to scales $J = 4$, $J = 5$ and $J = 6$. The spacing between nodal degrees of freedom would be the same after reduction, regardless of the starting level. Thus the choice of J only affects the offline computations and not the computations within the optimization process.

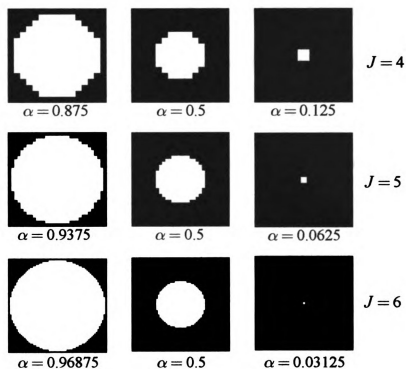


Figure 4.7: Substructures with circular perforations for various finest levels

4.2.3 Sensitivity Analysis

The sensitivity analysis using substructures with centered circular perforations is illustrated here. The analysis can be extended to substructures with other kinds of perforations easily. In the case of substructures with circular perforations, the design variable is the diameter of the perforation in a substructure given by the following relation

$$d_c = \alpha L_c, \quad 0 \leq \alpha \leq \alpha_{\max} \quad (4.6)$$

where L_c is the dimension of the substructure and α_{\max} is a prescribed bound on the size of the perforations. When the reduction of the substructures is based on an MRA of material distribution, entries in the library are pixel values of ρ_j^c , obtained using a

$(J - j)$ -level reduction of the fine-scale material distribution function $\rho_J(\alpha^{(k)})$. The pixel values $(\rho_j^c)_{kl}$ are obtained from an interpolation of the entries in the library.

The effective stiffness matrix $\mathbf{K}_j^c(\alpha)$ is then computed using these interpolated reduced material distribution functions. The gradients of the stiffness matrix with respect to the design variables is computed as

$$\frac{\partial \mathbf{K}_j^c}{\partial d_c} = \frac{1}{L_c} \frac{\partial \mathbf{K}_j^c}{\partial \alpha} = \frac{1}{L_c} \sum_{k,l=1}^n (\rho')_{k,l} \mathbf{k}^0 \quad (4.7)$$

where $\rho' = \frac{\partial \rho_j^c}{\partial \alpha}$ is computed using the interpolation function and \mathbf{k}^0 is the element stiffness matrix of a solid element (reference).

When the reduction is based on an MRA of displacements, the effective stiffness matrix $\mathbf{K}_j^c(\alpha)$ is computed by interpolation in α of the entries in the library $\{\mathbf{K}_j^c\}^{(k)}$. This interpolated function is similarly used in the computation of the gradients of the stiffness matrix with respect to the design variables,

$$\frac{\partial \mathbf{K}_j^c}{\partial d_c} = \frac{1}{L_c} \frac{\partial \mathbf{K}_j^c}{\partial \alpha} \quad (4.8)$$

where the derivative with respect to α , $\frac{\partial \mathbf{K}_j^c}{\partial \alpha}$, is computed using the interpolation function.

4.3. Compliance Minimization Problems

While the proposed procedure can be applied using any geometry of (parameterizable) perforations, here the formulation of the compliance minimization problem is illustrated for two particular cases: substructures with centered rectangular perforations and substructures with circular perforations. It is a common practice in standard topology optimization problems to consider characteristic cells with rectangular voids (see Suzuki and Kikuchi [36]). This is usually done so that fully void regions can be modeled by letting the perforation extend to the whole cell (void cells), see Figure 4.2. In the present case, the exterior boundary of the design domain is known a-priori and we are only interested in the distribution of the perforations inside this boundary. The choice of the shape of the perforation in this case may be dictated by other considerations such as ease of implementation, etc. Figure 4.8 shows two typical perforated substructures and the associated parameters.

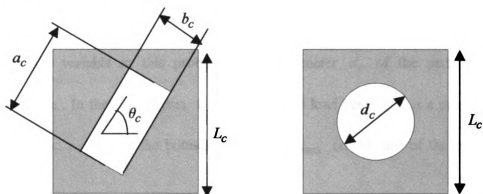


Figure 4.8: Substructures with rectangular and circular perforations

A compliance-minimization problem for a library of substructures of centered rectangular perforations can be written as follows: For each designable substructure c , find a_c, b_c, θ_c that

$$\begin{aligned}
& \text{minimize} && \mathbf{C} \doteq \mathbf{f}^T \mathbf{u} \\
& \text{subject to} && \sum_c \left(L_c^2 - a_c b_c \right) \leq \gamma \text{meas}(\Omega) \\
& && \alpha_{\min} L_c \leq a_c \cos \theta_c, b_c \cos \theta_c \leq L_c \\
& && \alpha_{\min} L_c \leq a_c \sin \theta_c, b_c \sin \theta_c \leq L_c \\
& && 0 \leq \theta_c < \pi/2 \\
& && \mathbf{K}\mathbf{u} = \mathbf{f}
\end{aligned} \tag{4.9}$$

The design variables in this case are the dimensions of the perforations and the orientation of the perforations with respect to the substructures.

Similarly, the optimization problem for a library of substructures of centered circular perforations can be expressed as follows: for each designable substructure c , find d_c that

$$\begin{aligned}
& \text{minimize} && \mathbf{C} \doteq \mathbf{f}^T \mathbf{u} \\
& \text{subject to} && \sum_c \left(L_c^2 - \pi \frac{d_c^2}{4} \right) \leq \gamma \text{meas}(\Omega) \\
& && 0 \leq d_c \leq \alpha_{\max} L_c \\
& && \mathbf{K}\mathbf{u} = \mathbf{f}
\end{aligned} \tag{4.10}$$

The design variable in this problem is the diameter d_c of the perforation in each substructure. In these problems, \mathbf{f} is a prescribed load vector, γ is a prescribed volume fraction, $0 < \gamma < 1$, and the bounds α_{\min} and α_{\max} on the size of the perforations are given data.

Compliance minimization problems (or any other problems) solved using the proposed scheme can be divided into two broad categories: fixed and variable discretization of the domain. In the problems of the first kind, the discretization of the design domain Ω into substructures is prescribed a-priori and remains unchanged throughout the optimization, i.e., only the size of the perforation in each substructure

needs to be determined. Figure 4.9 illustrates a possible starting and final layout of perforations in an optimization problem using a fixed layout of substructures.

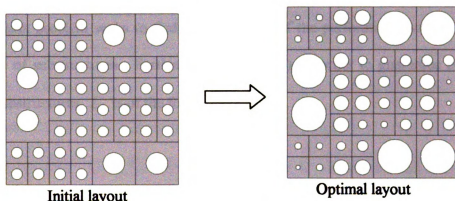


Figure 4.9: Optimization using fixed layout of substructures

In problems of the second kind, the discretization of the design domain into substructures varies at each stage of the optimization, i.e., at each step the size of each substructure and size of the perforation are determined. Figure 4.10 illustrates the optimization using variable layouts of substructures. However, in both types of problems, since (consistently) reduced substructures are used the number of degrees of freedom in the reduced model of the structure is always the same regardless of the number of substructures used or their sizes.

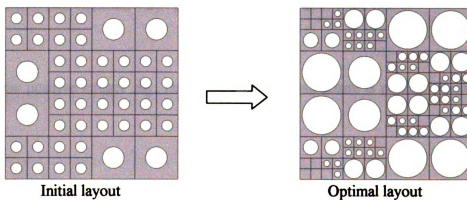


Figure 4.10: Optimization using variable layouts of substructures

1. The first step in the process of identifying a problem is to recognize that a problem exists. This is often done by comparing current performance with a desired state or goal. For example, a manager might notice that sales are declining or that customer satisfaction is low. Once a problem is identified, the next step is to define it more precisely. This involves determining the scope of the problem, its causes, and its effects. For instance, a manager might define a sales decline as a 10% drop in revenue over the last quarter, caused by a decrease in the number of new customers and a decline in repeat business. The final step in the process is to prioritize the problem. This involves assessing the importance of the problem and the urgency of addressing it. For example, a manager might prioritize a sales decline over a low level of customer satisfaction because the former is more likely to result in long-term damage to the company.

4.4 Optimization Using Fixed Layouts Of Reduced Substructures

In this type of problems the size L_c of each substructure is prescribed a-priori, i.e., the optimization problem seeks to find only the sizes of the perforations within a prescribed assembly of substructures. Furthermore, from (4.5), in order to guarantee compatibility across substructures, L_c is of the form,

$$L_c = 2^{m_c} L \quad (4.11)$$

where m_c is a non-negative integer and L is a prescribed dimension in the problem, see Figure 4.6. The exponent m_c may vary from substructure to substructure. For simplicity, it is assumed that the geometry in all the perforated substructures is resolved by a discretization of the same level, J . Thus, the fine scale at any substructure is

$$S_c = L_c / 2^J \quad (4.12)$$

i.e., the material in each substructure is modeled using $2^J \times 2^J$ (pixels) elements. In the reduced system, the degrees of freedom are spaced such that displacements are continuous across boundaries. This determines the reduction level j_c for each substructure (see equation 4.5). If the nodal spacing after reduction is

$$\Delta = L / 2^{m_0} \quad (4.13)$$

for some positive integer m_0 , then a perforated substructure is reduced from level J to level

$$j_c = m_0 + m_c \quad (4.14)$$

Clearly, m_0 must be such that for all substructures $j_c \leq J$.

A possible (fixed) layout of substructures is shown in Figure 4.11. Three sizes of substructures are used in this layout, L , $2L$ and $4L$. In order to satisfy the continuity requirements across substructure boundaries the reduction levels in the substructures are relating according to the following rule: if the substructures of size $4L$ are reduced to a level j , then the substructures of sizes $2L$ and L are reduced to levels $j-1$ and $j-2$ respectively. The lowest allowable level for any substructure is $j = 3$ when D6 scaling functions are used. Thus, the substructures of size $4L$ can be reduced at the most to a level $j = 5$ in order to satisfy the previous criterion.

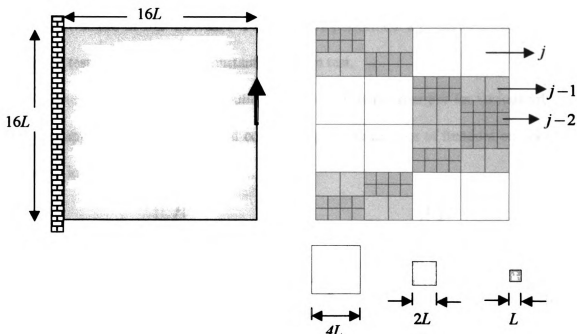


Figure 4.11: A design domain and a possible layout of reduced substructures

4.5 Optimization Using Variable Layouts Of Reduced Substructures

4.5.1 Perforated Substructures and Layout Dependency

In problems with variable layouts of substructures, one needs suitable criteria to choose between assemblies of smaller substructures and large substructures. This necessitates a comparison between the stiffness properties of a single perforated substructure with an assembly of smaller substructures keeping the total amount of material in both equal. Here, an assembly of four substructures, each of size $L \times L$, is compared with a single large substructure of size $2L \times 2L$. Two tests are performed: a prescribed traction on the boundary test and a prescribed constant pre-strain test.

The first test involves computing the resulting strain energies for various arbitrary tractions applied on three edges and constraining all the degrees of freedom on one edge, as shown in Figure 4.12.

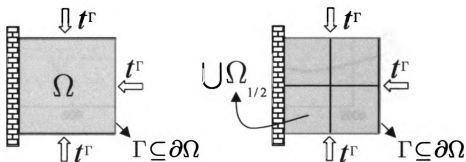


Figure 4.12: Boundary traction test

In a structure made up of several substructures subject to some prescribed loading, this test seeks to answer the question: whether removing a large substructure with a single perforation and replacing it with four small substructures (of half the size and with the amount material being the same in both) would make the structure stiffer or alternatively,

removing a patch of four small substructures and replacing them with a single large substructure makes the structure stiffer. For the same tractions, the stiffer substructure would result in a lesser deformation and hence the resulting complementary strain energy of a stiffer structure would be lesser. The random tractions are chosen arbitrarily from a uniform random distribution in $\mathbb{R}^{[0,1]}$. The resulting strain energies in each case are shown in Figure 4.13. The results show that a configuration of four substructures, of size L each, is stiffer (lesser strain energy) than a substructure of size $2L$ with a single perforation and having the same amount of material.

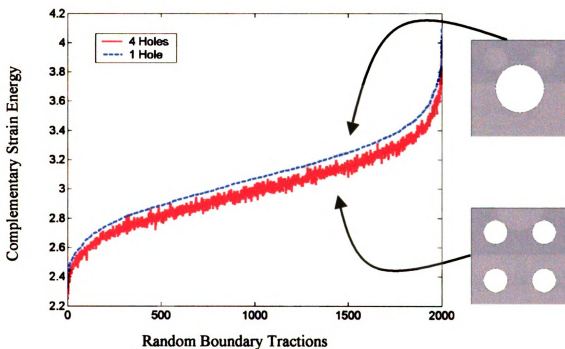


Figure 4.13: Comparison of strain energies in substructures with different number of perforations for various boundary tractions

The second test involves the application of *constant* pre-strains of the form,

$$\epsilon^0 = \begin{bmatrix} 1 & 0 \\ 0 & \eta \end{bmatrix}, \eta \in [-1, 1], \text{ (see section 3.x). For the same prescribed strain a stiffer}$$

structure would result in higher strain energy. As before, the resulting strain energy due to these pre-strains as obtained from a single substructure of size $2L$ and a patch of four substructures of size L are shown in Figure 4.14. It can be seen from the figure that the strain energy in the patch of four smaller substructures is always greater than that in the large substructure and thus conforming that the patch of four substructures of size L each is indeed stiffer than a single substructure of size $2L$ for the same amount of material in both.

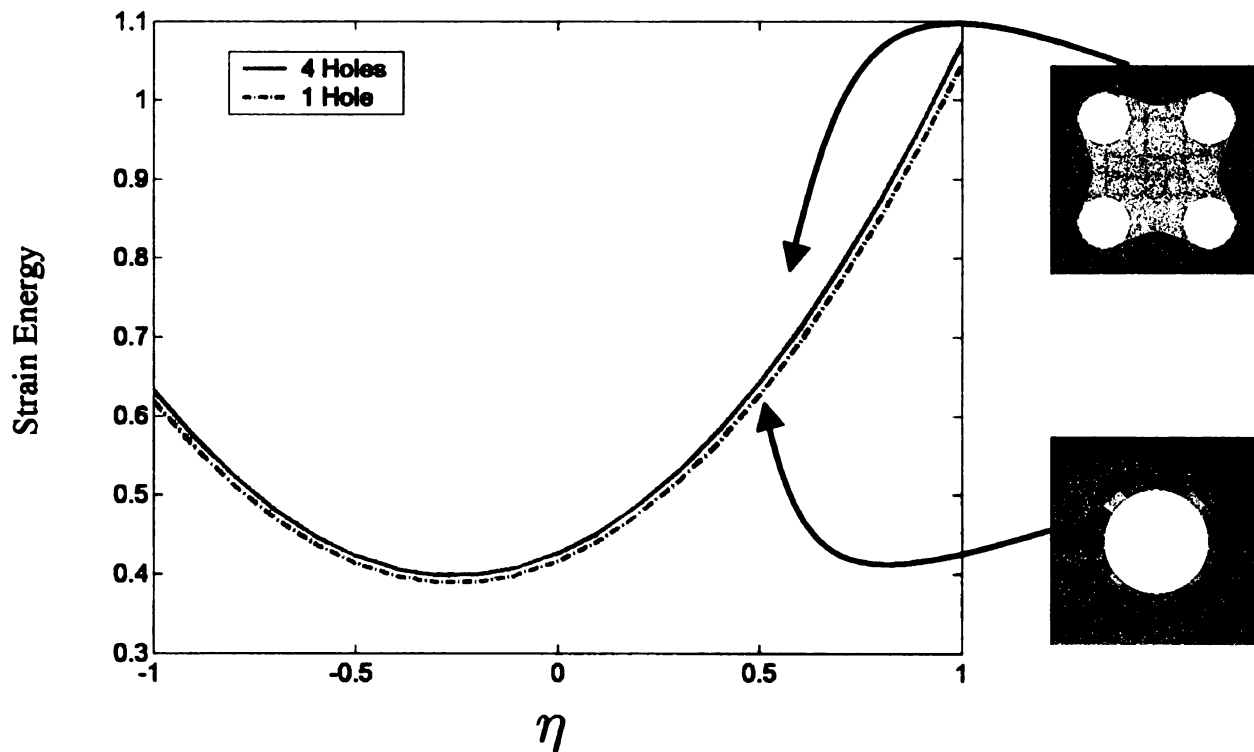


Figure 4.14: Comparison of strain energies in substructures with different number of perforations for various constant pre-strains

It should be noted that these results are local to a particular substructure, i.e., they assume that the change in the layout of a substructure does not alter the overall stress distribution in the entire structure. However, this may not be true in general. Nevertheless, this result may be used as a criterion in an updating scheme to determine

the optimal arrangement of substructures that result in the stiffest structure. This needs to be done iteratively and is discussed in the following sections.

4.5.2 A Dividing Approach to Optimization with Variable Layouts

In this approach the structure is initially built entirely using as many large substructures as possible and each update of the layout corresponds to a subdivision of a large substructure into four smaller ones. This process is illustrated in Figure 4.15.

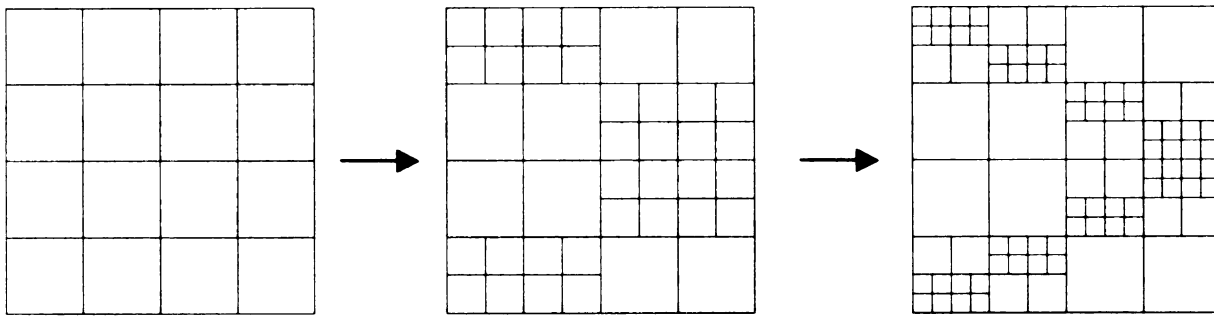


Figure 4.15: Illustration of the possible evolution of the layouts using the dividing approach

Here, additional constraints such as a bound on the total perimeter of the perforations (P_{\max}) or a limit on the number of substructures of a particular size are introduced in order to have a suitable stopping criterion for the layout updating.

This process may be summarized as follows. (Here, the method is illustrated using a bound on the perimeter of the perforations as the stopping criterion.)

(0). Start with an initial layout of substructures $\{L_c\}$, $c = 1$ to N_0 , with perforations of suitable sizes such that the volume constraint is satisfied, e.g.,

$$d_c = 2L_c \sqrt{\frac{1-\gamma}{\pi}}$$

where d_c is the diameter of a perforation, γ is a prescribed volume fraction and L_c is the size of a substructure.

(1). Solve a fixed-layout optimization problem (4.10), i.e., for $c = 1$ to N_0 , find optimal

$$d_c$$

(2). Sort the substructures according to *decreasing* order of magnitude of strain energy in each, such that

$$\mathbf{u}_i^T \mathbf{K}^i \mathbf{u}_i \geq \mathbf{u}_j^T \mathbf{K}^j \mathbf{u}_j, \text{ if } i < j$$

where, i and j are two substructures in the sorted list whose corresponding stiffness matrices are \mathbf{K}^i and \mathbf{K}^j with displacements \mathbf{u}_i and \mathbf{u}_j

$$\text{Set } N = N_0 \text{ and } P = \sum_c \pi d_c$$

(3). For each substructure c in the sorted list, $c = 1$ to N_0

If the perforation is of a *significant size* and the perimeter constraint is not violated upon subdivision, divide the substructure into four smaller substructures with perforations of half the size of the original perforation. Each such division increases the total perimeter of the perforations by πd and the number of substructures by 3. The requirement that the perforation be of significant size is because the division of solid (or almost solid) substructures does not improve performance.

```

    Let  $D = d_c$  and Let  $L = L_c$ 
  ( if  $D > \alpha_{\min} L$ 
    ( if  $(P + \pi D) \leq P_{\max}$ 
       $d_c = d_{N+1} = d_{N+2} = d_{N+3} = \frac{D}{2}$ 
       $L_c = L_{N+1} = L_{N+2} = L_{N+3} = \frac{L}{2}$ 
       $N = N + 3$ 
       $P = P + \pi D$ 
    ) endif
  ) endif

```

where α_{\min} is a suitably chosen minimum (relative) size of a perforation (e.g., 0.05).

Else, go to step 4 (break loop).

- (4). Solve a fixed-layout optimization problem (4.10) to determine the optimal sizes of perforations, i.e., d_c , $c = 1$ to N (where, $N > N_0$)

The resulting layout may be used again as a starting layout and the entire process is repeated recursively till the stopping criterion is met, i.e., any further division results in a violation of the perimeter constraint.

A method that directly follows from the reverse idea of this approach is discussed next.

4.5.3 A Merging Approach to Optimization with Variable Layouts

In this approach, the starting layout consists of purely small substructures and each update of the layout corresponds to merging four small substructures to create a bigger substructure. This is illustrated in Figure 4.16.

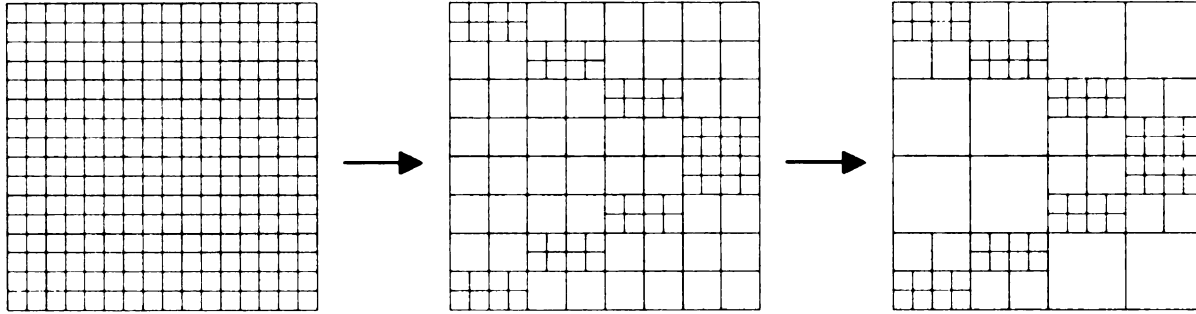


Figure 4.16 Illustration of the possible evolution of the layouts using the merging approach

This approach is more flexible in terms of feasible starting layouts. In the previous approach, there is only one way to divide a substructure into four equal smaller substructures. However, in this approach, each substructure may have up to four ways of merging with neighboring substructures to make up a large substructure. Thus, the number of possible layouts of substructures in this approach is a lot more than that using the earlier approach.

This approach may be summarized as follows. (As before, the method is illustrated using a bound on the perimeter as the stopping criterion.)

- (0). Start with a layout of small substructures $\{L_c\}$, $c = 1$ to N_0 , with perforations such that the volume constraint is satisfied, e.g.,

$$d_c = 2L_c \sqrt{\frac{1-\gamma}{\pi}}$$

where d_c is the diameter of a perforation, γ is a prescribed volume fraction and L_c is the size of a substructure.

- (1). Solve a fixed-layout optimization problem (4.10), to find the optimal d_c for $c = 1$ to N_0

(2). Group neighboring substructures (of the same size)[§] as possible candidates to be merged. A substructure can be a part of up to four groups depending on whether it is located in an edge or in the interior of the domain. Create a table \mathbf{G} , of dimensions $N_G \times 4$, that consists of all possible groups of four neighboring substructures, where N_G is the number of groups.

(3). Sort the groups according to *increasing* magnitude of total strain energy of the substructures in the groups

$$\text{Set } P = \sum_c \pi d_c \text{ and } N = N_0$$

(4). For each group in the sorted table, $g = 1$ to N_G , if the total perimeter exceeds the allowable limit and if the maximum deviation of the perforation size from the mean is within a prescribed bound (and the perforations are of significant size), merge the four substructures in the group, i.e.,

$$\left(\begin{array}{l} \text{if } P > P_{\max} \\ \quad \{d\}^g = \{d_i, d_j, d_k, d_l\} \\ \\ \quad \left(\text{if } \text{mean}(\{d\}^g) > \alpha_{\min} L_g \text{ and } \left(\frac{\max(\{d\}^g)}{\text{mean}(\{d\}^g)} - 1 \right) < \delta \right. \\ \\ \quad \quad D = \sqrt{(d_i^2 + d_j^2 + d_k^2 + d_l^2)} \\ \quad \quad P = P - \pi((d_i + d_j + d_k + d_l) - D) \\ \quad \quad N = N - 3 \\ \quad \quad \text{endif} \\ \text{endif} \end{array} \right.$$

[§] relevant for recursive restarts

where, $\{i, j, k, l\}$ is any group in G , α_{\min} is a prescribed bound on the minimum relative size of perforations, L_g is the size of the substructures in the group, δ is a prescribed bound on the maximum deviation of the perforation sizes allowable in a group to be merged, e.g., 30% and D is the new size of the merged perforation. Each such merging reduces the number of substructures by 3 and the reduction in the perimeter depends on the size of the perforations merged.

(5). Solve a fixed-layout optimization problem (4.10), to find the optimal d_c , for $c = 1$ to N . Here, $N < N_0$.

These steps are repeated recursively till the stopping criterion is met, i.e., the perimeter satisfies the prescribed bound.

As before, the sorting of the groups and the formation of the groups themselves must take into account the significance of the perforation sizes in the substructures to be grouped in order to avoid unnecessarily merging solid substructures. In the previous approach the sizes of the updated perforations are exactly half the size of the original perforation in a substructure. In this approach, the occurrence of a group of four neighboring perforations of the same size cannot be expected in general. It should be noted that in this approach the starting layout has a large initial value of total perimeter of perforations and this keeps reducing as the optimization progresses. This is in contrast to the previous approach where the perimeter is initially less than the allowable value and keeps increasing as the optimization progresses. Also, an important difference in the two approaches is that the division is performed on substructures in the decreasing order of strain energy and the merging is done on groups of substructures in the increasing order of strain energy. In these methods, the main idea behind the changing of the layouts is

the knowledge that a perforated substructure of size $2L$ with perforation diameter $2d$ is weaker than a patch of four substructures of size L each with a perforation diameter d . Thus, at locations of high strain energy, it is better to have smaller substructures than large ones. This also explains the use of the bound on the maximum deviation of the size of the perforations in a group to be merged, since the criterion results from comparing a patch of substructures with the same size perforations with a large substructure with a perforation of double the size of the small perforations. The same criterion cannot be used when comparing a patch of substructures with very different sizes of perforations in each with an equivalent larger substructure with the same amount of material and so merging of substructures with very different perforation sizes are avoided by prescribing a bound on the maximum deviation on the perforation size in a group to be merged.

4.6. Examples

Some numerical examples that illustrate the proposed optimization schemes for the compliance minimization problem are presented in this section. Here the schemes are illustrated using substructures with circular perforations. In all the examples shown, the solid material has a Young's modulus of 0.91 and the weak material (void) has a Young's modulus of 0.045 and the Poisson's ratio is 0.3 in both.

4.6.1. Example 1

The first example considered is a simple rectangular design domain that is clamped at the sides and two loads are applied at the centers of the top and bottom edges as shown in Figure 4.17.

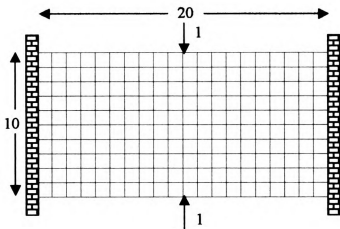


Figure 4.17: Problem description for example 1

The fixed layout of substructures is also shown in the above figure. The domain is modeled using 200 substructures of equal size, as shown. The allowable volume fraction of solid material is 0.6. The optimal layout obtained is shown in Figure 4.18. The compliance of the structure with uniform sized perforations is 35.2. The compliance of the optimal layout obtained is 25.2.

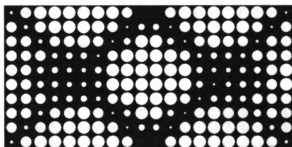
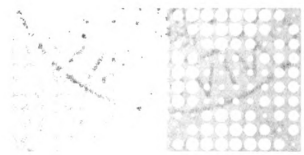


Figure 4.18: Optimal layout for example 1

The first part of the paper discusses the importance of the research and the objectives of the study. It highlights the need for a comprehensive understanding of the subject matter and the role of the researcher in this process. The second part of the paper focuses on the methodology used in the study, detailing the data collection methods and the analysis techniques employed. The third part of the paper presents the results of the study, discussing the findings and their implications. The final part of the paper concludes the study, summarizing the key points and providing recommendations for future research.



4.6.2. Example 2

This example illustrates the effect of multiple load cases. The design domain is a rectangle pinned at the bottom corners with three loads at the bottom edge applied one at a time as shown in Figure 4.19.

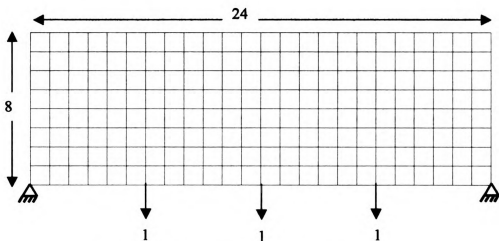


Figure 4.19: Problem description for example 2

The domain is modeled using 192 substructures of uniform size as shown. The volume fraction of the solid material allowed is 0.6. The optimal layout obtained using multiple load cases with the objective function being the mean compliance of the three load cases is shown in Figure 4.20. The compliance of the optimal layout is 53.8.

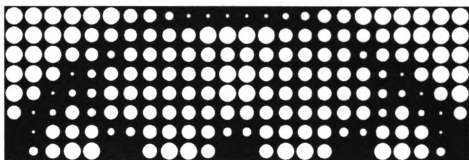


Figure 4.20: Optimal layout using multiple load cases for example 2

1. The first part of the document discusses the importance of maintaining accurate records of all transactions. This is essential for ensuring the integrity of the financial statements and for providing a clear audit trail.

2. The second part of the document outlines the various methods used to collect and analyze data. These methods include direct observation, interviews, and the use of specialized software tools.

3. The third part of the document describes the results of the data collection and analysis. It shows that there are significant differences in the way that different departments handle their data, and that these differences can lead to errors and inconsistencies.

4. The fourth part of the document discusses the implications of these findings and provides recommendations for how to improve the data collection and analysis process.

The following table shows the results of the data collection and analysis for the different departments.

Department	Method	Results
Sales	Direct Observation	High accuracy, but time-consuming.
	Interviews	Good for understanding context, but prone to bias.
Marketing	Direct Observation	Low accuracy, but easy to implement.
	Interviews	Good for understanding context, but prone to bias.
Finance	Direct Observation	High accuracy, but time-consuming.
	Interviews	Good for understanding context, but prone to bias.
Operations	Direct Observation	High accuracy, but time-consuming.
	Interviews	Good for understanding context, but prone to bias.

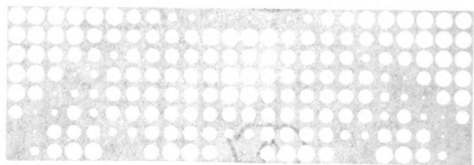


Figure 4.21 shows the optimal layout obtained when all the three loads are applied simultaneously. It can be seen that this layout is quite different from the previous layout.

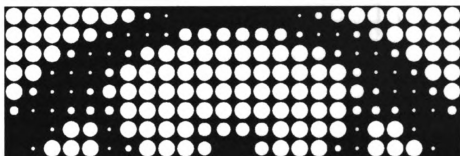


Figure 4.21: Optimal layout using single load case for example 2

4.6.3. Example 3

The third example is an L-shaped domain with the bottom edge clamped and a unit tip load applied on the center of the right edge. This domain is modeled using a uniform layout of 192 substructures of equal size as shown in Figure 4.22 and using an arbitrary layout with two sizes of substructures defined as shown in Figure 4.23.

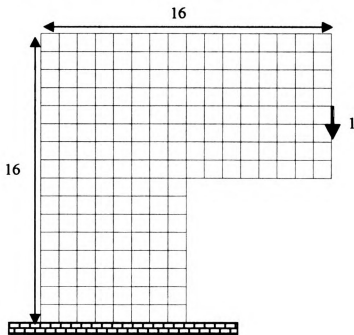


Figure 4.22: Problem description with uniform layout for example 3

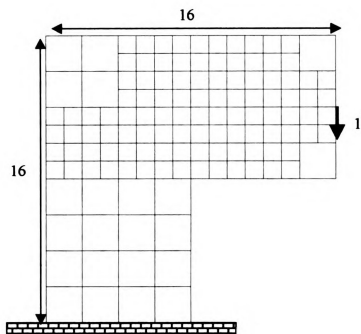


Figure 4.23: Problem description with multi-size layout for example 3

The optimal layout obtained using the uniform layout is shown in Figure 4.24 and that obtained from the layout with multi-size substructures is shown in Figure 4.25.



Figure 4.24: Optimal layout using single-size substructures for example 3



Figure 4.25: Layout using multi-size substructures for example 3

The compliance of the layout with uniform size substructures is 82.8 and the compliance of the layout with substructures of two different sizes is 86.3. Clearly, this arrangement of substructures of two sizes is not the optimal arrangement. However, such layouts involving larger substructures are necessary when additional constraints such as those on the total perimeter of perforations in the structure are prescribed. The arrangement of layouts involving multiple size substructures needs to be done iteratively and is the subject of discussion in the following examples.

The examples presented so far require the layout of substructures to be prescribed a-priori and that it remains unchanged throughout the optimization. The next two examples illustrate the proposed schemes for optimization using variable layouts of substructures.

4.6.4. Example 4

This example is the well-known short cantilever beam problem (see Bendsøe et al [4]). The standard topology optimization solution to this problem is shown in Figure 4.2. The design domain is a rectangle that is clamped at the left edge and a tip load at the right edge as shown in Figure 4.26. The volume fraction prescribed is 0.7. The layout of substructures is not prescribed but rather it is part of the problem.

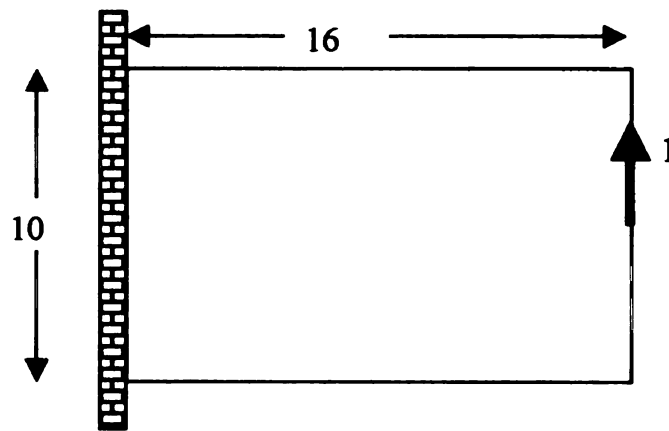


Figure 4.26: Problem description for example 4

This problem is solved using the two proposed approaches for problems with variable layouts of substructures, i.e., dividing approach and merging approach. Substructures of two sizes, L and $2L$ are used in the layout optimization. A perimeter constraint $P_{\max} = 207.3$ is prescribed, which is the average of the perimeters of the optimal layouts of perforations when uniform discretization of the domain using of substructures of size L and $2L$ are used.



Dividing Approach

The starting layout of substructures for the dividing approach (a uniform layout of substructures of size $2L$) and the optimal layout of perforations for this arrangement of substructures are shown in Figure 4.27. The compliance associated with this layout is 37.4. The total perimeter of the perforations is 138.2.

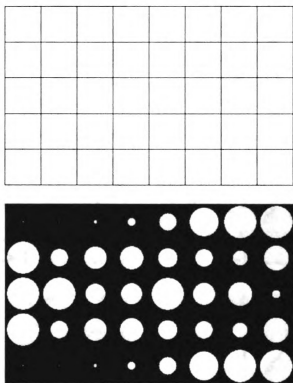
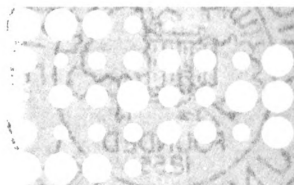


Figure 4.27: Starting arrangement of substructures for optimization using the dividing approach for example 4 and the corresponding optimal layout of perforations

Figure 4.28 shows the sequence of steps in the dividing approach. According to the algorithm described in section 3.5.2, the substructures shown in figure 4.27 are sorted according to the strain energy and are divided in sequence till the total perimeter of the perforations reaches the prescribed limit.



1. The first step is to identify the key elements of the problem. This involves understanding the context, the goal, and the constraints. It is important to ask questions and gather information to fully understand the problem.

2. Next, you should break the problem down into smaller, more manageable parts. This allows you to focus on one aspect at a time and makes it easier to find a solution.

3. Once you have identified the key elements and broken the problem down, you can start to brainstorm potential solutions. This is a creative process and often involves thinking outside the box.

4. After you have brainstormed potential solutions, you should evaluate each one. Consider the pros and cons of each solution and how well it addresses the problem.

5. Finally, you should choose the best solution and implement it. This may involve making adjustments or refining the solution as you go along.

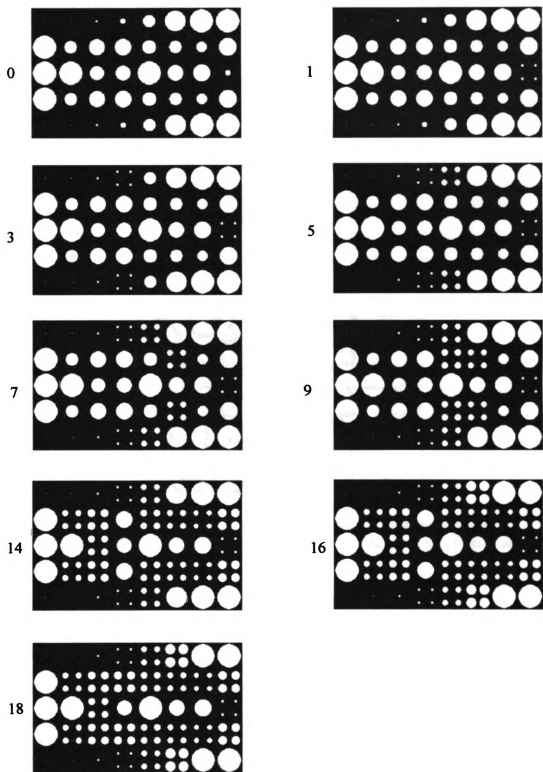


Figure 4.28: Sequence of steps in the dividing approach for example 4

THE UNIVERSITY OF CHICAGO

THE UNIVERSITY OF CHICAGO PRESS

50 EAST LAKE STREET, CHICAGO, ILLINOIS 60607

TEL: 773/936-3400 FAX: 773/936-4700

WWW.UCHICAGO.PRESS.COM

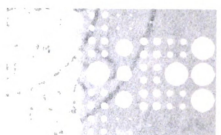
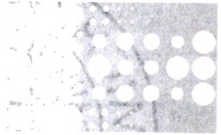
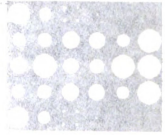
THE UNIVERSITY OF CHICAGO

THE UNIVERSITY OF CHICAGO PRESS

50 EAST LAKE STREET, CHICAGO, ILLINOIS 60607

TEL: 773/936-3400 FAX: 773/936-4700

WWW.UCHICAGO.PRESS.COM



The layout of substructures after successive divisions (step 18) and the optimal structure with this as a fixed layout are shown in Figure 4.29. The compliance of this structure is 34.2 and the perimeter is 201.8.

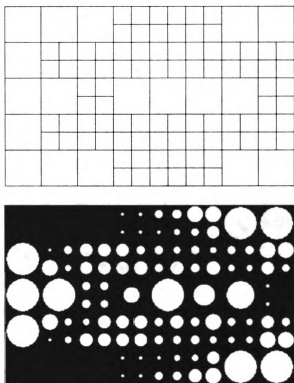


Figure 4.29: Optimal arrangement of substructures using the dividing approach for example 4 and the corresponding optimal layout of perforations

Merging Approach

The starting layout of substructures (a uniform layout of substructures of size L) and the optimal structure using this initial layout are shown in Figure 4.30. The compliance of this structure is 34.5 and the perimeter of the perforations is 276.5. Notice that the compliance of this structure is already very close to that of the optimal structure using the dividing approach. However, the perimeter of the perforations is much larger than the prescribed limit.

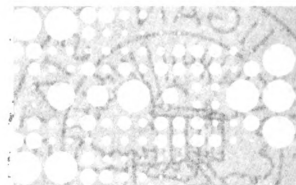


Fig. 1. Scanning electron micrograph of the polymer matrix.

the polymer matrix, and the particles are randomly distributed.

The morphology of the polymer matrix is shown in Figure 1.

The morphology of the polymer matrix is shown in Figure 1.

The morphology of the polymer matrix is shown in Figure 1.

The morphology of the polymer matrix is shown in Figure 1.

The morphology of the polymer matrix is shown in Figure 1.

The morphology of the polymer matrix is shown in Figure 1.

The morphology of the polymer matrix is shown in Figure 1.

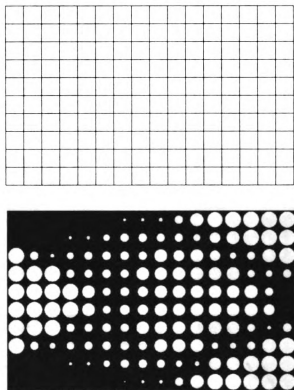


Figure 4.30: Starting arrangement of substructures using the merging approach for example 4 and the corresponding optimal layout of perforations

Figure 4.31 shows the sequence of steps in the merging approach starting from the optimal structure obtained using the initial layout. As described in section 3.5.3, the substructures in figure 4.30 are first arranged into a list of possible candidates for merging in an increasing order of total strain energy. Then, the groups in the list are sequentially merged till the total perimeter of the perforations falls below the allowable limit.



THE UNIVERSITY OF CHICAGO
DIVISION OF THE PHYSICAL SCIENCES
DEPARTMENT OF CHEMISTRY
5708 SOUTH CAMPUS DRIVE
CHICAGO, ILLINOIS 60637

RECEIVED
JAN 15 1964
BY
LIBRARY OF THE UNIVERSITY OF CHICAGO
DIVISION OF THE PHYSICAL SCIENCES
DEPARTMENT OF CHEMISTRY
5708 SOUTH CAMPUS DRIVE
CHICAGO, ILLINOIS 60637

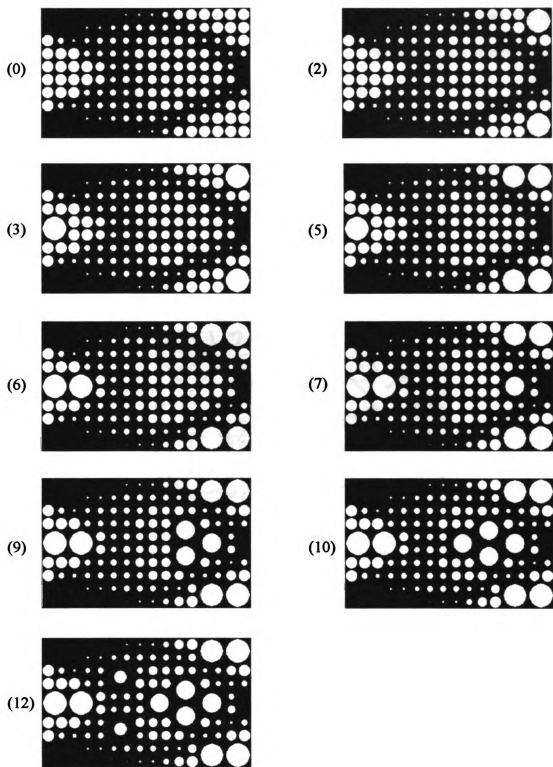


Figure 4.31: Sequence of steps in the merging approach for example 4

The final layout of substructures obtained after successive merging and the optimal structure using this layout are shown in Figure 4.32. The compliance of this structure is 33.6 and the total perimeter of the perforations is 207.1.

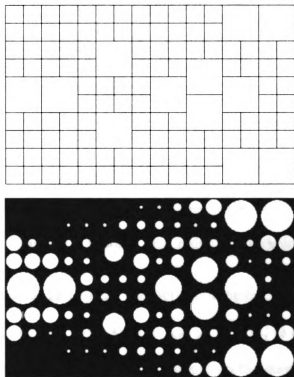


Figure 4.32: Optimal arrangement of substructures using the merging approach and the corresponding optimal layout of perforations for example 4

The optimal structure obtained using the merging approach is stiffer than that obtained using the dividing approach. However, the perimeter in the optimal layout using the merging approach is slightly higher than the dividing approach, although both satisfy the constraint on the perimeter.

4.7.5. Example 5

The last example is a slight variation of the classical MBB beam problem (see Duysinx and Bendsøe [16]). Here the design domain is a slender simply supported rectangle with a uniform unit load on the top edge as shown in Figure 4.33.

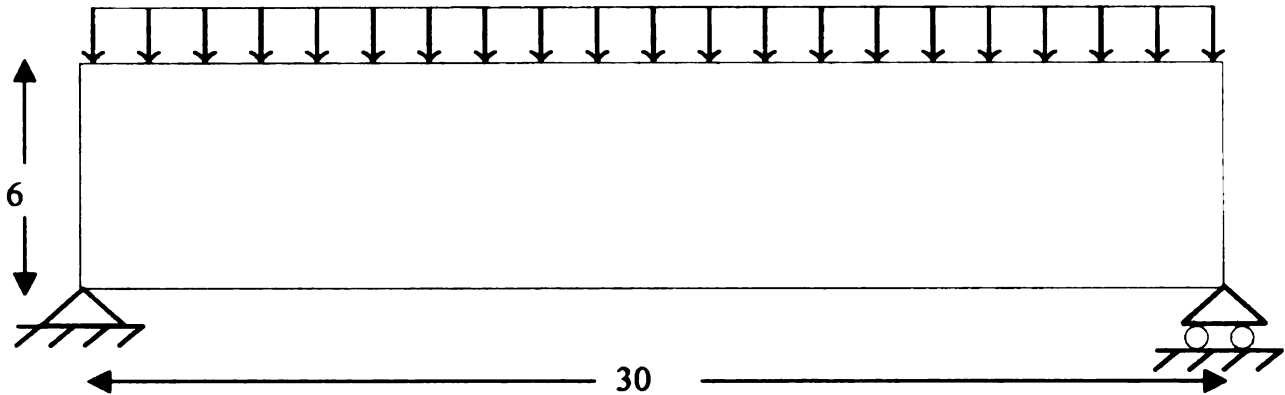


Figure 4.33: Problem description for example 5

As before, this problem seeks to build the optimal structure in the given design space using perforated substructures of two sizes L and $2L$. Here, to illustrate other possible stopping criteria for the layout updating, a constraint on the number of substructures of size $2L$ is prescribed as 11. This is used as the stopping criterion in the merging and the dividing approaches to determine the optimal arrangement of substructures.

Merging Approach

The initial layout of substructures for the merging approach and the optimal structure using this layout are shown in Figure 4.34. The compliance of the structure is 25.6. The total perimeter of the perforations is 325.



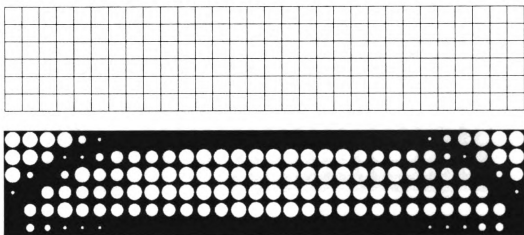


Figure 4.34: Initial layout for the merging approach and optimal structure using this layout for example 5

A sequence of layouts obtained using the merging approach is shown in Figure 4.35. The arrangement of substructures after successive merging and the corresponding optimal structure using that layout is shown in Figure 4.36. The compliance of that structure is 25.4. The total perimeter of the perforations is 250. Although this perimeter is not used at this point to determine the termination of the merging process, it is used later to compare the optimal structures obtained using the dividing approach with two possible termination criteria, i.e., number of substructures and total perimeter.

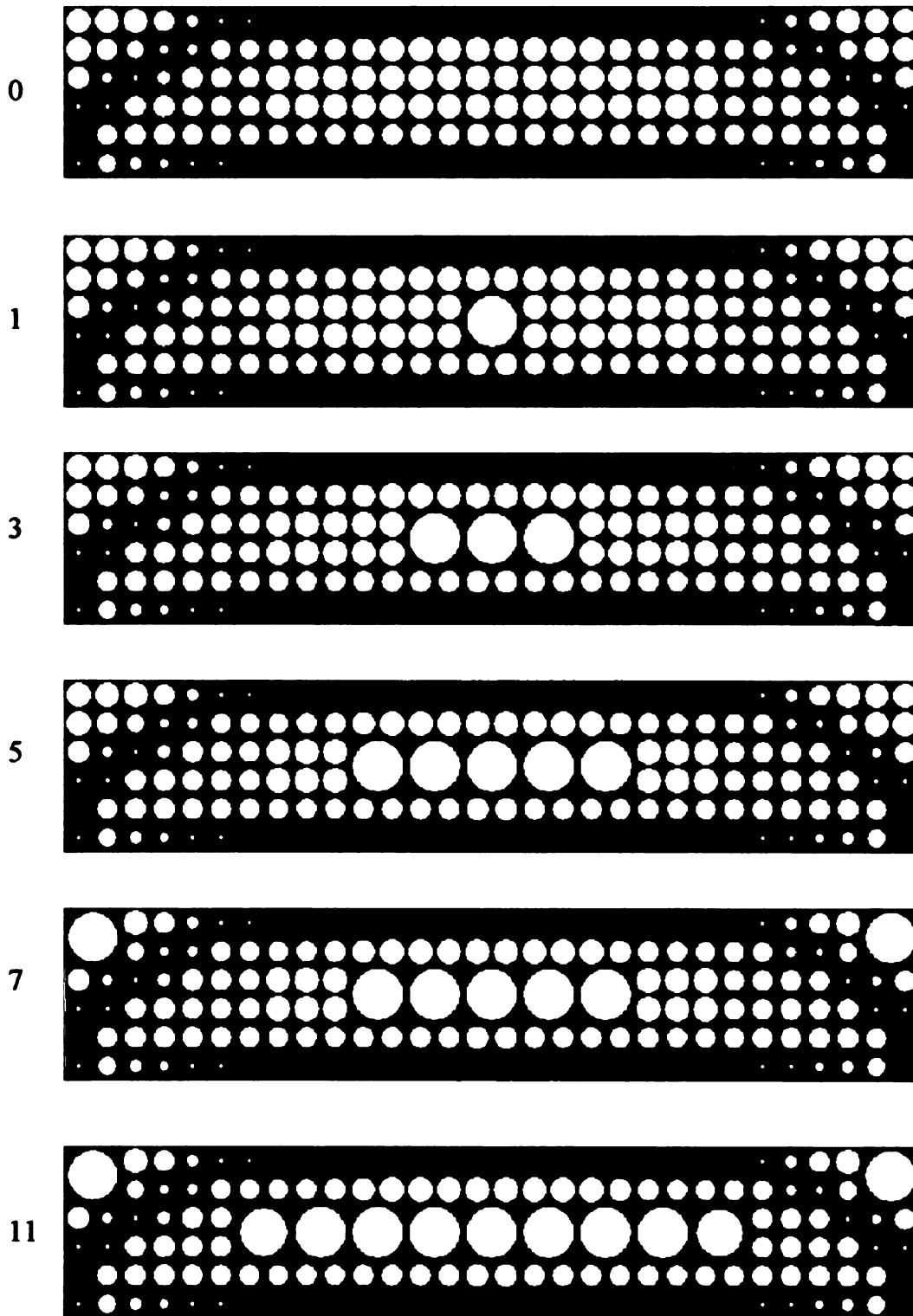


Figure 4.35: Sequence of layouts obtained using the merging approach for example 5



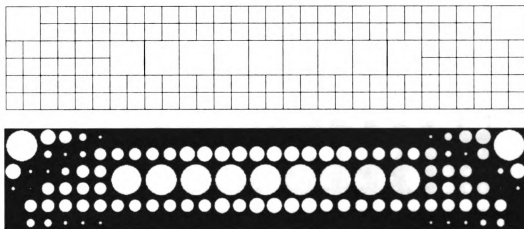


Figure 4.36: Optimal arrangement of substructures and the corresponding optimal structure obtained using the merging approach for example 5

Dividing Approach

The starting layout for the dividing approach and the optimal structure for this layout are shown in Figure 4.37. The compliance of this structure is 29.9 and the total perimeter of the perforations is 177.

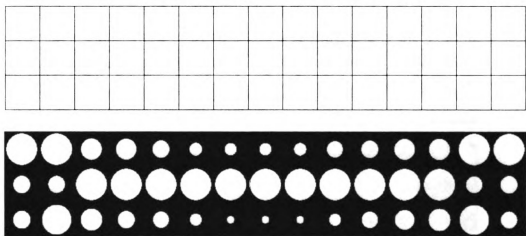


Figure 4.37: Starting layout of substructures for the dividing approach and the corresponding optimal structure for example 5



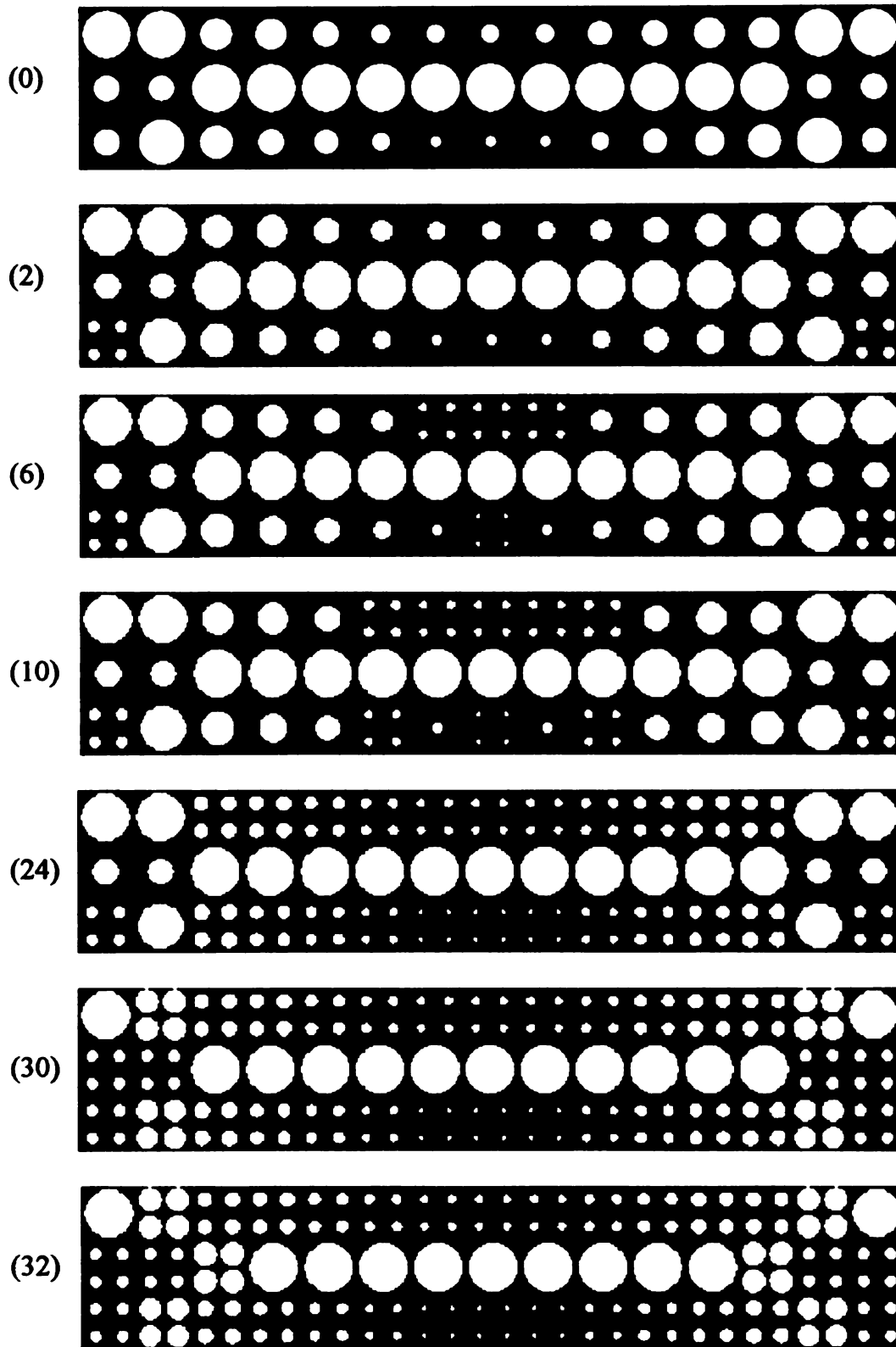


Figure 4.38: Sequence of layouts obtained using the dividing approach for example 5

A sequence of steps using the dividing approach is shown in Figure 4.38. The dividing process continues till the number of substructures of size $2L$ becomes equal to the prescribed value of 11. The final layout in Figure 4.39 is then used as the starting guess for a fixed-layout optimization problem. The layout of substructures and the corresponding optimal structure are shown in Figure 4.40. The compliance of this structure is 25.3.

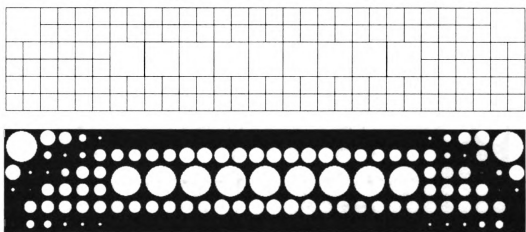


Figure 4.39: Optimal arrangement of substructures and the corresponding optimal structure obtained using the dividing approach with prescribed number of substructures of size $2L$ for example 5

It can be seen that the optimal layout of substructures and hence the optimal structure obtained using the dividing approach when the number of substructures of size $2L$ are prescribed is the same as that obtained using the merging approach.

However, if instead of the constraint on the number of substructures, a constraint on the perimeter of the perforations ($P_{\max} = 250$) is used as the termination criterion in the dividing approach, the dividing process terminates at step 24 shown in Figure 4.39. (The perimeter constraint prescribed is total perimeter of the optimal structure obtained using

1948

1949

1950

1951

1952

1953

1954

the merging approach.) The number of substructures of size $2L$ in this layout is 17. This layout is then used in a fixed-layout optimization problem to determine the optimal structure for this arrangement of substructures. The arrangement of substructures and the corresponding optimal structure is shown in Figure 4.40. The compliance of this structure is 25.7. This is higher than the previously obtained optimal layout using the constraint on the number of substructures of size $2L$.

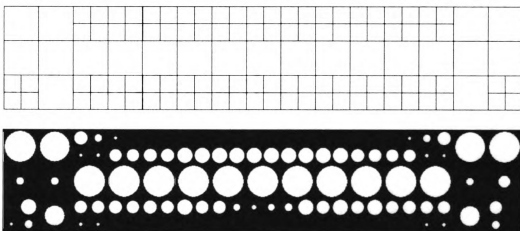


Figure 4.40: Layout of substructures and corresponding optimal structure obtained using the dividing approach with a perimeter constraint for example 5



Chapter 5

Concluding Remarks

5.1 Summary

An approach for the analysis of structural systems in linear elasticity using an assembly of consistently reduced substructures (smaller components) was presented. Two strategies for constructing reduced models were introduced: one based on a multi-resolution analysis of material distributions and the other based on a multi-resolution analysis of displacements. For relatively simple geometries, it was seen that the two methods produce results that are not too different in the coarse-scale. However, using an augmentation procedure it was shown that some parameters such as stresses could be computed more accurately at certain desired locations in the case of the approach using a multi-resolution analysis of displacements.

The concept of structural analysis using reduced models was then applied to the problem of layout optimization of structures in which finite size heterogeneities of multiple scales could be accounted. This involved constructing libraries of reduced substructures with suitable heterogeneities (illustrated using perforations here) of various sizes. The dependency of the optimal layout on the arrangement of substructures was discussed. Two approaches for optimization of layouts with finite size heterogeneities were indicated: one using fixed discretization of the design domain into substructures and the second in which the arrangement of the substructures was part of the problem.

5.2 Conclusions

- The concept of analysis of large structures using assemblies of reduced substructures proved very convenient and successful in problems such as layout optimization of structures.
- A particular advantage is derived from the fact that the reduction of a given substructure needs to be performed only once but the results are reusable. This facilitates the construction of libraries of pre-computed reduced stiffness matrices to be used as needed.
- The use of reduced substructures of different sizes and reduction levels accomplishes the goal of accounting for heterogeneities of different sizes and scales.
- As the large-scale parameters, such as compliance, are almost the same when computed using either of the two reduction schemes the computationally

expensive MRA of displacements need only be used in cases where certain small-scale parameters such as local stresses are required.

- Finally, It has to be acknowledged that many serious issues need to be addressed before this strategy can be useful in problems such as those arising in crashworthiness design, such as: how to deal with dynamic behavior? – splitting of \ddot{u} into coarse-scale and details – how to accommodate nonlinear material behavior and non-linearity associated with large deformations?

5.3 Areas of Future Work

- An immediate extension of the model reduction scheme presented is to incorporate harmonic loading. This involves the computation of a reduced mass matrix as well as a reduced stiffness matrix. This is of interest in the design of wave-guides and in acoustics.
- Similarly, a direct extension of the presented layout optimization scheme is the problem of optimal arrangement of beadings or corrugations on plates for improved dynamics properties such as natural frequencies.
- An approach to suitably combine the dividing and merging approaches in the optimization using variable layouts of substructures.
- Extension of the proposed schemes for three-dimensional problems in elasticity.
- Incorporation of transient dynamics, non-linearity arising from material properties as well as from large displacements.

BIBLIOGRAPHY

Bibliography

- [1] N.S. Bakhvalov and A.V. Knyazev, *Fictitious domain methods and computations of homogenized properties of composites with a periodic structure of essentially different components*, in G.I. Marchuk (editor), *Numerical Methods and Applications*, CRC Press, Boca Raton, FL, (1994), 221-266
- [2] M.P. Bendsøe and N. Kikuchi, *Generating optimal topologies in structural design using a homogenization method*, *Computer Methods in Applied Mechanics and Engineering*, 71 (1988) 197-224.
- [3] M.P. Bendsøe, *Optimal shape design as a material distribution problem*, *Structural Optimization*, 1 (1989), 193-202.
- [4] M.P. Bendsøe, A.R. Diaz and N. Kikuchi, *Topology and generalized layout optimization of elastic structures*, in *Topology design of structures*, edited by M.P. Bendsøe and C.A. Mota Soares, Kluwer Academic Publishers, (1993), 159-205.
- [5] A. Bensoussan, J.L. Lions and G. Papanicolaou, *Asymptotic analysis for periodic structures*, North-Holland, (1978).
- [6] G. Beylkin and N. Coult, *A multi-resolution strategy for reduction of elliptic PDEs and eigenvalue problems*, *Applied and Computational Harmonic Analysis*, 5, (1998), 129-155.
- [7] M. Brewster and G. Beylkin, *A multi-resolution strategy for numerical homogenization*, *Applied and Computational Harmonic Analysis*, 2 (1995), 327-349
- [8] R.R. Craig and M.C.C. Bampton, *Coupling of substructures for dynamic analyses*, *AIAA Journal*, 6 (7), (1968), 1313-1319.
- [9] W. Dahmen and C.A. Micchelli, *Using the refinement equation for evaluating integrals of wavelets*, *SIAM Journal of Numerical Analysis*, 30, (1993), 507-537
- [10] I. Daubechies, *Ten Lectures On Wavelets*, CBMS-NSF Series in Applied Mathematics, 61, SIAM, Philadelphia, 1992.
- [11] G.C.A. DeRose, Jr. and A.R. Diaz, *Single scale wavelet approximations in layout optimization*, *Structural Optimization*, 18 (1999), 1-11.

- [12] A.R. Díaz and M.P. Bendsøe, *Shape optimization of structures for multiple loading conditions using a homogenization method*, Structural Optimization, 4 (1992), 17-22
- [13] A.R. Díaz and N. Kikuchi, *Solutions to shape and topology eigenvalue optimization problems using a homogenization method*, International Journal of Numerical Methods in Engineering, 35, (1992), 1487-1502
- [14] A.R. Díaz, *A wavelet-Galerkin scheme for analysis of large scale problems on simple domains*, International Journal of Numerical Methods in Engineering, 44, (1999), 1599-1616
- [15] M. Dorabantu and B. Engquist, *Wavelet-based numerical homogenization*, SIAM Journal of Numerical Analysis, 35 (1998), 540-559
- [16] P. Duysinx and M.P. Bendsøe, *Topology optimization of continuum structures with local stress constraints*, International Journal of Numerical Methods in Engineering, 43, (1998), 1453-1478
- [17] B. Engquist and O. Runborg, *Wavelet-based numerical homogenization with applications*, In T.J. Barth, T.F. Chan and R. Haimes, editors, Multi-scale and Multi-resolution Methods: Theory and Applications, 97-148, Vol. 20, Lecture Notes in Computational Science and Engineering, Heidelberg 2001, Springer-Verlag.
- [18] M. Frazier, *An introduction to wavelets through linear algebra*, Springer-Verlag, New York, (1999).
- [19] M.I. Friswell, S.D. Garvey and J.E.T. Penny, *Model reduction using dynamic and iterated IRS techniques*, Journal of Sound and Vibration, 186 (2), (1995), 311-323
- [20] A.C. Gilbert, *A comparison of multi-resolution and classical one-dimensional homogenization schemes*, Applied and Computational Harmonic Analysis. 5 (1998), 1-35
- [21] R. Glowinski, T.W. Pan, R.O. Wells and X. Zhou, *Wavelet and finite element solutions for the Neumann problem using fictitious domains*, Journal of Computational Physics, 126, (1996), 40-51
- [22] R.J. Guyan, *Reduction of stiffness and mass matrices*, AIAA Journal, 3 (2), (1965), 380.
- [23] R.B. Haber, C.S. Jog and M.P. Bendsøe, *A new approach to variable topology shape design using a constraint on perimeter*, Structural Optimization, 11, (1996), 1-12
- [24] W.C. Hurty, *Dynamic analysis of structural systems using component modes*, AIAA Journal, 3 (4), (1965), 678-685.

- [25] R.V. Kohn and G. Strang, *Optimal design and relaxation of variational problems*, Communications in Pure and Applied Mathematics, 39, (1986), 113-137 (part I), 139-182 (part II), 353-377 (part III)
- [26] A. Kunoth, *Computing refinable integrals*, Technical report ISC-95-02-MATH (1995), Institute for Scientific Computation, Texas A&M University, College Station, Texas, USA.
- [27] A. Latto, H.L. Resnikoff and E. Tenebaum, *The evaluation of connection coefficients of compactly supported wavelets*, in Y. Maday (editor), Proceedings of French-USA Workshop on Wavelets and Turbulence, Princeton University, Springer, New York, (1992).
- [28] S.G. Mallat, *A theory for multi-resolution signal decomposition: The wavelet representation*, Communications in Pure and Applied Mathematics, 41 (7), 674-693 (1988).
- [29] F. Murat and L. Tartar, *Optimality conditions and homogenization*, in A. Marino et al (editors), Nonlinear Variational Problems, Pitman Advanced Publishing Program, Boston, (1995), 1-8
- [30] S. Pecullan, L.V. Gibiansky and S. Torquato, *Scale Effects on the elastic behavior of periodic and hierarchical two-dimensional composites*, Journal of the Mechanics and Physics of Solids, 47 (1999), 1509-1542.
- [31] P. Pedersen, *On optimal orientation of orthotropic materials*, Structural Optimization, 1, (1989), 101-106
- [32] H.L. Resnikoff and R.O. Wells, *Wavelet Analysis: The scalable structure of information*, Springer-Verlag, New York, (1999).
- [33] G.I.N. Rozvany, M. Zhou and T. Birker, *Generalized shape optimization without homogenization*, Structural Optimization, 4, (1992), 250-252
- [34] G.I.N. Rozvany, M. Zhou, T. Birker and O. Sigmund, *Topology optimization using iterative continuum-type optimality criteria (COC) methods for discretized systems*, in Topology design of structures, edited by M.P. Bendsøe and C.A. Mota Soares, Kluwer Academic Publishers, (1993), 273-286
- [35] P. Seshu, *Substructuring and component mode synthesis*, Shock and Vibration, 4 (3), (1997), 199-210.
- [36] K. Suzuki and N. Kikuchi, *A homogenization method for shape and topology optimization*, Computer Methods in Applied Mechanics and Engineering, 93 (1991) 291-318
- [37] R.O. Wells and X. Zhou, *Wavelet solutions for the Dirichlet problem*, Numerische Mathematik, 70, (1995), 379-396

- [38] E.L. Wilson, *The static condensation algorithm*, International Journal of Numerical Methods in Engineering, 8 (1974), 199-203
- [39] E.L. Wilson, M-W. Yuan and J.M. Dickens, *Dynamic analysis by direct superposition of Ritz vectors*, Earthquake Engineering and Structural Dynamics, 10, (1982), 813-821
- [40] R-J. Yang, *Metamodeling development for vehicle frontal impact simulation*, (DETC2001/DAC-21012), Proceedings of the 27th Annual ASME Design Automation Conference. Pittsburgh, PA, Sept 9-12, (2001).

MICHIGAN STATE UNIVERSITY LIBRARIES



3 1293 02563 6055